5G Waveform Candidate Selection

D3.1

‘5GNOW_D3.1_v1.0.docx’

Version: 1.0

Last Update: 3/3/2015

Distribution Level: CO

- ***Distribution level***
  PU = Public,
  RE = Restricted to a group of the specified Consortium,
  PP = Restricted to other program participants (including Commission Services),
  CO= Confidential, only for members of the 5GNOW Consortium (including the Commission Services)

SEVENTH FRAMEWORK PROGRAMME
Alcatel·Lucent
cea leti
Fraunhofer Heinrich Hertz Institute
is-wireless
NATIONAL INSTRUMENTS
TECHNISCHE UNIVERSITÄT DRESDEN

The 5GNOW Project Consortium groups the following organizations:

Partner Name	Short name	Country
FRAUNHOFER-GESELLSCHAFT ZUR FOERDERUNG DER ANGEWANDTEN FORSCHUNG E.V.	HHI	Germany
ALCATEL-LUCENT DEUTSCHLAND AG	ALUD	Germany
COMMISSARIAT À L'ENERGIE ATOMIQUE ET AUX ENERGIES ALTERNATIVES	CEA	France
IS-WIRELESS	ISW	Poland
NATIONAL INSTRUMENTS	NI	Hungary
TECHNISCHE UNIVERSITÄT DRESDEN	TUD	Germany

Abstract:
One of the main drivers for new waveforms is to enable efficient multiple access in the light of the requirements of future 5G wireless communication systems which will have to handle a very diverse variety of traffic types. The scenarios which are initiating those requirements and which are considered by the 5GNOW project (see D2.1) are driven by machine-type communication and the Tactile Internet, by coordinated multi-point (CoMP) and by fragmented spectrum. The 5GNOW project has developed here the vision of a unified frame structure and corresponding new waveforms which aims at handling as much different traffic types as possible within the same band and the same frame.
This document introduces promising waveform candidates for 5G systems, explains the considered reference scenarios and the corresponding multiple access vision. Supporting simulation results are provided, stressing the potential of the candidate technologies. Selection criteria for the waveforms are provided and discussed. In conclusion, the introduced waveforms are much more capable than OFDM when relaxed synchronicity and orthogonality requirements shall be supported. Particularly, they allow dropping a large amount of signalling overhead present in today's systems, when e.g. a large number of devices have to be supported.
Future work of the 5GNOW project will investigate those waveform candidates in detail and propose a physical layer concept for next generation wireless communication systems
Based on the waveform candidates in IR3.1, D3.1 contains selection criteria, benchmarking results and discussion of chosen candidate selection for 5G waveforms.

Partner	Author name
HHI	Martin Kasparick Gerhard Wunder Peter Jung
ALUD	Yejian Chen Frank Schaich Thorsten Wild
CEA	Vincent Berg Nicolas Cassiau Jean-Baptiste Doré Dimitri Kténas
ISW	Marcin Dryjański Slawomir Pietrzyk
TUD	Ivan Simões Gaspar Nicola Michailow

"The research leading to these results has received funding from the European Community's Seventh Framework Programme (FP7/2007-2013) under grant agreement n° 318555"

Document Identity

Title:	5G Waveform Candidate Selection
WP:	WP3 – Physical layer design
WP Leader	ALUD
Main Editor	Thorsten Wild
Number:	D3.1
File name:	5GNOW_D3.1_v1.0.docx
Last Update:	Tuesday, March 03, 20153

Revision History

No.	Version	Edition	Author(s)	Date
1	0.1		Thorsten Wild (ALUD)	28.06.13
	Comments:	Provided initial template and skeleton		
2	0.2		Input by all authors; Thorsten Wild	09.08.13
	Comments:	Merged partner inputs, added summary, conclusion and some guiding text		
3	0.3		Thorsten Wild	14.08.13
	Comments:	Review comments by CEA, TUD and ISW taken into account and merged into one document		
4	0.4			16.09.12
	Comments:	Reference added		
5	0.5		Martin Kasparick	20.09.13
	Comments:	Polishing		
6	v1.0		Gerhard Wunder (Coordinator)	23.09.2013
	Comments:	Final revision		
7				
	Comments:			
8				
	Comments:			
9				
	Comments:			
10				
	Comments:			
11				
	Comments:			
12				
	Comments:			
13				
	Comments:			
14				
	Comments:			
15				
	Comments:			

Table of Contents

Executive Summary

This document presents the selected 5GNOW waveform candidates for next generation wireless systems.
Chapter 1 gives an overview on the scope of the 5GNOW project and the considered reference scenarios for 5G communication systems. With respect to the chosen scenarios, respective motivations for the new waveform candidates are provided. Waveform candidates support coordinated multi-point transmission and reception (CoMP) better than OFDM in the presence of timing and frequency offsets. The Tactile Internet is addressed by providing waveform candidates, supporting very short bursts for a very low latency air interface. Sporadic access, driven by machine-type communication and the Internet of Things, is better supported in conjunction with classical high-data-rate traffic by presenting the unified frame structure vision and the waveform candidates supporting this. The candidates contain improved spectral properties, compared to OFDM, which make very efficient use of fragmented spectrum bands.

Chapter 2 presents selected waveform candidates for 5G communications systems: Filter-bank based multi-carrier (FBMC), Generalized Frequency Division Multiplexing (GFDM), Universal Filtered Multi-Carrier (UFMC) and Biorthogonal Frequency Division Multiplexing (BFDM). The waveform techniques are described there in detail.

Chapter 3 presents the 5GNOW vision for multiple access. The unified frame structure is an efficient, flexible and scalable solution for supporting heterogeneous traffic types within the same band. The usage of different signal layers in conjunction with iterative receiver technologies offers additional degrees of freedom. For random access, a modern sparsity-aware approach is presented. Simulation results for those multiple access scenarios are provided which show in an exemplary manner advantages of the proposed solution supported by waveform candidates. Further details related to chapter 3 are discussed in appendix B.

Chapter 4 picks up the 5GNOW reference scenarios in more detail. Here, simulation results for the candidate waveforms are presented, stressing their potential in the anticipated future communication scenarios. Further details related to chapter 4 are contained in appendix C.

Chapter 5 provides a first basic comparison and discussion of the waveform candidates.

Chapter 6 concludes D3.1.

In Appendix A, principles of waveform design and pulse shaping are presented, which gives the theoretical background for this document.

1 Introduction

This chapter explains the scope of 5GNOW and 5G wireless communication systems. It introduces the 5GNOW multiple access vision and shows alternatives to orthogonal frequency division multiplexing (OFDM) for the 5G application scenarios. Section 1.4 presents the structure of this entire document.

1.1 Overview on 5GNOW and related 5G activities

While fundamental research for 5G is now well under way [Met13, WKB+13] the question what actually makes a 5G system, what are the drivers is still open and part of intensive discussions. The 5GNOW project has published a first white paper version in [WKB+13] and short follow up [WKW+13] with initial waveform results. It is outlined that 5G should be driven by applications and reference scenarios not possible today or even unimaginable with current technology.

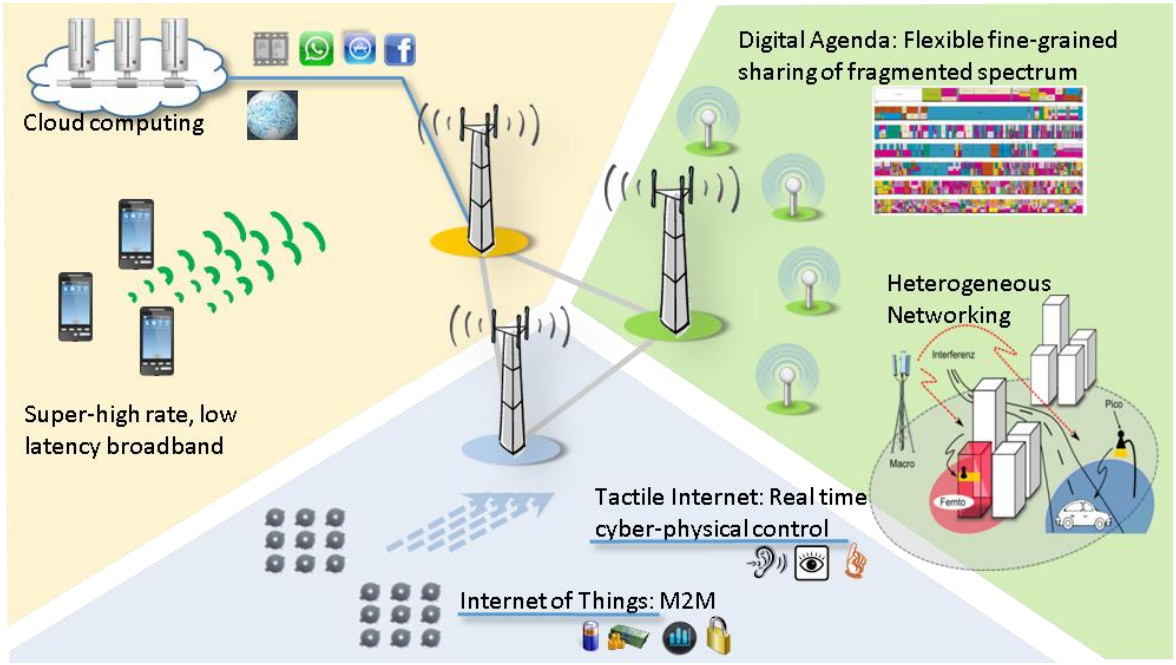

Figure 1.1.1: ***Application Challenges***

The main drivers for 5GNOW are:

1) Tactile Internet: This application scenario enables real-time cyber-physical tactile control experiments. The toughest real time constraint is the human tactile sense which distinguishes latencies in the order of 1ms. As derived e.g. in [Fet12], in this setting 1ms round trip time requires a time budget on PHY of max. 100 µs.
2) Internet of Things (IoT): The IoT is possibly the next killer application but business models have not started off yet. There is as scalability problem (>100k MTC nodes in a cell) under the premises of cost, coverage, energy (life time) and privacy.
3) Gigabit Wireless Connectivity: There are many application examples of future Gigabit wireless, for example users will want to have quick downloads (e.g. from a wireless data

kiosk) of e.g. 3D streaming content with data rates in the order of ~100 Mbit/s. Thereby download times are expected to be 100 times faster thus in the order of ~ 10 Gbit/s.

4) Fragmented Spectrum and the Spectrum Paradox: Spectrum is scarce and expensive but underutilized. Hence, e.g. with White Spaces Communication according to the table of KPIs in [D2.1] a 100x better localization and related PAPR issues is expected.

Altogether the wireless access has to be **flexible, scalable, content aware, robust, reliable and efficient in terms of both energy and spectrum**. There are strong indicators that at least for some of the mentioned applications the OFDM waveform is not suitable. In this document/deliverable new waveform approaches that overcome the disadvantages of OFDM are discussed. The main challenges are depicted in Figure 1.1.1.

1.2 5GNOW unified frame vision

5GNOW is the physical layer evolution of mobile communication network technology such as LTE-Advanced towards the emerging application challenges. While LTE is tailored to maximize performance by enforcing strict synchronism and orthogonality, the emerging trends reveal major pitfalls:

1) Machine-type communication (MTC) communications requires bulky procedures to ensure strict synchronism.
2) Collaborative schemes use tremendous efforts to collect gains under the premise of strict synchronism and orthogonality.
3) Digital Agenda/Carrier aggregation forces systems to deal with fragmented spectrum.

5GNOW is an explorative research proposal challenging the obedience of LTE and LTE-Advanced to strict synchronism and orthogonality with respect to the future applications. It introduces non-orthogonal waveforms that carry the data on physical layer enabling

1) Asynchronous MTC traffic with drastically reduced signalling and increased life time
2) Provision of asynchronous coordinated multi-point (CoMP) / Heterogeneous Networking (HetNet) concepts beyond the ‘coordinate everything approach’
3) Implementation of asynchronous carrier aggregation concepts with well frequency localization

The 5GNOW approach is able to efficiently support different traffic types, which all have to be part of future wireless cellular systems. Our vision of a unified frame structure concept, depicted by Figure 3.1.1, aims at handling the large set of requirements within a single 5G system. A (filtered) multicarrier approach will enable the mix of synchronous / asynchronous and orthogonal / non-orthogonal traffic types, where the reduced side-lobe levels of the waveform seek to minimize inter-carrier interference (ICI).

The classical “bit pipe” traffic (Type I) with high volume data transmission and high-end spectral efficiency still exploits orthogonality and synchronicity, wherever it is possible, e.g. when serving cell-center users. Vertical layering at common time-frequency resources generates a non-orthogonal signal format supporting heterogeneous cell structures and cell edge transmissions more efficiently. For high-volume data applications in those cell areas (Type II), a multi-cell, multi-user transceiver concept is required. The principle of interleave division multiple access (IDMA) [PLL03] is a very

appealing approach for generating these signal layers and an elegant receiver and coding concept for it.

MTC is expected to be one dominant application of 5G systems. For this sporadic traffic type (Type III), a contention based-access technique is attractive, saving overhead by dropping the strict synchronicity requirement. For sensor-type traffic (Type IV), the open weightless standard [Wei] has shown that, from an energy-efficiency perspective, it is beneficial to stretch the transmissions in time by spreading. This additional signal layer, again, can be handled by an IDMA-like approach.

5GNOW on top of that, will provide the MAC scheduling framework to accompany the waveform with necessary algorithms and signaling to assure, that various types of traffic could be managed efficiently, taking into account trade-off between signaling and accuracy. As MTC traffic and “bit pipe” traffic are different service types (e.g. MTC is typically UL low bitrate, and “bit pipe” is a typically DL high bitrate), 5GNOW will address these issues to incorporate them into the MAC design.

1.3 OFDM – the choice of 4G: limitations and alternatives

The limitations of OFDM and potential new waveforms will be discussed along the following 5GNOW reference scenarios (described in detail in [D2.1]) along with the requirements and current limitations.

1.3.1 Uplink CoMP

One important Type II reference scenario for 5GNOW is the multiuser uplink CoMP joint reception case where we face timing and carrier frequency offsets (CFOs). Uplink timing advance control mechanisms in LTE can align receive signals of a single cell, but, due to propagation delay differences, Uplink CoMP joint reception across multiple cells has inherent timing offsets degrading the potential performance gains of current LTE-A. Moreover, relaxed oscillator requirements (like those in WLAN instead of LTE) are beneficial in terms of cost and performance for mass market devices. Both will push multi-carrier waveforms with lower side lobe levels. This scenario is tackled with a novel block-wise filtering multi-carrier approach, which we denote as universal filtered multi-carrier (UFMC).

1.3.2 Tactile Internet

A 'Tactile Internet' Type IV reference scenario was proposed in [Fet12] as a new service and technology enabling ingredient in the next 5G wave. This application imposes strict latency and resilience requirements for short and asynchronous bursts of data. For an MTC uplink in a cellular network, the overall goal for a tactile experience is to achieve a round trip delay of 1 ms. For the air interface, a feasible proposal is to transmit data bursts of up to 1000 bits within 100 µs. Both is infeasible with current LTE technology. In 5GNOW, a PHY layer based on generalized frequency division multiplexing (GFDM) [FKB09, MGK+12] will be explored to address these specific requirements.

1.3.3 Downlink CoMP

The opportunity to support Type II traffic with filter bank multicarrier (FBMC) for downlink CoMP is studied:

1) Received signals from multiple cells may not be aligned in time at the receiver due to propagation delay differences and due to possible time de-synchronization between cooperating BSs. This offset causes pilots rotations at the receiver that make the estimation of the channel difficult in LTE-A.
2) In order to deal with different time of arrivals from different BSs degrading the potential performance gains of current LTE-A. In LTE-A, the receiver may estimate the delay and feedback the information to the BSs. The cost of this operation, in term of UL bandwidth, will be studied.
3) Furthermore multiuser CoMP implies CSI knowledge at the transmitter side. Therefore the necessary information to be fed back to the BSs will be investigated as well reducing the level of control information solutions (backhaul and CSI feedbacks) momentarily infeasible degrading the performance of LTE-A.

1.3.4 Sporadic Access

Similar to the implementation in UMTS the goal is to transmit small user data packets using the physical layer random access channel (PRACH) thereby not maintaining a continuous connection (Type IV). So far, this is not possible in LTE, where data is only carried using the physical uplink shared channel (PUSCH) and the required control signalling effort rendering scalable MTC (several hundred nodes in the cell accessing the BSs) infeasible. The goal of the Sporadic Access reference scenario is joint link acquisition and the transmission of “sparse data” in the total number of dimensions within 1 to X subframes.

1.3.5 Fragment Spectrum

Both LTE and FBMC may theoretically be suited to multicarrier-based spectrum pooling. However, high adjacent channels’ rejection cannot be met without a very complex and programmable band-pass transmit filter in the LTE case, whereas FBMC would simply requires “switching on and off” the appropriate carriers at the transmitter. The main shortcoming of the LTE waveform identified here originates from the large side-lobes because of the rectangular shaping of the temporal signal whereas the FBMC built-in filtering feature (100x better localization) adapts to spectrum availability even in the fragmented case.

2 Overview of the Considered Waveform Approaches

To enable the 5GNOW approach the basic concept of this proposal is to dismiss the widely unquestioned assumption of strict synchronism and orthogonality in the network and, instead, to introduce a broader non-orthogonal robustness concept incorporating the overall required control signaling effort and the applied waveforms in a joint framework. At the core of this paradigm is the introduction of new non-orthogonal waveforms that carry the data on the physical layer. The idea is to abandon synchronism and orthogonality altogether, thereby admitting some crosstalk or interference, and to control these impairments by a suitable transceiver structure and transmission technique. Current research addresses these design goals by various filter bank based signal design techniques. A comprehensive description of the proposed schemes is given in this chapter, namely Generalized Frequency Division Multiplexing (GFDM), Universal Filtered Multicarrier (UFMC), Filter Band Multicarrier (FBMC) and Biorthogonal Frequency Division Multiplexing (BFDM).

Note that the main drivers for the choice of those candidate waveforms are the multiple access for 5G, discussed in chapter 3, and the different reference scenarios, discussed in chapter 4. Related performance results are discussed in those respective chapters.

2.1 GFDM

Generalized frequency division multiplexing (GFDM) is a non-orthogonal, digital multicarrier transmission scheme proposed to address emerging requirements in cellular communications system such as opportunistic use of spectrum and machine-to-machine communication with special attention to asynchronous low duty cycle transmission and exploration of non-continuous bandwidths. It is a flexibility modulation scheme capable to spread data across a two-dimensional (time and frequency) block structure (multi-symbols per multi-carriers). In contrast to the traditional orthogonal frequency division multiplexing (OFDM), it can benefit from transmitting multiple symbols per sub-carrier. GFDM targets block based transmission which is enabled by circular pulse shaping of the individual sub-carriers.

Regarding out of band radiation the transmit signal exhibits strong frequency localization per subcarrier by applying adjustable pulse shaping filters. Circular convolution is employed in the process to preserve the block oriented structure (preventing non negligible rate loss that would otherwise occur from filter tails in burst transmission scenarios) and allows introduction of cyclic prefix (CP) to provide a simple way of equalization when data is transmitted through a multipath channel. Additionally, time windowing schemes can be applied over the extended GFDM block, allowing further control of out of band radiation at a small expense of the CP length.

By introducing variable pulse shaping filters, the orthogonality between the subcarriers is initially dismissed. As a result, self-induced inter-carrier and inter-symbol interferences need to be accounted for. While GFDM has self-interference due to signal design, impairments due imperfect synchronism affect the performance of multiple access scenarios in LTE systems in a similar way. So, by overcoming this problem, GFDM aims to relax the current requisites of oscillator accuracy of 0.1 ppm in LTE up to 10-100 times (1-10 ppm) and allows the design of simpler transmitters, leaving out complex synchronization procedures and reducing signaling overhead.

Nevertheless, GFDM can also explore offset QAM modulation, similar to the filter bank based multi-carrier (FBMC) approach (section 2.3), with additional elimination of filter tails in the signal with its circular pulse shaping approach. So, in favorable applications, GFDM can be shaped to address orthogonal conditions as well. Although FBMC may be shaped to use a higher number of symbols with shorter length to minimize tail penalties in short burst transmission scenario, multipath channel effects spreading over several successive symbols can substantially increase complexity in time domain equalization process. The circular structure of GFDM allows equalization to be performed in frequency domain, multipath echoes that spread over several symbols can be easily combated within the proposed approach, making it favorable to short burst applications.

These characteristics of GFDM combined with the idea of shifting as much processing as possible to the base station in the uplink scenario can contribute to reduce the power consumption of the terminals. An equivalent approach with OFDM is disadvantageous due the high spectral leakage of the sinc-pulse and strict requirements to synchronization in order to maintain subcarrier orthogonality or equivalently a relatively large amount of redundant CP for relaxing the lack of synchronism.

As a generalization of OFDM, GFDM is compliant with it when the number of symbols per subcarrier is chosen to be one. It can reach OFDM BER performance while facilitating pulse shaped subcarriers for suppression of out of band radiation and thus minimizing interference to the legacy system when opportunistically used in white spaces.

2.1.1 Mathematical description of the GFDM transceiver

Let $d[k,m]$ be a complex valued information symbol. The $K \times M$ matrix

$$\mathbf{D} = \begin{pmatrix} d[0,0] & \dots & d[0,M-1] \\ \vdots & \ddots & \vdots \\ d[K-1,0] & \dots & d[K-1,M-1] \end{pmatrix} \tag{2.1.1}$$

will be addressed as one information block. Therein, $k = 0,\dots,K-1$ shall denote a subcarrier while $m = 0,\dots,M-1$ refers to a time slot. With the intention to distribute the data symbols in time and frequency, the discrete impulse response of the pulse shaping transmit filter $g[n]$ needs to be movable in those dimensions. Mathematically, the expression $g[n-mN]e^{j2\pi\frac{kn}{N}}$ accounts for these shifts, where given a sampling time T_S the length of one symbol in time is $T_d = NT_S$ and $\frac{1}{NT_S}$ denotes the spacing of two neighboring subcarriers in frequency domain. The transmit signal

$$x[n] = \sum_{m=0}^{M-1}\sum_{k=0}^{K-1} d[k,m]g[n-mN]e^{j2\pi\frac{kn}{N}}, \quad 0 \le n \le NM \tag{2.1.2}$$

results for one block from the superposition of all shifted impulse responses that are weighted with the respective information symbols $d[k,m]$.

In order to be able to perform equalization at the receiver in frequency domain, $x[n]$ is prefixed with a cyclic extension and yields $\tilde{x}[n]$, which is the signal that is going to be sent through the radio channel.

The received signal is given by

$$\tilde{y}[n] = \tilde{x}[n] * h[n] + n[n] \tag{2.1.3}$$

where $*$ denotes convolution with respect to n . Removing the CP, provides $y[n]$ and assuming the channel response $h[n]$, is known perfectly at the receiver, one block of $K \times M$ information symbols is equalized by

$$\overline{y}[n] = \mathrm{IDFT}\left(\frac{\mathrm{DFT}(y[n])}{\mathrm{DFT}(h[n])}\right) \tag{2.1.4}$$

with $\mathrm{DFT}(\bullet)$ being the discrete Fourier transform and $\mathrm{IDFT}(\bullet)$ denoting its inverse. However, in order to ensure the cyclic structure of $y[n]$ that is a prerequisite to $\overline{y}[n]$, the CP of the system requires to account for the channel, as well as the transmit and receive filter.

Assuming T_h denotes the length of the channel impulse response in time domain and T_g the length of the matched filter, and then the cyclic prefix needs to be of length $T_{CP} = T_g + T_h + T_g$ to prevent interference between subsequent blocks and to make frequency domain equalization (FDE) possible. The resulting decrease of the data rate is of factor

$$\frac{T_b}{T_b + T_{cp}} \tag{2.1.5}$$

and the increase of the power required to transmit one bit of information is its reciprocal for $T_b = M T_d$. Clearly, from this point of view it is desirable to keep T_{CP} as short as possible, while at the same time for spectral shaping large values for T_g are favorable. Tail biting [FKB09] has been introduced as one way to reduce the length of the CP without cutting short on the pulse shaping filter length. It is based on the idea of preserving a circular structure within each transmitted block, which allows to keep the length of the CP independent from the length of the transmit filter.

While in [FKB09], tail biting is only used on the transmitter side, this report applies the concept also to the receiver. Therefor each subcarrier is received and processed using the matched filter $g[n]$ according to

$$\overline{y}_k[n] = \overline{y}[n] e^{-j2\pi\frac{kn}{N}} \# \; g[n] \tag{2.1.6}$$

with a circular convolution $\#$ with respect to n . By keeping every N th sample, the information symbols $\overline{d}[k,m] = \overline{y}_k[mN]$ are retrieved and passed to the detector. The complete GFDM system model is depicted in Figure 2.1.1 below. A low complex implementation is described in [MGK+12] and [GMN+13].

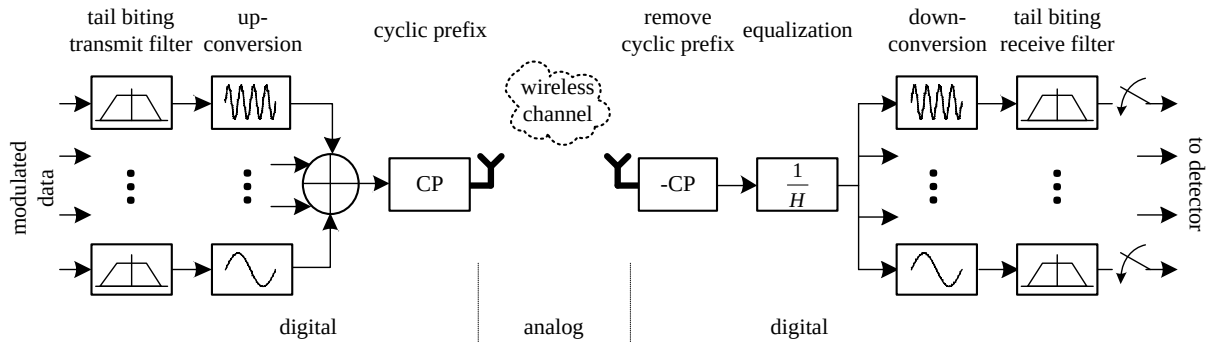

Figure 2.1.1: GFDM transceiver model

2.2 UFMC

Filterbank based multi-carrier (FBMC) and filtered OFDM [Far11] have a long history in telecommunication research. The former applies a filtering functionality on a per subcarrier basis; the latter filters the complete multicarrier band in a single shot. Both variants have various implications for transmitting data via a wireless link. Neither of the two schemes outperforms the other in every aspect relevant for communication. While FBMC provides a better subcarrier separation, filtered OFDM is less complex.

A closer look reveals the two schemes to be the extreme cases of a more general waveform design: As outlined above, FBMC applies a filtering on a per subcarrier basis. By doing so, many advantages can be harvested on. Just to name one, inter-carrier interference is highly reduced in case of frequency jitter / offsets either due to Doppler or due to misaligned oscillators. However, the cost to pay are comparatively long filter lengths according to one of the natural laws of signal processing – Küpfmüller's uncertainty [KK00] principle (the product of the length and the bandwidth of a given pulse is constant). Filtered OFDM is on the other side of the space of options. Filtering is done over the complete band. So, the filter bandwidth is much higher and thus the filter length is much smaller than with FBMC.

Having identified this, we have designed a more universal solution: Universal Filtered Multicarrier (UFMC). UFMC applies filtering to subsets of the complete band instead of single subcarriers or the complete band.

Figure 2.2.1 depicts an exemplary baseband structure of the UFMC transmitter with B sub-bands (single antenna case). The i-th UFMC sub-module, with $i \in \{1,2, ..., B\}$, generates the $(N+N_{\text{filter}}-1)$-dimensional time-domain baseband vector $\mathbf{x}_i$ following the UFMC design criteria for the respective sub-band carrying the complex QAM symbol vector $\mathbf{s}_i$ with dimension n_i x1. N is the required number of samples per symbol to represent all sub-bands without introducing aliasing (i.e. N depends on the overall covered bandwidth), the sample rates of the single sub-bands naturally have to be aligned to each other, N_{filter} the length of the filter.

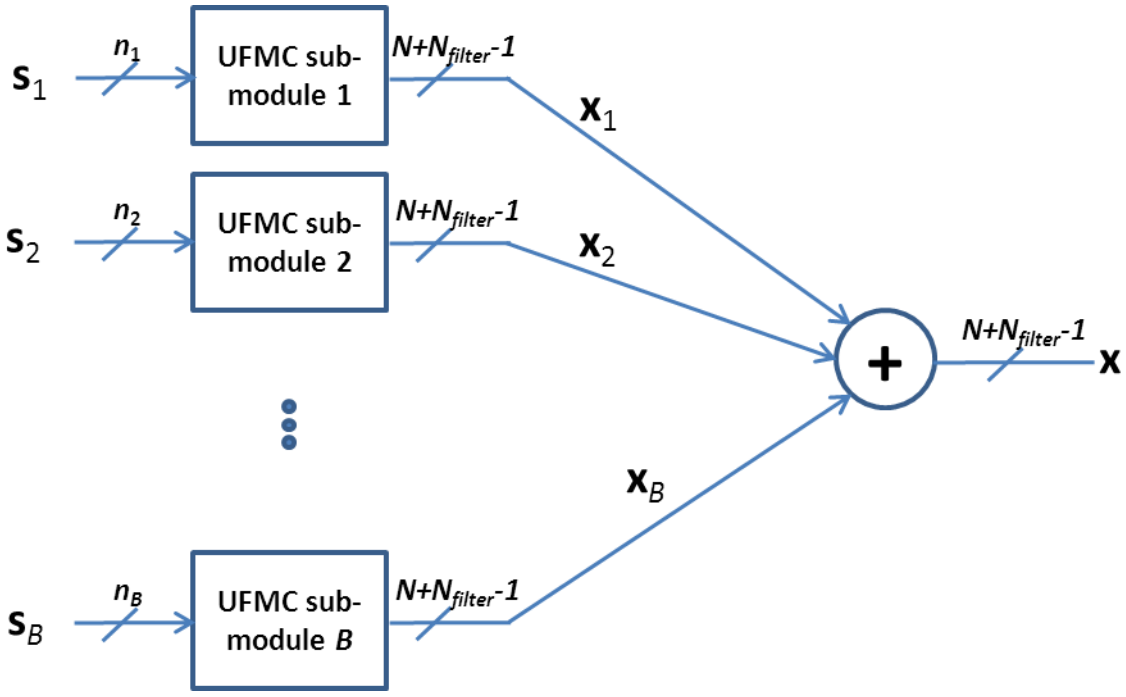

Figure 2.2.1: General UFMC transmitter structure

We consider one multi-carrier symbol out of a consecutive stream of symbol vectors, dropping the temporal symbol index for the ease of notation. The single sub-band signals are combined to synthesize the transmit vector **x**. In case of downlink (DL) the single sub-modules cover the complete available frequency band(s), transporting data to multiple users. (Note that in case of fragmented spectrum, UFMC also supports non-contiguous subbands.) In uplink (UL) the single sub-modules cover only the frequency portion the respective user has been allocated to. A single sub-module is constructed according to Figure 2.2.2.

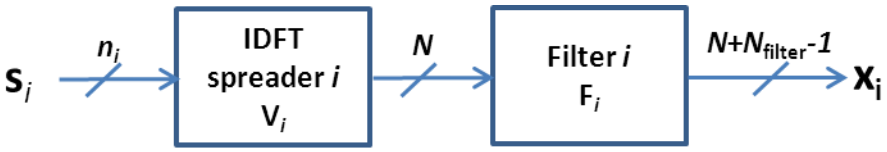

Figure 2.2.2: UFMC transmitter submodule

The n_i complex QAM symbols are transformed to time-domain using an IDFT spreader. Then the sub-band filter is applied. The time-domain transmit vector for a particular multi-carrier symbol is the superposition of the sub-band-wise filtered components:

$$\mathbf{x} = \sum_{i=1}^{B} \mathbf{F}_i \mathbf{V}_i \mathbf{s}_i \qquad (2.2.1)$$

$\mathbf{V}_i$, being of dimension N x n_i, includes the relevant columns of the inverse Fourier matrix according to the respective sub-band position within the overall available frequency range, $\mathbf{F}_i$ is a Toeplitz matrix with dimension $(N+N_{filter}-1)xN$, composed of the filter impulse response, enabling the convolution.
The signal can be rewritten without the summation by the following definitions:

$$\overline{\mathbf{F}} = [\mathbf{F}_1, \mathbf{F}_2, \ldots, \mathbf{F}_B]$$
$$\overline{\mathbf{V}} = diag\ (\mathbf{V}_1, \mathbf{V}_2, \ldots, \mathbf{V}_B)$$
$$\overline{\mathbf{s}} = [\mathbf{s}_1^T, \mathbf{s}_2^T, \ldots, \mathbf{s}_B^T]^T$$

This enables columnwise stacking of filter matrices, generating a block-diagonal IDFT matrix and stacking of all data symbols into one column, respectively. This results into:

$$\mathbf{x} = \overline{\mathbf{F}}\,\overline{\mathbf{V}}\,\overline{\mathbf{s}} \qquad (2.2.2)$$

The following table summarizes the available design elements:

Table 2.2.1: Design elements for UFMC

B	Number of sub-bands
n_i	Number of subcarriers in sub-band *i*
N	Overall number of subcarriers
Filter *i*	length/bandwidth, filter characteristic defined by FIR filter coefficients

The choice of *B* depends on the spectral settings the UFMC transmitter has to deal with (e.g. fragmented spectrum) and on the system design targets. If the system is to be applied to a scenario with fragmented spectrum, *B* may be chosen according to the number of available spectral sub-bands (*B* may even vary in time in case of some of the spectral sub-bands being populated by other wireless services only occasionally). Alternatively, for streamlining the overall system and controlling the spectral characteristics more fine-grained, the single sub-bands may even be subdivided into smaller chunks with equal size in every sub-band. We call the single spectral chunks physical resource blocks (PRB), following the terminology of LTE.

For the choice of the filter characteristics many alternatives are available. In the framework of 5GNOW we have started by applying FIR-coefficients defined by (Dolph-)Chebyshev windows, which are parametrizable in their shape in terms of side lobe attenuation. (Note that for a given main lobe width, a (Dolph-)Chebyshev window maximizes the side lobe attenuation.). Figure 2.2.3 depicts their characteristics in time and frequency domain for some exemplary settings (filter length: 80, side lobe attenuation: 60 dB).

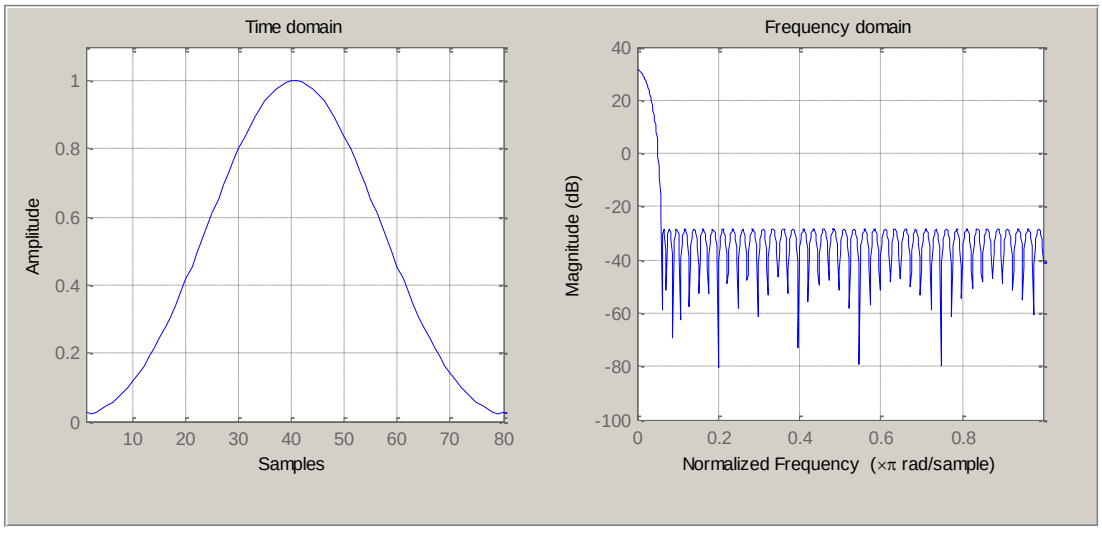

Figure 2.2.3: Chebyshev filter characteristic in time and frequency domain (filter length: 80, sidelobe attenuation: 60 dB)

The single sub-band/PRB filters are frequency-shifted according to the frequency position given by the preceding IDFT spreader onto the respective sub-band center frequency. Figure 2.2.4 depicts the spectral behaviour within a single sub-band with B=6 PRBs (each PRB spans n_i=12 subcarriers) when applying UFMC with filter length 16, FFT size 128 and side lobe attenuation of 120dB (a). (b) compares the spectral behaviour of UFMC with OFDM for a single PRB. The tremendous discrepancy in terms of out-of-band-radiation is apparent.

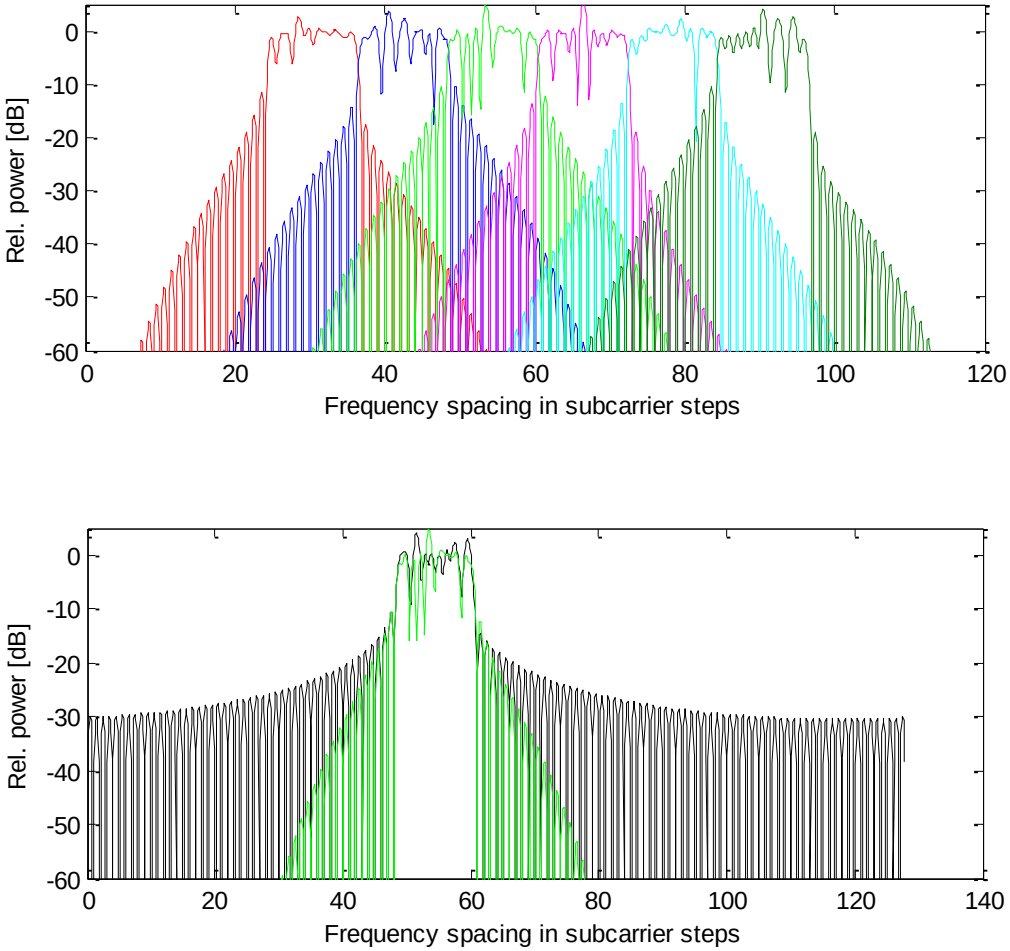

Figure 2.2.4: Spectral behaviour within a single sub-band (top) and for a single PRB compared to OFDM (bottom)

For reception, processing is done accordingly (for simplicity we concentrate on the elements purely related to UFMC signal processing, blocks dealing with channel estimation/equalization, error correction etcetera are in principle applicable to UFMC in a similar way as they are applicable to OFDM and FBMC), as depicted in Figure 2.2.5.

y is the received signal vector after propagation through the channel, represented by the convolution matrix **H** with Toeplitz structure, constructed by the time-domain channel impulse response, including the addition of noise **n**:

$$\mathbf{y} = \mathbf{H}\mathbf{x} + \mathbf{n} = \mathbf{H}\overline{\overline{\mathbf{F}}}\,\overline{\overline{\mathbf{V}}}\,\overline{\mathbf{s}} + \mathbf{n} \qquad (2.2.3)$$

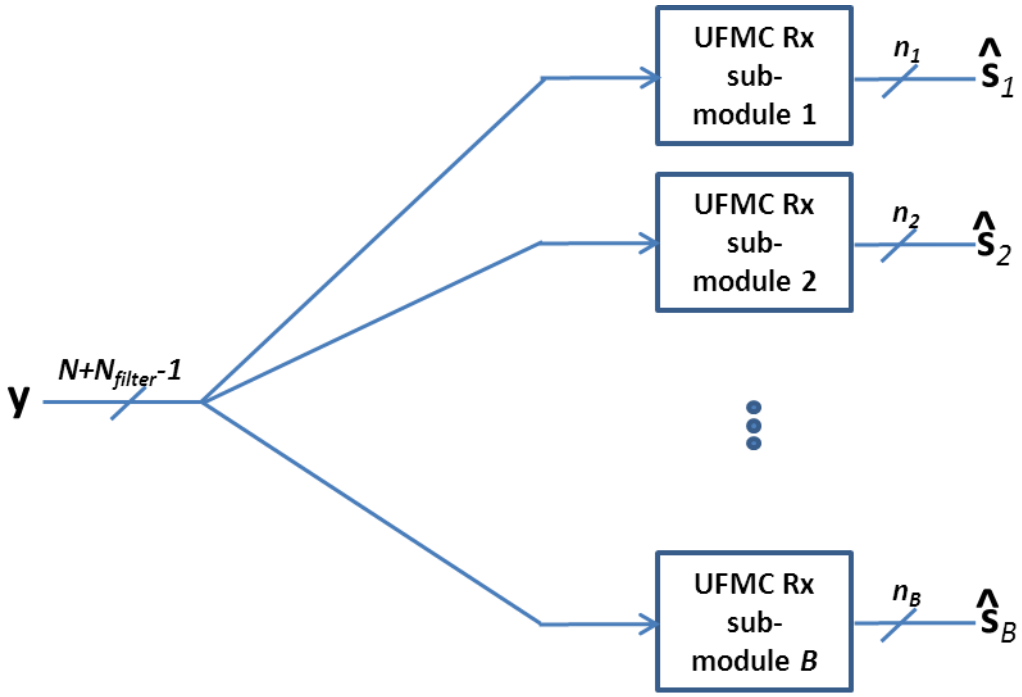

Figure 2.2.5: General UFMC receiver structure.

Each UFMC Rx sub-module outputs the transmitted symbol vectors including distortions (due to noise, channel and interference) of the respective sub-band. In UL the sub-modules are covering the complete frequency range used for data transmission, in DL the receiver is part of the user equipment, and so, the single sub-modules are only active, if the respective sub-band/PRB carries data and/or control messages relevant for the respective user.

Various design strategies for the receiver are possible. In the exemplary case of a linear receiver in an AWGN channel, represented by the identity matrix, the matched filter (MF) and zero forcing filter (ZF) can be written as

$$\mathbf{W}_{MF} = \left(\overline{\mathbf{F}}\,\overline{\mathbf{V}}\right)^{H} = \overline{\mathbf{V}}^{H}\overline{\mathbf{F}}^{H}, \qquad \mathbf{W}_{ZF} = \left(\overline{\mathbf{F}}\,\overline{\mathbf{V}}\right)^{+} = \overline{\mathbf{V}}^{+}\overline{\mathbf{F}}^{+} \tag{2.2.4}$$

with $\mathbf{A}^{+}$ being the Moore-Penrose-Inverse of a matrix. So the receiver operation in (2.2.4) can be viewed as a concatenation of inverse filtering and DFT despreading.

One design criterion for UFMC has been to keep the bulk of the advantages of FBMC and filtered OFDM, while avoiding the major disadvantages. Naturally, UFMC outperforms FBMC and filtered OFDM in some, but not all, of the different aspects relevant for communication. However, target of the studies in 5GNOW related to UFMC is to evaluate the scheme in the light of various relevant scenarios (Tactile Internet, inclusion of MTC traffic, fragmented spectrum, UL joint reception) of wireless cellular communications and to show UFMC to be a very promising solution for wireless cellular communication in an overall manner.

Initial results regarding the applicability of UFMC to the unified frame structure concept and in the light of UL joint reception [VWS+13] are given in the respective chapters 3 and 4.

2.3 FBMC

2.3.1 Overview of FBMC

A multicarrier system can be described by a synthesis-analysis filter bank, i.e. a trans-multiplexer structure. The synthesis filter bank is composed of all the parallel transmit filters and the analysis filter bank consists in all the matched receive filters, as shown in Figure 2.3.1 where $p_{Tx}(t)$ and $p_{Rx}(t)$ are respectively transmit and receive prototype filters. For subcarrier k, the filter is the prototype filter phase shifted by $e^{j2\pi f_k t}$. This phase shift in the time domain implies a frequency shift of f_k in the frequency domain. In this figure, the data signal is defined by Eq. (2.3.1):

$$s_k(t) = \sum_{n=-\infty}^{\infty} s_k[n]\,\delta(t - nT) \qquad (2.3.1)$$

with $s_k[n]$ the data symbols for subcarrier k, T the symbol period, n the symbol number and N_c the number of subchannels.

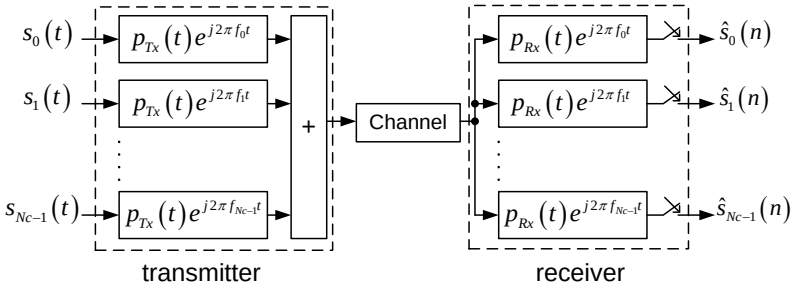

Figure 2.3.1. Block diagram of a multicarrier transceiver.

The most widely used multicarrier technique is OFDM, based on the use of inverse and forward DFT for the analysis and the synthesis filter banks. The prototype filter is a rectangular window whose size is equal to the Fourier Transform. At the receiver, perfect signal recovery is possible under ideal channel conditions thanks to the orthogonality of the subchannel filters. Nevertheless under real multipath channels a data rate loss is induced by the mandatory use of a cyclic prefix (CP), longer than the impulse response of the channel. With filter bank multicarrier (FBMC), the CP can be removed and subcarriers can be better localized, thanks to more advanced prototype filter design.
The FBMC prototype filter can be designed in many ways, trying to satisfy different constraints. In general, it is chosen to be:

- complex modulated for good spectral efficiency
- uniform to equally divide the available channel bandwidth
- with finite Impulse Response for ease of design and implementation
- orthogonal, to have a single prototype filter
- with Nearly Perfect Reconstruction (NPR) : certain amount of filter bank distortions can be tolerated as long as they are negligible compared to those caused by the transmission channel

In this document the prototype filter is designed using the frequency sampling technique. This technique provides the advantage of reducing the number of filter coefficients. In other words, the prototype filter coefficients should be given using a closed-form representation that includes only a few adjustable design parameters. The coefficients of the prototype filter for an overlapping factor *K* equal to 4 are [BEL10b]:

$$P_{0:3} = \left[1, 0.97195983, 1/\sqrt{2}, \sqrt{1 - P_1^2}\right] \qquad (2.3.2)$$

The KN_c-1 length time response of this filter is computed thanks to:

$$p_m = P_0 + 2\sum_{k=1}^{K-1} (-1)^k P_k \cos\left[\frac{2\pi k}{KN_c}(m+1)\right], m = 0 : KN_c - 2 \quad (2.3.3)$$

The stopband attenuation exceeds 60 dB for the frequency range above 10 channel spacings (Figure 2.3.2).

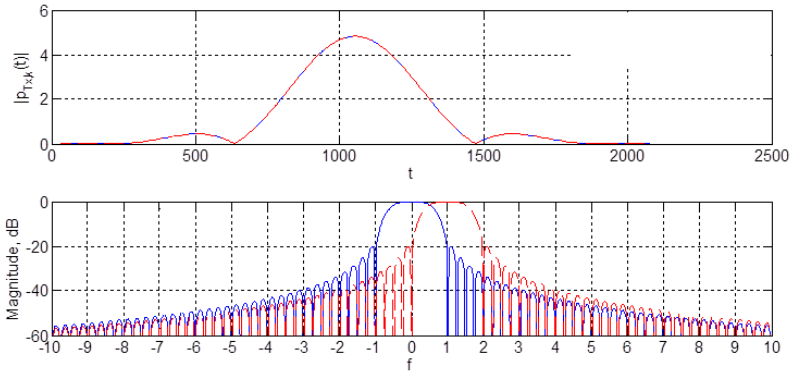

Figure 2.3.2. FBMC : filters for subcarriers 0 (blue) and 1 (red), $Nc = 512, K = 4$

As shown in Figure 2.3.2, adjacent carriers significantly overlap. In order to keep adjacent carriers and symbols orthogonal, real and pure imaginary values alternate on carriers and on symbols at the transmitter side. This so-called OQAM (Offset QAM) modulation implies a rate loss of a factor of 2. This efficiency loss of OQAM modulation is compensated by doubling the symbol period T.
K is frequently called the overlapping factor: indeed the symbol period is $T/2$ and the symbol length is $KT - 1$ samples; each FBMC symbol at the channel input is then overlapped with $2(2K - 1)$ other FBMC symbols.

2.3.2 Frequency domain description of FBMC

The transmitter of FBMC can be represented by Figure 2.3.3, with the filtering operation (block 'frequency spreading') done in the frequency domain. In this figure:

- $\mathbf{d}_m \in \mathbb{C}^{1\times N_c}$ is the vector containing the data to transmit for the m^{th} FBMC symbol.
- $\mathbf{X}_m = \mathbf{d}_m\widehat{\mathbf{G}}, \in \mathbb{C}^{1\times KN_c}$ is the vector of data for the m^{th} FBMC symbol filtered in the frequency domain.
- $\widehat{\mathbf{G}} \in \mathbb{R}^{N_c\times KN_c}$ is the matrix of filtering vectors given by Eq. (2.3.4), with $\mathbf{G} \in \mathbb{R}^{1\times 2K-1}$, the filtering vector, i.e. the frequency response of the filter given by Eq. (2.3.2):

$$\widehat{\mathbf{G}} = \begin{bmatrix} G & & 0 \\ & G & \\ 0 & & G \end{bmatrix} \quad (2.3.4)$$

- $\mathbf{x}_m \in \mathbb{C}^{1\times KN_c}$ is the vector of data for the m^{th} FBMC in the time domain.

The IFFT has a size of KN_c samples. The transmit signal is composed of the overlapping of symbols $\mathbf{x}_m$ with a factor of $N_c/2$.

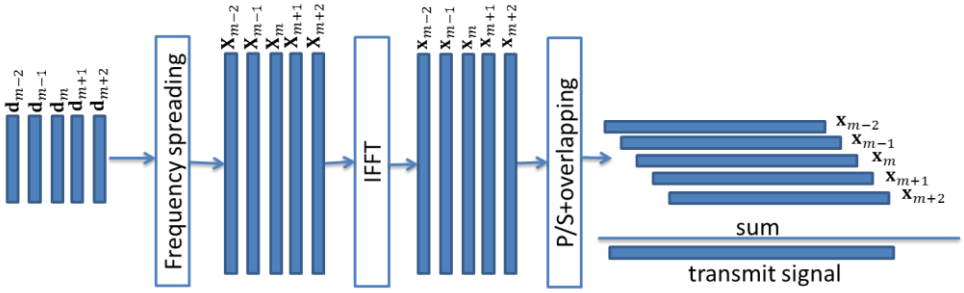

Figure 2.3.3. FBMC transmitter with filtering in the frequency domain

The frequency spreading operation is further described by Figure 2.3.4 where each carrier of $\mathbf{d}_m$ is spread on $2K-1$ carriers on $\mathbf{X}_m$. Here $K=4$. As can be seen from Figure 2.3.3, FBMC symbols overlap in the time domain and as Figure 2.3.4 shows, adjacent carriers in the vector $\mathbf{d}_m$ significantly overlap in the vector $\mathbf{X}_m$.

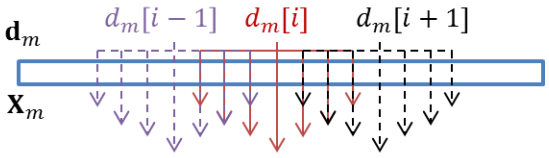

Figure 2.3.4. Frequency spreading

The FBMC receiver can be described by Figure 2.3.5, where the received signal is the transmitted signal after passing through the channel and after addition of white noise. The FFT has a length of KN_c samples and is done every $N_c/2$ samples, in order to recover the transmitted symbols (Figure 2.3.3). $\mathbf{Y}_m$ is then a vector of length KN_c samples.

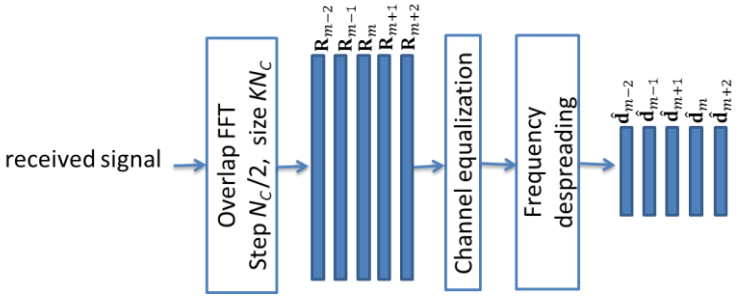

Figure 2.3.5. FBMC receiver with filtering in the frequency domain

In the frequency domain, the m^{th} received FBMC symbol, $m \geq 0$, $\mathbf{R}_m^i \in \mathbb{C}^{1\times KN_c}$, from BS i to UE is given by:

$$\mathbf{R}_m^i = \left(\mathbf{d}_m \widehat{\mathbf{G}}\right)\mathbf{H}_m^i + \mathbf{Z}_m = \mathbf{X}_m \mathbf{H}_m^i + \mathbf{Z}_m \qquad (2.3.5)$$

$\mathbf{Z}_m \in \mathbb{C}^{1\times KN_c}$ is the white noise (AWGN). $\mathbf{H}_m^i \in \mathbb{C}^{KN_c\times KN_c}$ is the matrix of the channel coefficients. As the channel impulse response is assumed to be short compared to the length of the FFT, $\mathbf{H}_m^i$ can be considered as diagonal.

2.3.3 Time synchronization

5GNOW identifies and questions orthogonality and synchronism as common design principles of the system architecture. FBMC modulation is good candidate waveform since time synchronization between users is not required. This particular property is discussed in the following sub-section.

In the case of OFDM, an important feature must be underlined. Due to synchronous transmission, the receiver may perform only one FFT for the considered channel, reducing notably the complexity. However, in case of non-synchronous transmission (see section 4.3), this property is lost for OFDM. Now let us consider the FBMC case.

When the frequency sampling technique is applied to the design of the prototype filter of a filter bank, the number of non-zero samples in the frequency response is given by P=2K-1. This suggests a direct approach to derive the transmitted signal, namely an inverse FFT combined with an overlap-and-sum scheme [BEL12]. If the system has N_c sub-channels, the size of the FFT is L = KN_c. At the receiver side a dual scheme may be implemented. This means that first a FFT is processed and in a second step the filtering is applied in the frequency domain.

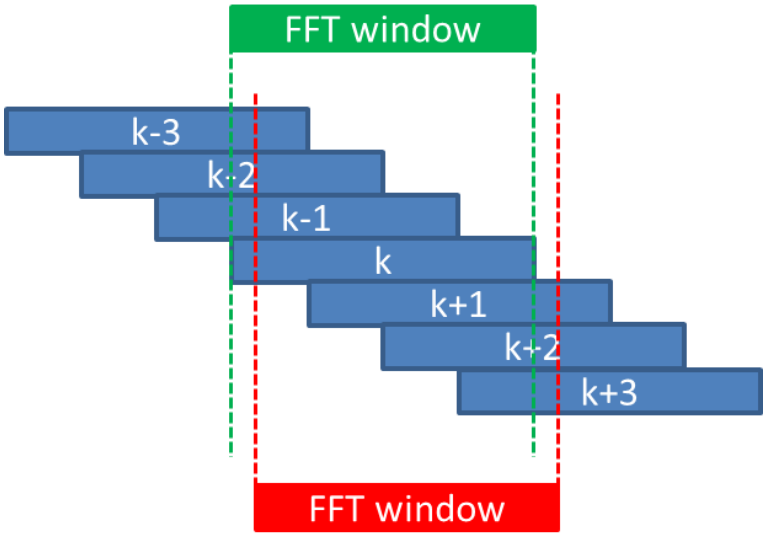

Figure 2.3.6. Case of perfect and imperfect synchronization at the receiver side for FBMC waveform

The case of a perfect synchronization is illustrated in Figure 2.3.6 (grey box). When a delay is introduced, the desired block *k* at the input of the FFT is shifted, a fraction of the block *k* is lost and a fraction of the adjacent block is introduced in the FFT window as illustrated in Figure 2.3.6 (red box). However, the interference generated is small due to the fair time localization properties of the prototype filter.

Indeed, the power of unwanted signal is small as illustrated in Figure 2.3.7. Assuming a filter length of 1024x4 (N_c=1024, K=4) taps prototype filter, the delay between two consecutive symbol is N_c/2=512 samples. This means that the maximum delay is 256 samples. It is clear from Figure 2.3.7 that the level of unwanted signal would in this worst case be very low.

The performance of FBMC in that respect is illustrated in Figure 2.3.8. A system with Nc=128 sub-channels and overlapping factor K=4 is considered. The timing offset is varied from 0 to Nc/2. The equalizer coefficients are assumed to be perfectly known at the receiver and the signal-to-noise ratio (SNR) is measured on the constellation at the output of the system. The SNR values decrease slightly when the timing offsets increase, due to the cyclic property of the FFT. However the SNR level is high, making it possible to factorize the FFT (as in synchronous CP-OFDM), which means than one FFT can be carried out at the receiver in the UL to recover the signals from all users.

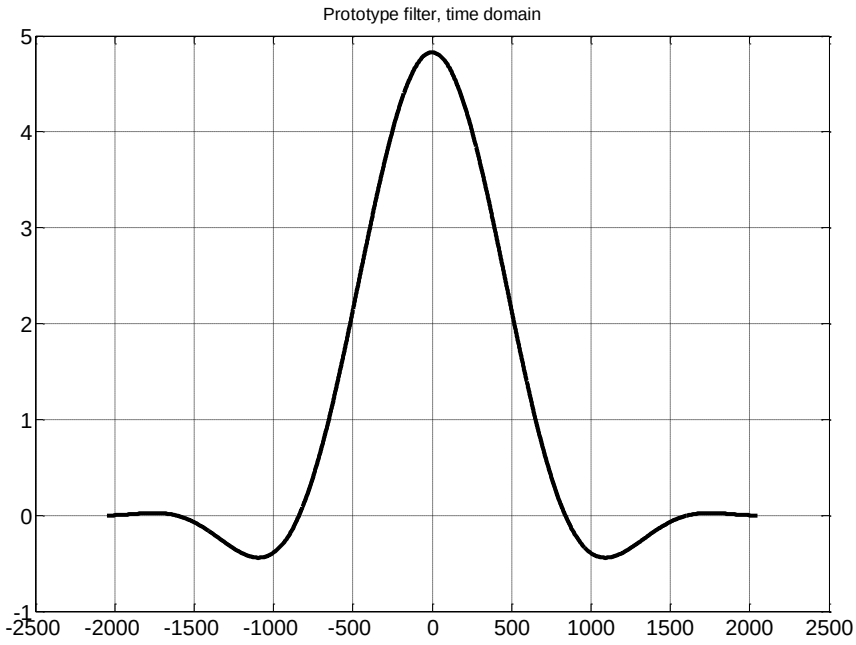

Figure 2.3.7. Example of a prototype filter

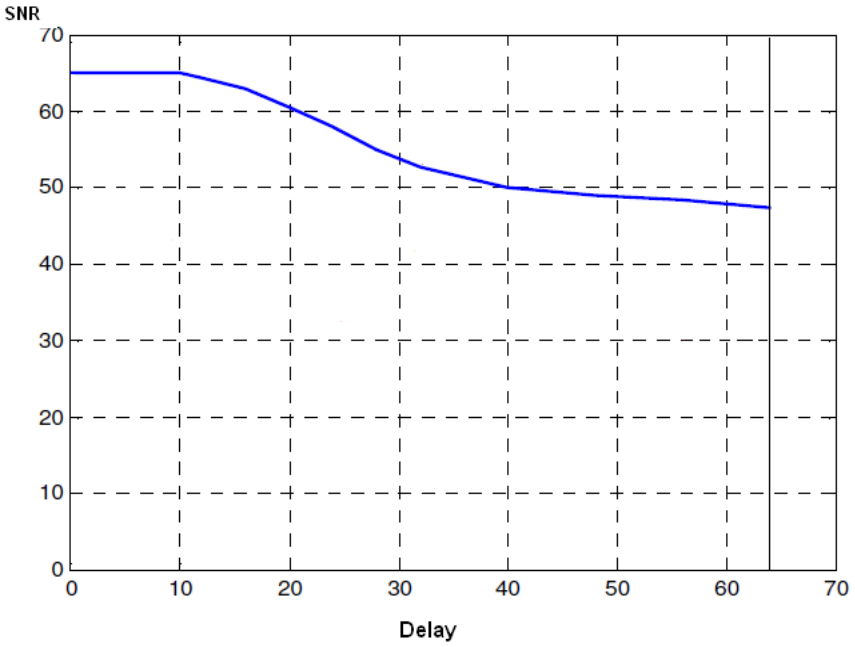

Figure 2.3.8. SNR (dB) vs delay for a FBMC K=4, N=128. Inspired from [BEL12]

In [BEL12], the author compared this implementation with the classical one, consisting in filtering in the time domain using a polyphase network (PPN). A 7 taps equalizer was considered. It was shown that the advantage of the frequency domain approach is significant, giving a gain of about 20 dB on the SNR.

The consideration of FBMC waveforms opens new challenges on receiver implementation. In this section we demonstrated that it is possible to "factorize" the FFT processing of non-synchronous users as is done in the classical synchronous OFDMA making the approach particularly suitable for hardware implementations. Obviously, other challenges should be addressed such as time synchronisation in the frequency domain and channel estimation in fragmented spectrum usage. These challenges will be addressed in the next steps of the project.

2.4 BFDM

In the bi-orthogonal frequency division multiplexing BFDM approach the symbols can be perfectly recovered (in the noiseless case, of course). This is achieved by replacing orthogonality with bi-orthogonality of the set of transmit and receive pulses which is a weaker form of orthogonality (see theoretical framework in the appendix A.3). Particularly, transmit and receive (so-called dual) pulses are no longer orthogonal. The BFDM approach is well suited to the PRACH sporadic access scenario in Section 3.3 since the PRACH symbols are relatively long. Side effects such as spectral regrowth due to periodic setting when calculating the bi-orthogonal pulses are negligible.
The concatenation of BFDM and several OFDM symbols together requires a good tail behaviour of the transmit pulse in order to keep the distortion to the payload carrying subcarriers in PUSCH small. Conversely, the dual pulse which accounts for the distortion of PUSCH onto PRACH can be controlled by iterative interference cancellation (if necessary). This alleviates the typical problem of controlling time/spectral localization of pulse and dual pulse.

BFDM will be best explained along the specific PRACH setting as described next. Note that all technical details for this section (pulse properties, pulse design, elements of multicarrier theory, channel spreading functions, ambiguity functions etc.) and new analytical results of this section are summarized in Appendix A1 to A3.

2.4.1 Transmitter

2.4.1.1 Preamble Generation

The preamble signal in the standard LTE Physical Random Access CHannel (PRACH) is constructed by a Zadoff-Chu sequence, which is defined as

$$x_u[m] = exp\left\{-j\,\frac{\pi\, u\, m\,(m+1)}{N_{ZC}}\right\}, 0 \leq\ m \leq \mathrm{N}_{ZC}\ - 1 \qquad (2.4.1)$$

where u is the root index and N_{ZC} is the length of the sequence. This Zadoff-Chu sequence has a constant amplitude and a good autocorrelation property, that is the periodic correlation with itself is zero except at lag $m = 0$. Similarly, the correlation between the cyclic shift version of this sequence has only a peak at a certain lag N_{CS}, where N_{CS} is the shift offset. We take benefit from this property to build possibly orthogonal preambles by cyclic shifting the ZC sequence. The resulting preamble is given as

$$x_{u,v}[m] = x_u[(m + v\,N_{CS}) mod\ N_{ZC}, \qquad (2.4.2)$$
$$v = 1, \ldots, \left\lfloor \frac{N_{ZC}}{N_{CS}} \right\rfloor$$

where v denotes the cyclic shift index. At most a number of $\left\lfloor \frac{N_{ZC}}{N_{CS}} \right\rfloor$ preambles that can be generated from the same root u. As long as the number of preambles generated from one root is not yet sufficient, the next root index will be taken until all required preambles are obtained. But in that

case, we obtain non-orthogonal preambles. To maximize the number of preambles from different root sequences with acceptable cross correlation property, N_{CS} and N_{ZC} should be chosen as coprime, which is guaranteed if the sequence length N_{ZC} is a prime [STB09].

2.4.1.2 Modulator

We compare two types of PRACH-signal transmission methods, namely we compare the standard PRACH, which uses SCFDMA modulator [1], and a novel PRACH using pulse shaped SCFDMA. Both methods have the following processing stages, which are also depicted in Figure 2.4.1 and Figure 2.4.2.

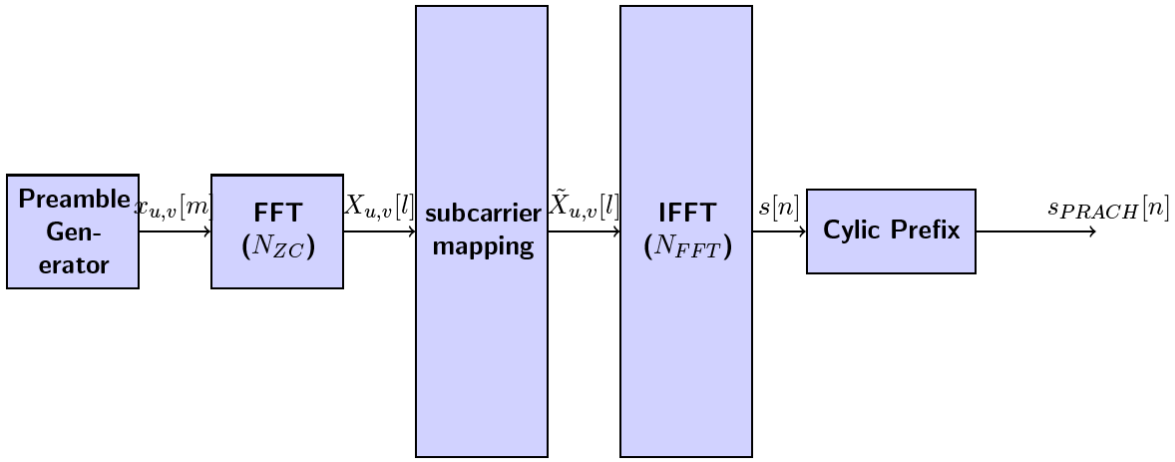

Figure 2.4.1 PRACH SCFDMA Transmitter

At first, every user chooses randomly an integer number from the available set of signatures, to which a preamble is assigned. In LTE, the available signatures of contention based RACH procedure are derived for each cell from the set of integer number $[1,\ldots,64-N_{cf}]$, where the number of reserved signatures N_{cf} is determined by [STB09]. The generated complex valued preamble $x_{u,v}[m]$ is then fed to the FFT of length N_{ZC}, which gives us the frequency representation of

$$X_{u,v}[l] = \sum_{m=0}^{N_{ZC}-1} x_{u,v}[m]\ e^{-j\frac{2\pi\, ml}{N_{ZC}}}. \quad (2.4.3)$$

It is mapped to the allocated subcarriers (1.08 MHz, that is 864 PRACH subcarriers of 1.25 kHz, corresponding to 72 PUSCH) and passed through an IFFT of length $N_{FFT} = 24576$, such that we have

$$s[n] = \sum_{l=q}^{N_{ZC}} \tilde{X}_{u,v}[l] e^{-j\frac{2\pi nl}{N_{FFT}}}, 0 \le n \le N_{FFT}, \quad (2.4.4)$$

where q indicates the location of subcarriers. In our PRACH q follows this subcarrier mapping rule

$$\tilde{X}_{u,v}[q] = \begin{cases} X_{u,v}[l]\ for\ N_{FFT} - N_{ZC}/2 - 1 < q < N_{FFT} + N_{ZC}/2 \\ 0\ otherwise \end{cases} \quad (2.4.5)$$

It maps each FFT output $X_{u,v}[l]$ into subcarriers in the center of the spectrum. For the standard-PRACH samples of length N_{cp} from the end are appended to the front as cyclic prefix. To allow a longer propagation delay a guard time at the end of preamble is inserted, which consists of zeros. At the output, the discrete baseband transmit signal of one symbol duration can be written in closed form as

$$s_{PRACH}[n] = \beta \sum_{l=q}^{N_{ZC}+q-1} \tilde{X}_{u,v}[l]\ e^{-j\frac{2\pi nl}{N_{FFT}}},\ 0 \le n \le N_{FFT} + N_{cp} + N_g, \quad (2.4.6)$$

where β is the amplitude scaling factor for customizing the transmit power.

2.4.2 Pulse shaped PRACH

Additional processing is needed for pulse shaped PRACH [SMH02]. In contrast to previous methods, we process more than one symbol interval, even if we use only one symbol to carry a preamble.

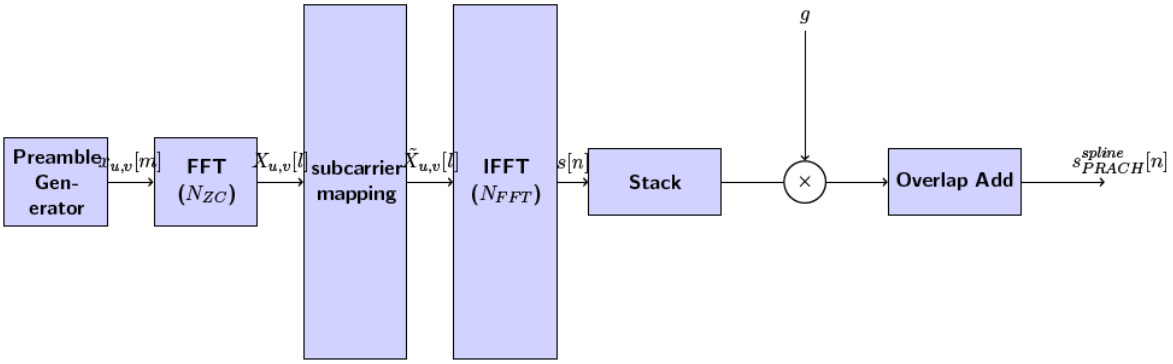

Figure 2.4.2 PRACH Pulse shaped transmitter

As depicted in Figure.2.4.1, we have the output signal $s[n]$ after the IFFT stage. We extent $s[n]$ by repeating it and taking the modulo P to get the same length as the pulse g. For K symbols, we stack the k-th symbol $s_k[n]$ as a row vector in a matrix

$$S = \begin{pmatrix} s_0[n] \\ s_1[n] \\ \vdots \\ s_{K-1}[n] \end{pmatrix}, S \in \mathbb{C}^{K \times P}, \tag{2.4.7}$$

where P is the length of pulse g. Then each of them are pointwise multiplied by the shifted pulse g and superimposed by overlap add, such that we get

$$s_{PRACH}^{pulse}[n] = \sum_{k=0}^{K-1} s_k[n] g[n - kN]. \tag{2.4.8}$$

By neglecting the ZC-sequence indices u and v, we have

$$s_{PRACH}^{pulse}[n] = \beta \sum_{k=0}^{K-1} \sum_{l=q}^{N_{\{ZC\}}+q-1} \check{X}_{k,l}\, g[n - kN] e^{j\frac{2\pi nl}{N_{FFT}}}, \tag{2.4.9}$$

where $\check{X}_{k,l}$ is the Fourier transformed ZC-sequence at the corresponding k −th symbol and l-th subcarrier and β is the amplitude scaling factor.

To pursue the maximal spectral efficiency, which is defined as $\eta = \frac{1}{TF}$, we prefer to have $TF \approx 1$. With given N_{FFT}, this can be achieved if the time shift $N$is approximately equal to N_{FFT}. But at $TF = 1$, due to the Balian-Low theorem, we cannot obtain a well localized pulse. To trade off between spectral efficiency and pulse localization we choose $TF = 1.25$ or $\eta = 0.8$. The rules of thumb for such design are given in appendix A.3.

2.4.1.3 B-spline / Gauss based pulse

We construct our pulse based on the B-spline in the frequency domain (see appendix A.2), considering that using B-spline we can also establish a Gabor Riesz basis and its corresponding dual Riesz basis (see appendix A.3. The only requirement for perfect symbol reconstruction is that the basis functions generating the transmit signal set form an incomplete Riesz basis. There are many Riesz bases, but we choose the one which intuitively can facilitate our task. The second order B-spline in frequency domain is given by

$$B_2(f) = B_1(f) * B_1(f), \tag{2.4.10}$$

where $B_1(f) := \chi_{\left[-\frac{1}{2},\frac{1}{2}\right]}(f)$.

The transmit pulse is then given as

$$g(t) = \left(\frac{\sin(B\pi t)}{B\pi t}\right)^2 \chi_{[-N_p,N_f]}(t). \tag{2.4.11}$$

This setting is compared to the standard transmit Gauss pulse given by $g(t) = e^{-B\pi t^2}$, where B is chosen equal to $4\,\Delta f$. The B-spline pulse has been shown in appendix A.2 as almost optimal in terms of tail properties with respect to the L_1norm. We believe that the better tail behavior is beneficial with respect to the overlap of PRACH to the PUSCH symbols.

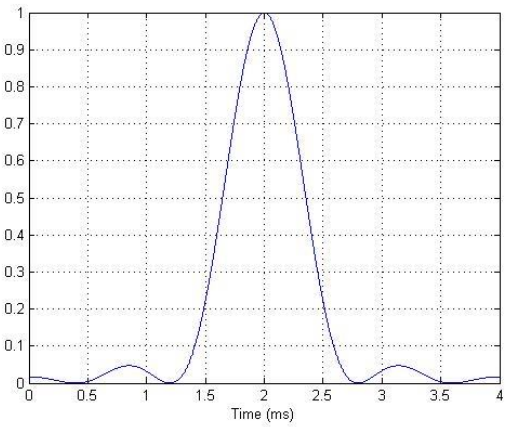

Figure 2.4.3 Spline transmit pulse , TF=1.25

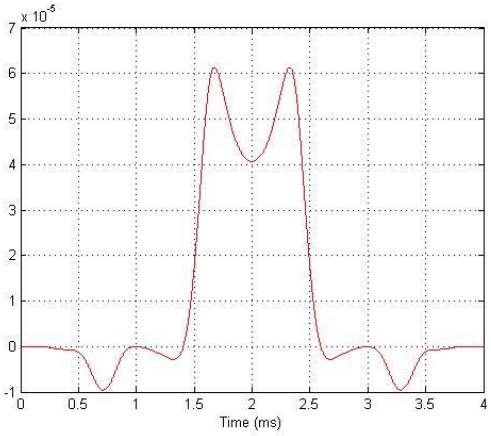

Figure 2.4.4 Gauss transmit pulse , TF=1.25

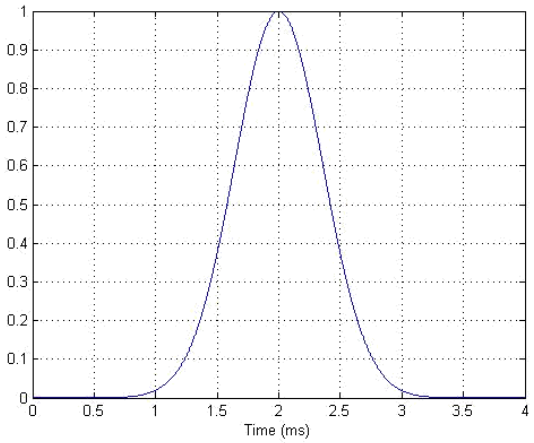

Figure 2.4.5 Spline receive pulse , TF=1.25

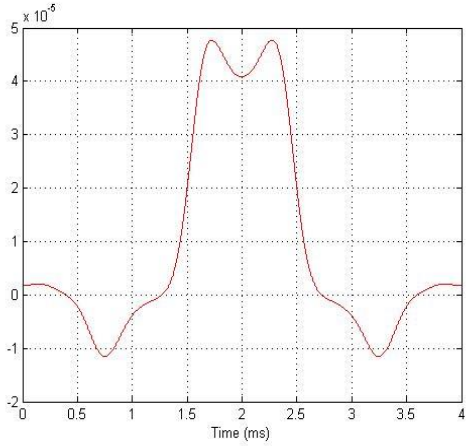

Figure 2.4.6 Gauss receive pulse , TF=1.25

We use the dual pulse of g as the receive pulse which is biorthogonal to g and denoted by γ. For the computation of γ the LTFAT toolbox can be used which implements a quite efficient algorithm [Son12]. In the finite discrete setting, the length P must hold $P = aK = bN_{FFT}$, where $a \in \mathbb{N}$ is the discrete time shift and $b \in \mathbb{N}$ is the discrete frequency shift. By given N_{FFT} and a, we can choose any length P which is jointly divisible by K and b. The shortest one is the $lcm(N_{FFT}, a)$, the least common multiple of N_{FFT} and a. The pulse length we obtain is $P = lcm(24576, 30720) = 122880T_s$ which equals to 4 LTE subframes.

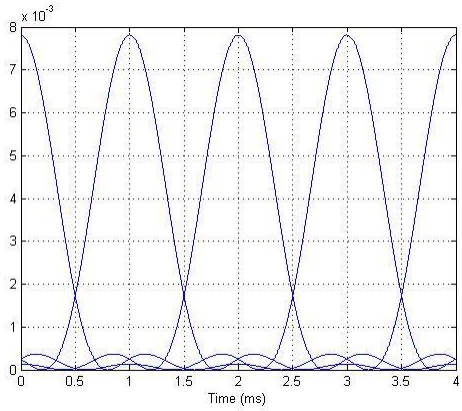

Figure 2.4.7 Cyclic shifted spline pulse

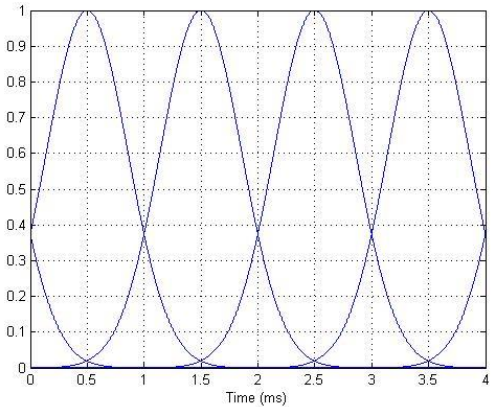

Figure 2.4.8 Cyclic shifted Gauss pulse

In Figures 2.4.2-2.4.7 we illustrate the time characteristics of those pulses, their regarded dual pulses and their shifted version. To observe their properties against the time-frequency distortions, the ambiguity functions are also depicted in Figures 2.4.8-2.4.11. The discrete ambiguity function of the pulse g is given as

$$A_{g,g}(\tau,\nu) = \sum_n g[n]g^*[n-\tau]e^{j2\pi\nu n}, \quad (2.4.12)$$

and the discrete cross-ambiguity function between pulse g and γ is given as

$$A_{g,\gamma}(\tau,\nu) = \sum_n g[n]\gamma^*[n-\tau]e^{j2\pi\nu n}\,. \quad (2.4.13)$$

Let us denote the maximum Doppler F, the maximum delay T, the Doppler grid number K and the delay grid number N on each side. The distance between the grids is given by

$$\Delta\tau = \frac{T}{N}\,P\,T_s \quad (2.4.14)$$

$$\Delta\nu = \frac{F}{K}\,\frac{1}{P} \quad (2.4.15)$$

where P is the pulse length. For subsequent figures we choose $F = 20$, $K = 40$, $T = 1$ and $N = 40$, such that we have $\Delta\tau$ ms and $\Delta\nu$ = 125 Hz.

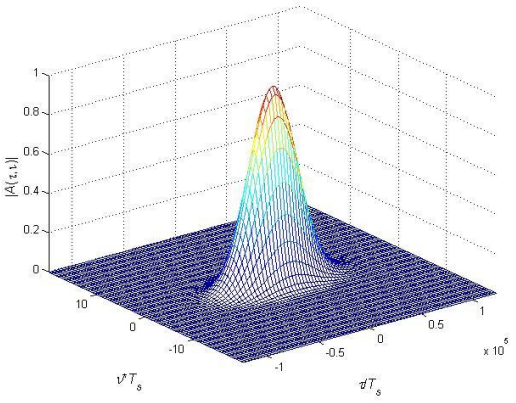

Figure 2.4.8 Ambiguity function of Gauss pulse

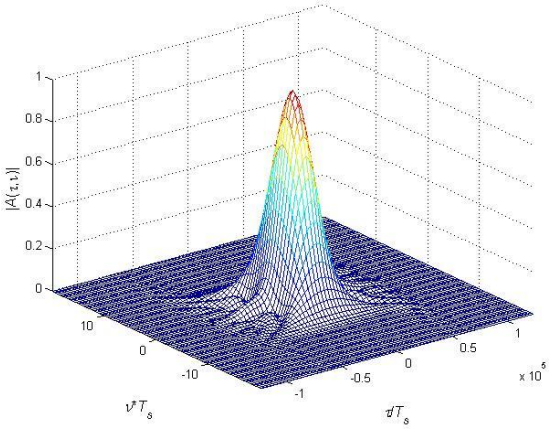

Figure 2.4.9 Ambiguity function of spline pulse

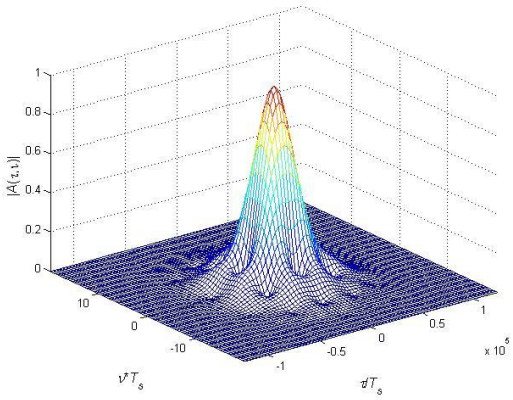

Figure 2.4.10 Cross ambiguity function of Gauss pulse

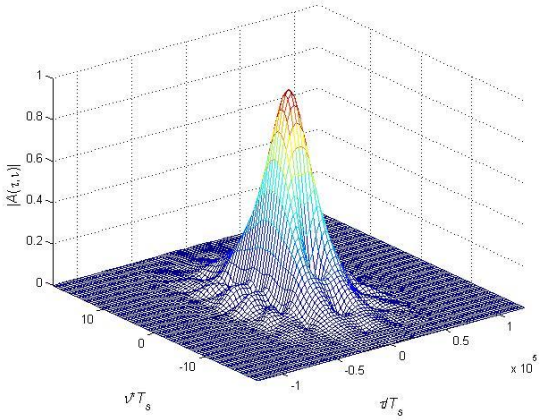

Figure 2.4.11 Cross ambiguity function of spline pulse

2.4.3 PUSCH

On the PUSCH the synchronized data bearing signal are transmitted using the Single Carrier Multiple Access (SC-FDMA) scheme. We have 16-QAM modulated data symbols, which are fed to FFT before passed through IFFT. The localized subcarrier mapping is used to share the available number of subcarriers among users. In simulations the length of the FFT depends on the number of users. To minimize the inter symbol interference a cyclic prefix is also appended. The baseband transmit signal on the PUSCH is expressed by

$$s_{PUSCH}[n] = \sum_{k=0}^{K-1} \sum_{l=q}^{l=L+q-1} \sum_{m=0}^{M-1} x_{k,l,m}\,[n - k(N_{FFT} + N_{CP})]\, e^{\frac{-j\,2\pi ml}{M}} e^{\frac{j\,2\pi nl}{N_{FFT}}}, \quad (2.4.16)$$

where M is the FFT length.

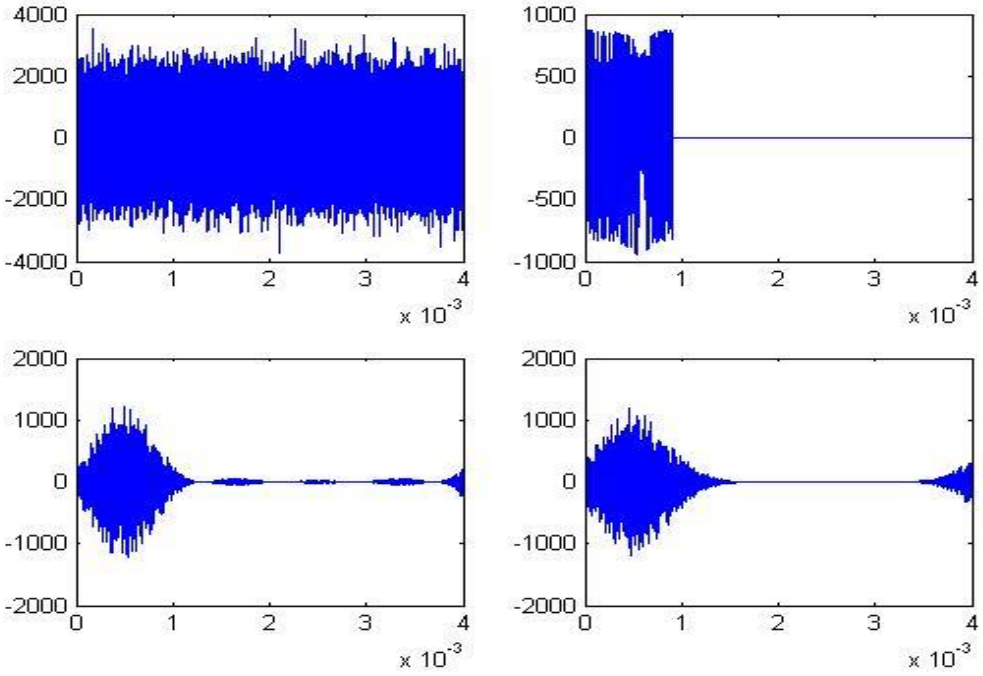

Figure 2.4.2 Transmit signal. From left clockwise: PUSCH , standard , Gauss and Spline PRACH

2.4.4 Receiver

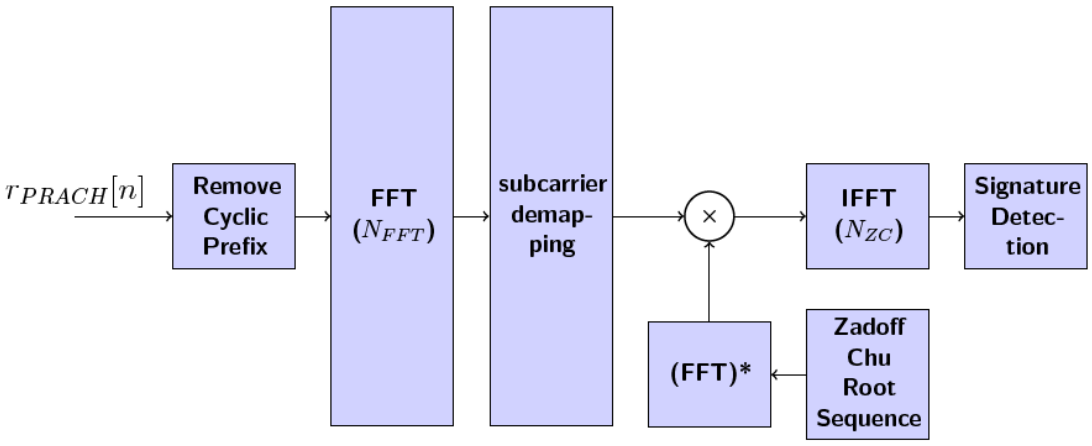

Figure 2.4.3 Standard PRACH receiver

We compare two base stations, each of which has a different receiver structure. The first base station has a SCFDMA demodulator. The second base station has a pulse shaped SCFDMA demodulator, which uses the Biorthogonal pulse γ. We omit the processing time at the transmitter as well at the receiver. Both of them have the same observation timing start $t = 0$, so that the resulting delay stems only from the propagation delay. They have also the same observation window of length 4 ms. The receive signals are given by

$$r_{PRACH\}}[n] = \sum_{m=1}^{L_{ch}} h[m]\, s_{PRACH}[n-m] + n_o[n], \quad (2.4.17)$$

$$r_{PRACH}^{spline}[n] = \sum_{m=1}^{L_{ch}} h[m]\, s_{PRACH}^{spline}[n-m] + n_o[n], \quad (2.4.18)$$

$$r_{PUSCH}[n] = \sum_{m=1}^{L_{ch}} h[m]\, s_{PUSCH}[n-m] + n_o[n], \quad (2.4.19)$$

where $h[m]$ is the channel of length L_{ch} and n_o is the Gaussian noise. The difference between the two receivers lies only on the processing before the FFT operation. The first base station first removes the received signal $r_{PRACH}[n]$ from the cyclic prefix and then performs the FFT, whereas the second base station first performs an operation to invert the pulse shaping at the transmitter. This operation consists of first arranging the K copies of received signal $r_{PRACH}^{spline}[n]$ as row vector in matrix

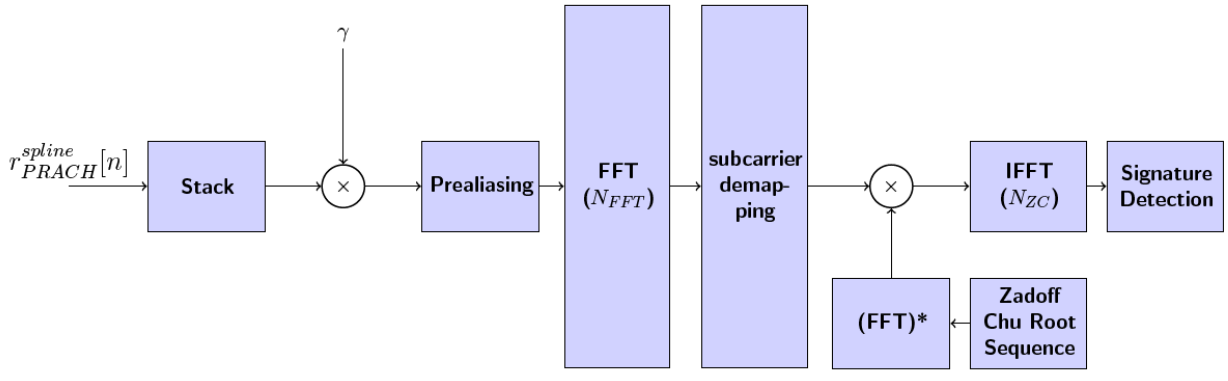

Figure 2.4.4 Pulse shaped PRACH receiver

$$R = \begin{pmatrix} r_0[n] \\ r_1[n] \\ \vdots \\ r[n] \end{pmatrix}, R \in \mathbb{C}^{K \times P}. \quad (2.4.20)$$

Afterwards each row is pointwise multiplied by the shifted receive pulse γ, such that we have

$$r_k^{\gamma}[n] = r_k[n]\, \gamma[n - kN]. \quad (2.4.21)$$

Further we do a kind of prealiasing operation to each windowed $r_k^{\gamma}[n]$

$$\tilde{r}_k^{\gamma}[n] = \sum_{l=0}^{P/N_{FFT}-1} r_k^{\gamma}\ [n - lN_{FFT}], \quad (2.4.22)$$

such that we can obtain the Fourier transformed preamble sequence at k-th symbol and l-th subcarrier after doing the FFT operation

$$\tilde{Y}_{k,l} = \sum_{n=0}^{N_{FFT}} \tilde{r}_k^{\gamma}[n] e^{\frac{-j\,2\pi nl}{N_{FFT}}} \quad (2.4.23)$$

Although we do not employ a cyclic prefix like in standard PRACH, the time frequency product of TF$= 1.25$ and $T > F$ allows the signal to also have temporal and frequency guards. This time-frequency guards and the overlapping of the pulses evoke the received signal to be cyclostationary [Böl01], which gives the same benefit as the cyclostationarity made by cyclic prefix. Furthermore, it is also shown in [Böl01], that the biorthogonality condition of the pulses is sufficient for the cyclostationarity and makes it possible to estimate the symbol timing offset from its correlation function.

2.4.5 Simulation Results

The SNR is given as the ratio of the received signal power to the noise power

$$SNR = \frac{P_s}{\sigma_n^2}, \quad (2.4.24)$$

where $P_s = \frac{1}{N_s}\sum_{n=1}^{N_s}|s[n]|^2$ is the power of the transmitted signal of length N_s and σ_n^2 is the noise variance. The noise is randomly generated with zero mean and standard deviation according to the configured SNR. The noise n_0 is then added to every sample of the signal s[n] to obtain the received signal

$$r[n] = s[n] + n_0[n]. \quad (2.4.25)$$

The transmit powers of PRACH and PUSCH are scaled such that a consistent power spectral density is achieved. Figure 2.4.12 shows the symbol error rate in the PUSCH for an AWGN channel with one user and single antenna communication. Different numbers of data subcarriers in D-PRACH are considered. Further the number of sub-frames $K = 4$. The symbol error rates are calculated only for the first sub-frame. In ongoing simulations we also investigate the influence of D-PRACH on PUSCH in subsequent sub-frames. Figure 2.4.13 shows the symbol error rates of the subcarriers used for data transmission in D-PRACH. Here both 10 subcarriers and 20 subcarriers are used for data transmission. A significant difference in the performance of the new pulses compared to the performance of the standard pulse can be observed. Simulations for multipath channels show a similar behaviour than that shown in Figures 2.4.12. and 2.4.13. Figure 2.4.14 depicts performance results regarding signature detection. The probability of misdetection (a transmitted preamble is detected wrong or not at all) is shown for different SNR values. We say a peak is detected if it has a value above the threshold D given by $D = k_{tr}N_0$, where k_{tr} is the adjustment factor and N_0 is the average noise floor of all received preamble samples that lie over a threshold $\widetilde{N_0}$. We choose

$$\widetilde{N_0} = \frac{1}{N_{ZC}}\sum_{n=1}^{N_{ZC}} |z(n)| \quad (2.4.26)$$

The figure shows that the misdetection probability with the new PRACH approaches is comparable to that of the standard PRACH.

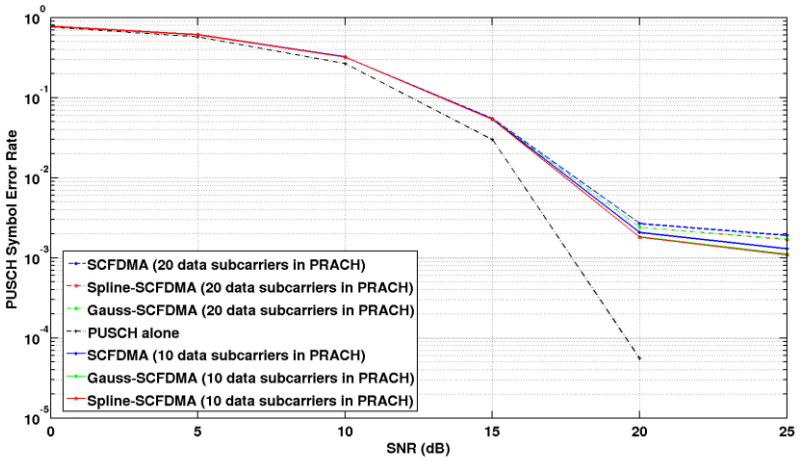

Figure 2.4.12 Symbol Error Rate in PUSCH for different PRACH vs. SNR

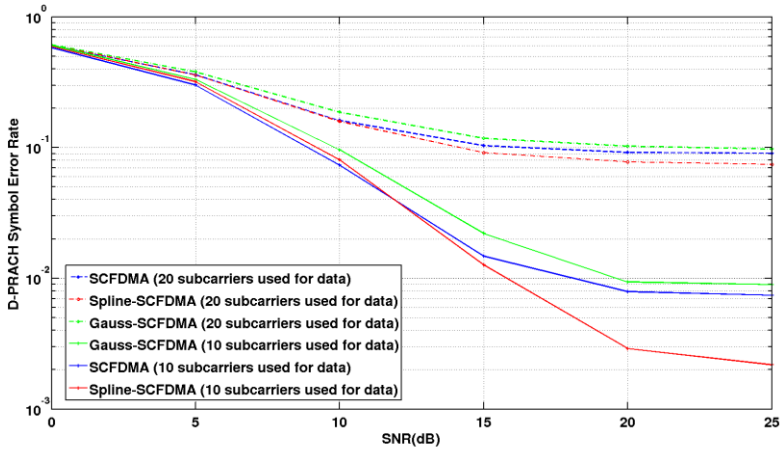

Figure 2.4.13 Symbol Error Rate in D-PRACH vs. SNR

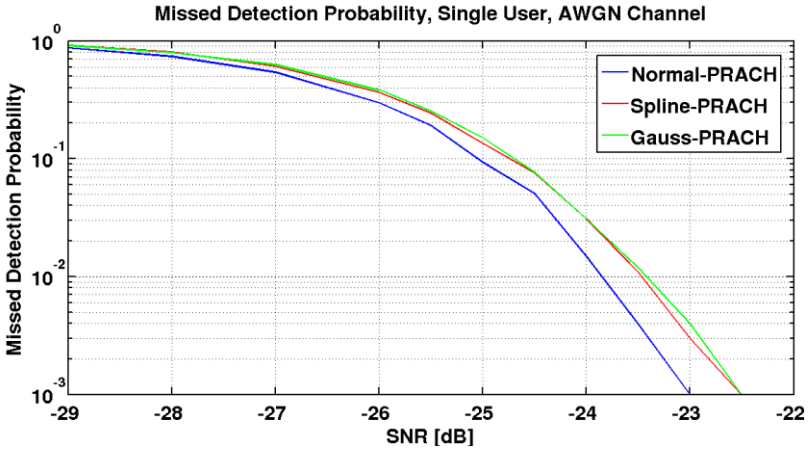

Figure 2.4.14 Missed Detection Probability of different C-PRACH

3 Multiple Access Vision and Impact on Waveforms

With the steady increase of handsets (smart phones, tablets) and with the advent of the internet of things – introducing a myriad of sensor/actor devices potentially accessing the wireless cellular communication network sporadically – it becomes clear, that many procedures of communication networks as applied nowadays (4G) have to be rethought.

There are many issues related to this. The most prominent one stems from the bulky closed-loop ranging process of LTE. With LTE a device entering a network has to follow a bulky ranging protocol including several message exchanges between device and network to become tightly synchronized with respect to timing and carrier frequency. With only few devices accessing the network closed-loop synchronization is a reasonable approach, however, once this number climbs significantly as indicated above, the channels used for the message exchange either become highly congested or have to be extended accordingly, digging heavily into the precious bandwidth resources.
Another issue is related to the high energy consumption connected to closed-loop synchronization. The Internet of Things will consist to a high extend of sensors/actors being installed without the intention of spending regular maintenance visits. So, energy consumption needs to be as low as possible for guaranteeing long battery life-cycles ruling out closed-loop synchronization.

5GNOW pursues a new concept relaxing the strict paradigm of high synchronicity. Various building blocks are required to enable this (the following chapters will detail on this):

- Unified frame structure: We have developed a unified frame structure including various traffic types – ranging from highly synchronized channels for e.g. video traffic of smart phones and tablets still applying closed-loop synchronization to loosely synchronized channels for e.g. sporadic sensor traffic relying only on open-loop synchronization (i.e. only based on preamble measurements, without message exchange).
- Layering: With allowing devices to access the system loosely synchronized, user separation has to be rethought. Conventional approaches such as applied in LTE are not suited very well due to the high amount of multiple access interference.
- Sparsity aware Random Access: To address sporadic traffic as an enabler of the IoT. 5GNOW anticipates a combination of waveform design and sparse signal processing in an extended PRACH to efficiently achieve link acquisition and (possibly small) payload transmission in one shot (subframe).

The main approach of 5GNOW relating to the above considerations is to treat various types of traffic differently, according to specifics of their behavior (e.g. DL hungry, UL only, synchronous, etc.). Thus, taking all the considerations above (i.e. approaches of new frame structure and a new RACH design) on the physical layer, additional aspects are appearing from the multiple access perspective, e.g.:

- Another building block with respect to the unified frame structure concept is feedback that needs to reflect the requirements on the transmission modes. The feedback type may be incorporated in an overall system design to adjust the feedback policy with the corresponding scenario (e.g. CoMP, MTC, single cell bit pipe). The parameters of feedback (e.g. bit rate, quantization and periodicity) shall be adjusted to the type of transmission with respect to required performance / robustness of this traffic type.
- Multiple access scheme including: adaptive frame structure depending on UEs mobility and distance from the eNB. The number of resources could be dynamically adapted within frame structure depending on the traffic type and QoS. While fixing the overall frame size, the

possible parameters for adaptations could be: amount of resources per each traffic type, CP size, subcarrier separation and waveform type.

These aspects will be further elaborated within the 5GNOW project under the MAC framework in WP4.

3.1 Unified Frame Structure

3.1.1 General concept

Figure 3.1.1 depicts schematically the unified frame structure [WKW+13]:

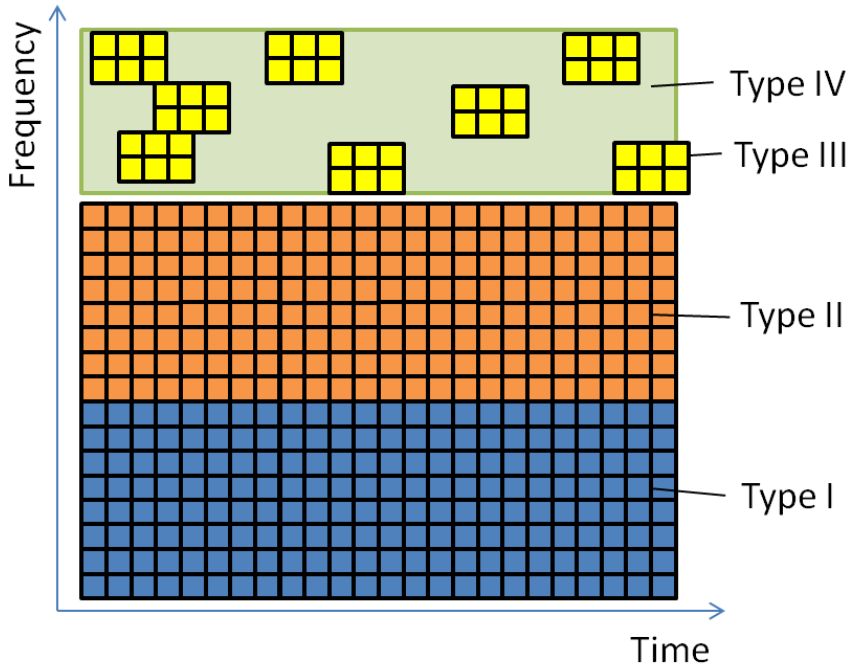

Figure 3.1.1: Unified frame structure

As with LTE today the base of the universal frame structure is a multi-carrier transmission technique (such as presented in earlier chapters). Each rectangle in Figure 3.1.1 represents a single subcarrier. Target of the unified frame structure is to support different sets of requirement and service classes efficiently within a single carrier. To do so, the frame is divided into different areas:

- The type I area carries classical “bit pipe” traffic. High volume data transmissions (e.g. video) lasting long (compared to sporadic sensor transmissions), being rather stationary and not heavily burdened by intercell interference (i.e. not being close to the cell edge or to a small cell) are served here. High spectral efficiency is the key performance indicator to be pursued. The issues connected to closed-loop synchronization mentioned earlier do not apply for this kind of traffic. A high degree of orthogonality and strict synchronism are still of value, here.
- Type II traffic is rather similar to type I traffic. Basically the same service and device classes are supported. In contrast to type I users being confronted with a higher degree of

interference from adjacent cells (cell edge, small cell areas, shaded areas in Figure3.1.2) are assembled here. Key building block for efficient multi-user separation is vertical layering (see next section). Synchronization and orthogonality are not as tight as with type I traffic.

- Type III traffic includes sporadic sensor/actor messages requiring low latencies. As outlined above, closed-loop synchronization is less suited, here. Instead transmissions are only loosely synchronized (open-loop) and a contention-based access technique is used.
- Type IV traffic includes sporadic sensor/actor messages tolerating high latencies. The open weightless standard [Wei] has shown that, from an energy-efficiency perspective, it is beneficial to stretch the transmissions in time by spreading. This additional signal layer, again, can be handled by an IDMA-like approach.

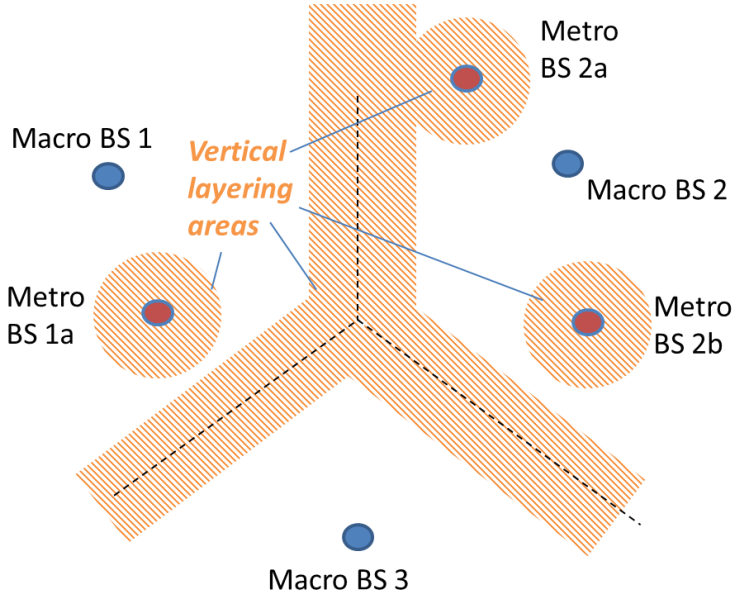

Figure 3.1.2: Areas applying vertical layering.

Naturally, the unified frame structure only becomes efficient, if combined with respectively tailored signal processing. For example the waveform designs proposed in the former chapter need to support this. One of the key characteristics here is the reduced side-lobe behavior common to these proposals compared to conventional OFDM.

The adressed properties of the unified waveform structure mainly impact the uplink by the addition of contention-based data transmission (type III and IV traffic). However, in the downlink, relaxation of synchronicity applies as well in conjunction with CoMP and multi-cell in general, e.g. driven by heterogeneous networks for type II traffic. (Type III and IV traffic might not be relevant for the downlink.)

Research studies in the framework of the unified frame structure will assess the capability of the underlying waveform and multiple access procedure to support the overall concept:

- The capability to separate the different types of traffic is of high importance. As it is only loosely synchronized, type II traffic causes intercarrier interference to adjacent type I traffic. The amount of generated interference depends on the characteristics of the underlying waveform. The achievable improvement by applying UFMC instead of OFDM will be assessed. Means to even improve on this will be proposed.

- Vertical layering for multi user separation (see next section).

In the following we present some initial results regarding the first bullet point. Some initial results regarding vertical layering can be found in the next chapter.

3.1.2 Simulation results

The scenario is as follows:

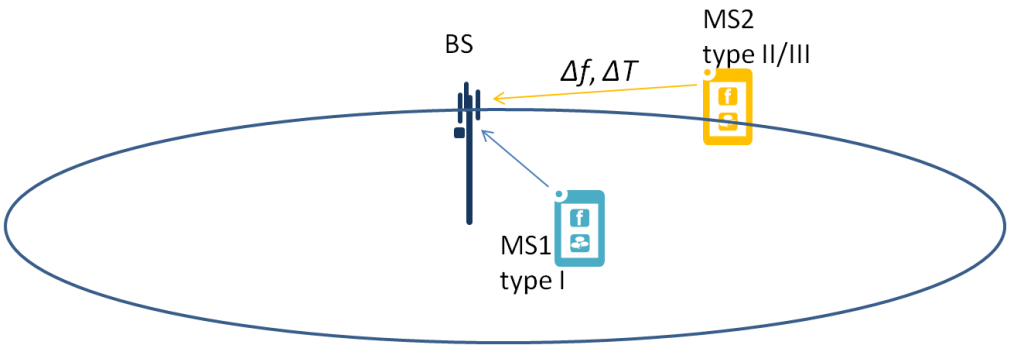

Figure 3.1.3: Simulation setup.

Two mobiles are transmitting data in UL. MS1 is a rather stationary user e.g. watching a video sitting in the park. A rather regular high rate connection is required and thus MS1 is categorized as type I traffic. So, MS1 is tightly synchronized to the serving basestation with the help of closed-loop synchronization. On the other side MS2 is either a mobile on the move being located close to the cell-edge or even a cheap sensor module planning to access the system. So, MS2 corresponds to a type II/III transmission. As discussed above a more loose synchronization is tolerated, only open-loop synchronization has been conducted. Therefore, the transmissions of MS2 potentially are affected by carrier frequency offset and are delayed (as open-loop synchronization is not able to account for round-trip delay) relative to the transmissions of MS1. The two mobiles are concurrently transmitting data using adjacent frequency resources (we assume both transmissions to arrive with the same powers at the basestation). For signal reception the single user receiver described in chapter 2.2 is used. Target of the study is to assess the distortion power (mean squared error, MSE) MS1 suffers due to the transmissions of MS2 comparing UFMC (sidelobe attenuation: 40 dB) and CP-OFDM. The following table summarizes the setup:

Table 3.1.1: Simulation parameters

Simulation Parameter	Value
Subcarriers per PRB	12
FFT size	1024
No. of allocated PRBs, (user of interest/interfering user)	3/9, adjacent in frequency
UFMC filter length / OFDM CP length	80/79 (similar to LTE in terms of overhead)
Frequency Offset in subcarrier spacings	[0, 0.05, 0.1]

Figure 3.1.4 depicts the simulation results.

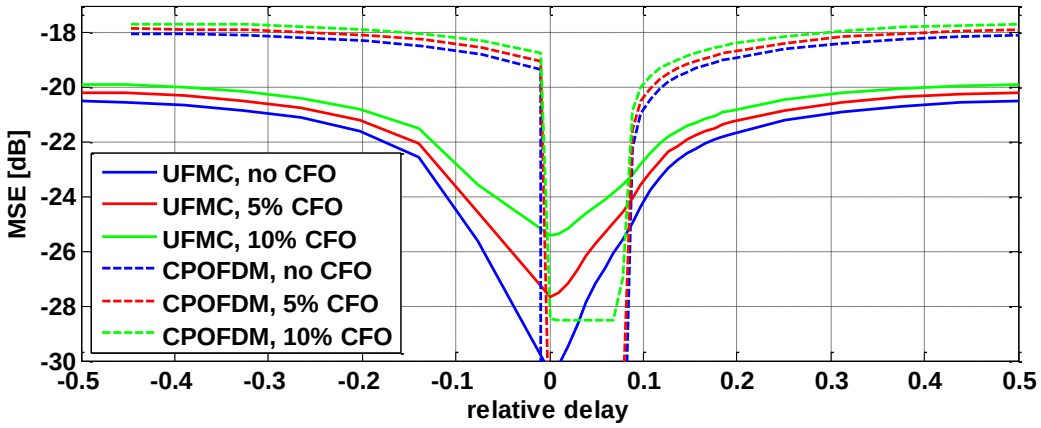

Figure 3.1.4: MSE type I traffic is suffering due to interference originating from type II/III traffic (CFO and delay).

Obviously and as expected, as long as the relative delay stays below the CP length the only source of distortion in case of OFDM is CFO. However, once the delay exceeds the CP length intercarrier interference climbs tremendously. With UFMC distortion climbs smoother with increasing delay. Ultimately, UFMC outclasses OFDM in the given scenario depending on the relative delay and once the CP is infringed at least by more than 2 dB. So, with applying UFMC instead of CP-OFDM the application of open-loop synchronization instead of a closed-loop variant (alike in LTE) for a high amount of devices is more feasible. Thus, messaging exchange may be reduced accordingly reducing the overall overhead tremendously and the energy consumption for sensor/actor devices is at a more tolerable level. With OFDM the symbol is asymmetric due to the cyclic prefix being completely at the beginning of the symbol. With UFMC the symbol is symmetric (ramp up and ramp down areas of the symbol). This feature becomes apparent when inspecting the figure. In a later deliverable we will make use of this.

3.2 Layering

Firstly, let's briefly review the history of processing techniques over multiple signal layers within an asynchronous communication system. In [PLW+02], [PWL+02], [PLL03] and [PLW+06], a new concept, Interleave-Division Multiple-Access (IDMA) was proposed by Li Ping *et al*. It was motivated to improve the performance of Code Division Multiple Access (CDMA) system in asynchronous communications. Further, the authors provided a turbo-type multiuser detector, which basically considers the statistics of multiple signal layerings, is thus low-complexity, robust against asynchronicity and allows accommodating multiple users. In [KB05] and [KBU12], both multiple access schemes, namely IDMA and CDMA, are compared by Kusume *et al.* basically from the viewpoints of following issues, such as complexity of the receiver, robustness against asynchronicity, tolerance with respect to users' overloading. Both literature sources help us to realize that the simplest receiver, denoted as Elementary Signal Estimator (ESE) by Li Ping *et al.* or denoted as soft rake detector by Kusume *et al.*, delivers an equivalent performance as the much more complex linear receiver for asynchronous users. Additionally, IDMA clearly outperforms CDMA in highly user-loaded scenarios. In [HSF08], Hoeher *et al.* investigated the IDMA system from the practical view points, such as channel estimation [SH05], receiver complexity [MLJ06], [NRS07], even with respect to non-

linear receiver. Recently, IDMA attracts more attention in multicarrier systems, e.g. as investigated in [PFG12] [VSK12].

In this section, we will provide a short review on IDMA system. In Fig. 3.2.1 the general transmitter and receiver structures of an IDMA system, simultaneously accommodating K users, are presented. As addressed in [PLW+02], [PWL+02], [PLL03] and [PLW+06], the key principle of IDMA is the interleavers of K users have to be different from each other.

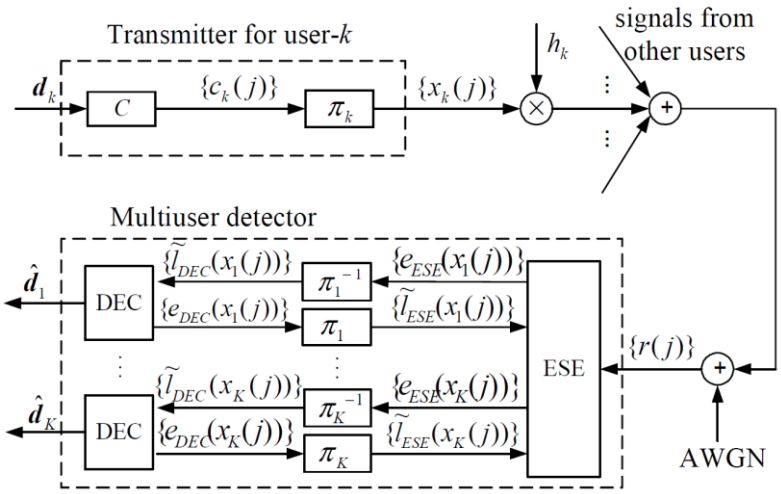

Figure 3.2.1: Transmitter and receiver of an IDMA system (source: [PLL03])

Claimed by Li Ping *et al.* at the very beginning, an information data block $\mathbf{d}_k$ of k -th user has to be encoded by a low-rate code C with code rate R . The corresponding code block is denoted by $\mathbf{c}_k$, with block length J . It is also emphasized that the low-rate code C can be equivalently achieved by concatenating an encoder with code rate R_c with a spreader, a CDMA terminology. As a matter of fact, the spreader mentioned is nothing different than a pattern of repetition for all K users in the system. Let's define the repetition rate as R_r . The overall effective code rate is thus

$$R = R_c \cdot R_r \,. \tag{3.2.1}$$

The modeling in (3.2.1) relaxes the implementation of an IDMA system and can potentially enhance the performance, because repetition coding can bring in huge diversity gain in the fading environment, jointly cooperating with an interleaver. As a part of the review, let's investigate this issue.

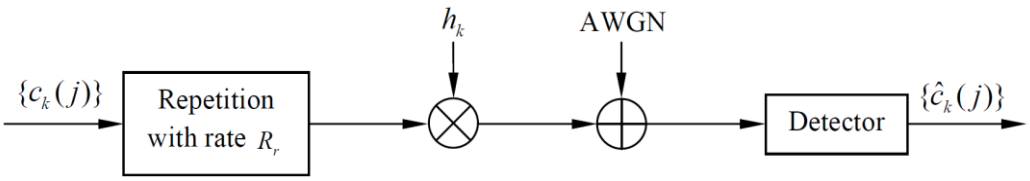

Figure 3.2.2: An equivalent single user system for investigating repetition coding

In Fig. 3.2.2, a single user system is depicted. We focus on the uncoded performance. The zero mean Additive Gaussian White Noise (AWGN) is considered, whose variance σ^2 is modeled by $\sigma^2 = N_0/2$, where N_0 denotes the noise spectral density in units of Watts per Hertz. The channel h_k is assumed to be independent and identically distributed (i.i.d.) complex Gaussian variable with $h_k \sim \mathcal{CN}(0,1)$. This i.i.d. property can be actually achieved by an interleaver, if a long code block is taken into account, although an interleaver is not depicted in Fig. 3.2.2. Hence, Fig. 3.2.2 can be a good reference model, because it is nothing different as separating a single user out of Fig. 3.2.1 and investigating the performance enhancement achieved by repetition coding.

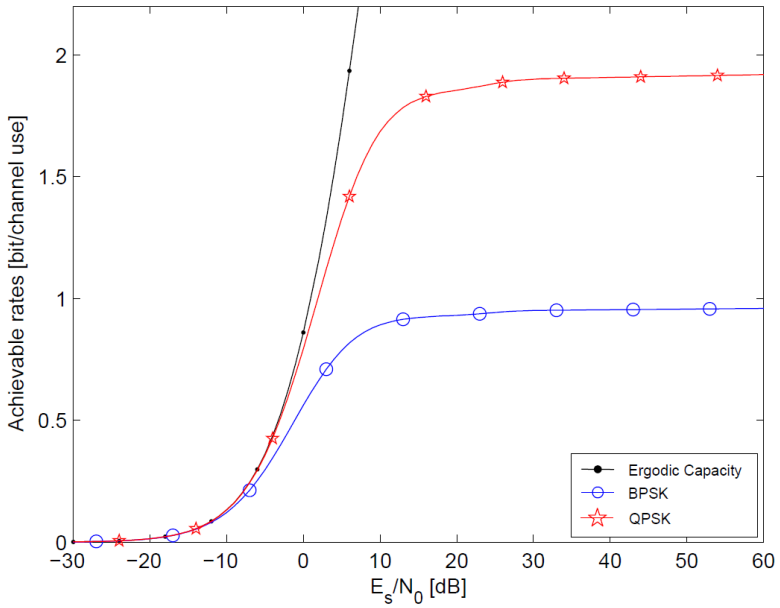

Figure 3.2.3: Achievable rates vs. E_s/N_0, single user system without repetition coding, i.i.d. Rayleigh channel

Firstly, we study the capacity region, as well as the achievable rates, under i.i.d. Rayleigh channel for BPSK and QPSK modulation schemes, as shown in Fig. 3.2.3. E_s/N_0 stands for energy per symbol to noise power spectral density ratio, and E_b/N_0 stands for energy per bit to noise power spectral density ratio, respectively. It holds

$$\frac{E_s}{N_0} = \frac{E_b}{N_0}\log_2 M \cdot \underbrace{R_c R_r}_{R} \tag{3.2.2}$$

where M denotes the number of constellation symbols of a modulation scheme. The ergodic capacity can be computed by

$$C_E = E\left[\log_2\left(1 + \frac{E_s}{N_0}\cdot|h_k|^2\right)\right]. \tag{3.2.3}$$

The achievable rates of single user BPSK and QPSK system can be obtained by evaluating the soft-output values of the detector in Fig. 3.2.2 and computing the bit-wise mutual information [CT06].

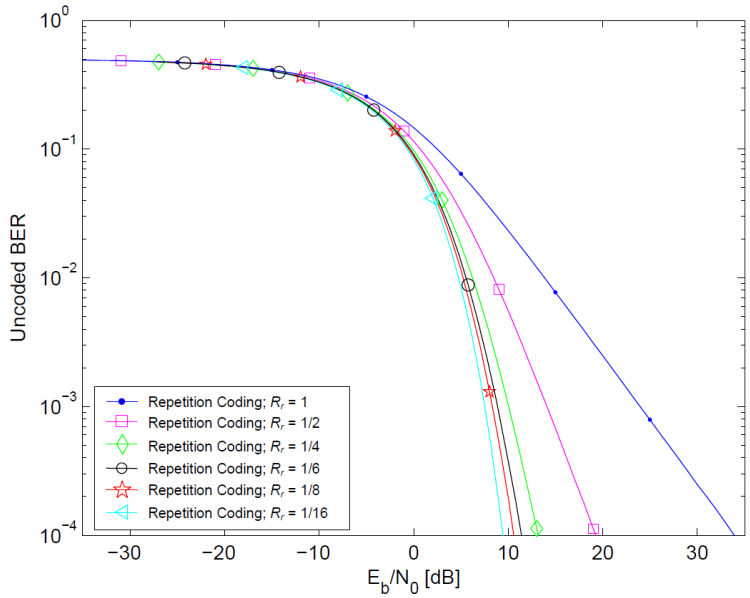

Figure 3.2.4: Single user system, uncoded BER vs. E_b/N_0 with repetition coding, i.i.d. Rayleigh channel, BPSK/QPSK

In Fig. 3.2.4, the uncoded Bit Error Rate (BER) is presented for the single user system, with respect to different repetition rates R_r. We realize, (a) the diversity gain achieved by repetition coding (generating the different visible slopes of the BER curves) will significantly increase for lower target BER, and (b) the BER performance cannot be arbitrarily improved by simply increasing the number of repetitions.

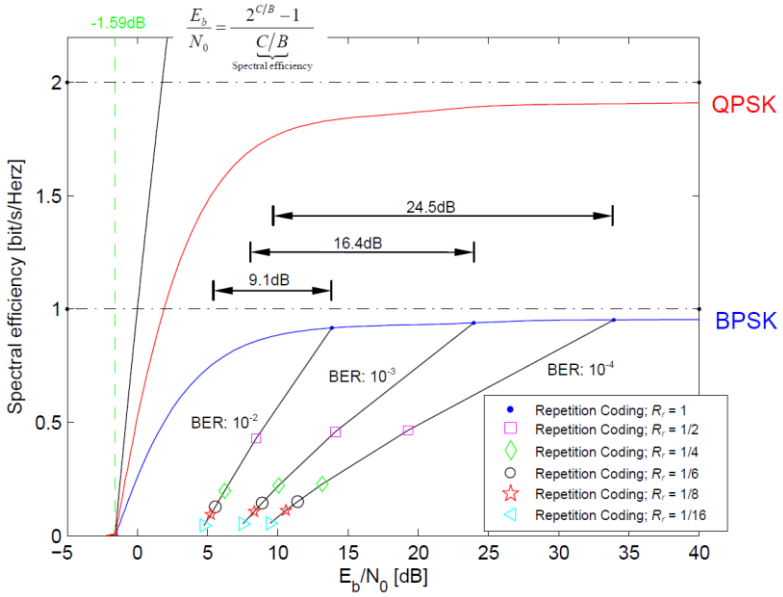

Figure 3.2.5: Single user system, spectral efficiency vs. E_b/N_0 with repetition coding, i.i.d. Rayleigh channel

As a matter of fact, in Fig. 3.2.3, each point on the achievable rates for BPSK/QPSK represents the link performance under a given code rate R. Regarding equation (3.2.2), we are allowed to transform each point in Fig. 3.2.3 to a new figure, which illustrates the spectral efficiency, as shown in Fig. 3.2.5. Furthermore, we also present the spectral efficiency in dependence upon E_b/N_0, which yields an

absolute upper bound at -1.59 dB, if extreme low-rate codes are taken into account, with $R \approx 0$. Assume that we are interested in the target BERs at, e.g. 10^{-2}, 10^{-3} and 10^{-4} in Fig. 3.2.4. We can straightforwardly obtain the E_b/N_0 values and plot them onto Fig. 3.2.5, noticing that the effective code rate $R = R_r$ in the single user system as shown in Fig. 3.2.3. This allows us to observe the diversity gain introduced by repetition coding, for instance, with BPSK modulation scheme.

In Fig. 3.2.6, the simulation model for our investigation on IDMA system is presented. We restrict ourselves to BPSK modulation, but this work can be straightforwardly extended to any high-order modulation scheme. We consider the Low Density Parity Check (LDPC) code with code rate $R_c = 1/4$, which is *soft-in soft-out* and can thus be exploited in the IDMA iterations. A repetition coding with code rate $R_r = 1/4$ is taken into account as well. The channel h_k of k-th user is assumed to experience i.i.d. Rayleigh fading as defined in the sub-system depicted in Fig. 3.2.2 above. Being the key part of IDMA system, the Elementary Signal Estimator (ESE) will be explained in Appendix B.2 in details.

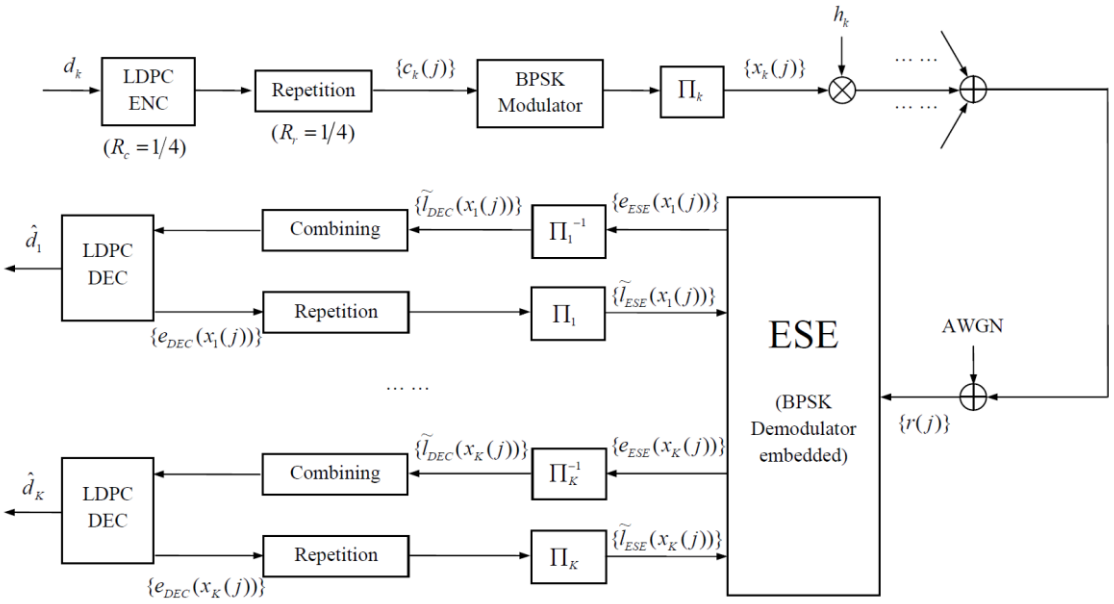

Figure 3.2.6: Our simulation model for investigating an IDMA system

In Fig. 3.2.7, the BER curves are presented for different receivers, with repetition rate $R_r = 1/4$ and channel coding rate $R_c = 1/4$. Firstly, it is very astonishing that LDPC single user bounds of AWGN and i.i.d. Rayleigh are close to each other. This coincides to the information delivered in Fig. 3.2.5. In AWGN channel, the repetition coding will not bring any performance enhancement, and channel coding gain plays a unique role there. In i.i.d. Rayleigh channel, the repetition coding is able to collect diversity gain. Thanks to both channel coding gain and diversity gain, the corresponding performance is therefore very close to the AWGN bound. Secondly, we introduce a reference curve here, namely maximum *a posteriori* probability (APP) detection, which jointly detects the signals of 2 users. APP detector strongly requires synchronicity and its complexity will increase exponentially, depending on the parameters, such as the number of users, the number of constellation symbols of a modulation scheme M. Additionally, the Shannon limit for BPSK at an overall rate $R = R_c R_r = 1/16$ can be obtained in Fig. 3.2.5 as a reference as well. Finally, we present the performance of IDMA system with 2 users, using an ESE receiver. The BER curves of 1st, 2nd and 5th iterations are shown.

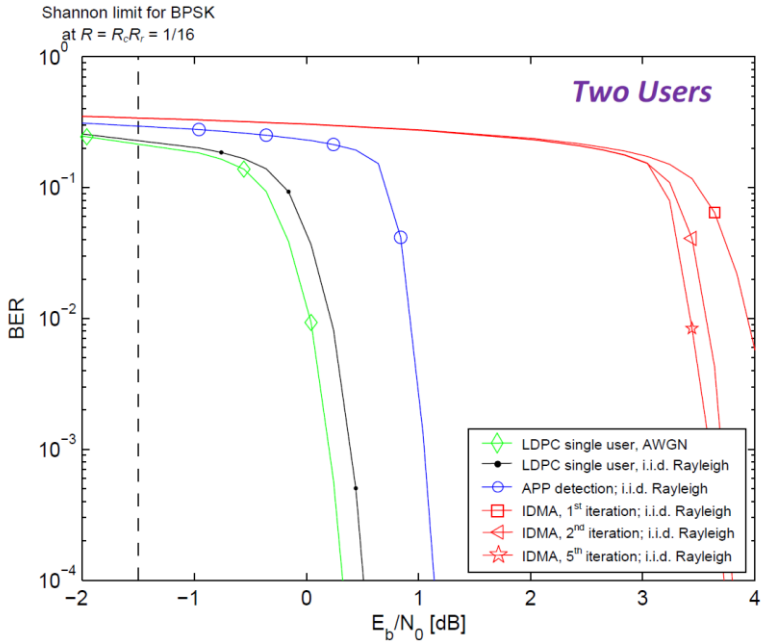

Figure 3.2.7: BER vs. E_b/N_0, 2 users, with repetition $R_r = 1/4$, channel coding $R_c = 1/4$, BPSK

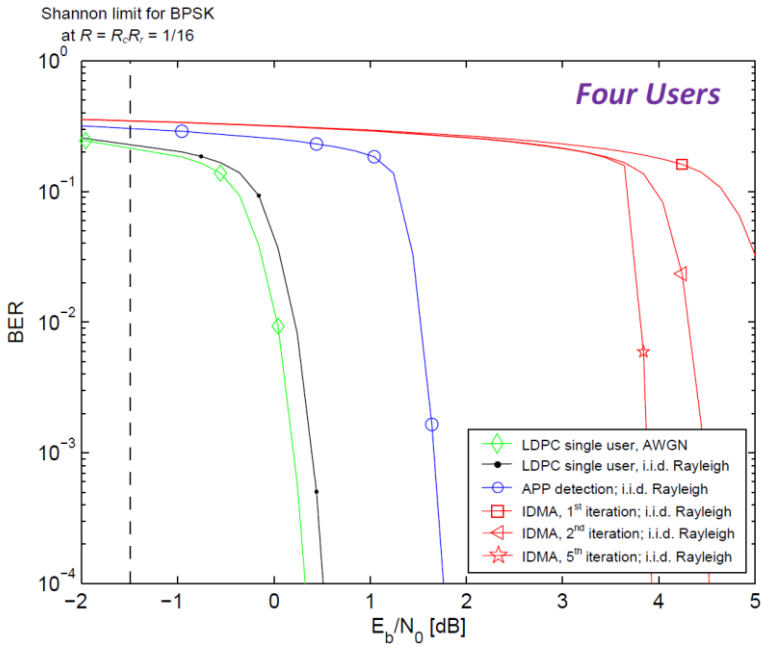

Figure 3.2.8: BER vs. E_b/N_0, 4 users, with repetition $R_r = 1/4$, channel coding $R_c = 1/4$, BPSK

Similarly, in Fig. 3.2.8, we present the BER curves for a multiuser system with 4 users. Especially, the spread of IDMA detector (with ESE) corresponding BER curves becomes bigger, which indicates that the iterations within IDMA system can effectively enhance the performance, by exchanging the soft-output between multiple users within ESE. From another view point, the 2-user and 4-user performance are compared to each other in Fig. 3.2.9. Notice that both APP detector and IDMA detector have certain degradation. Let's focus on BER at 10^{-4}. The degradation of IDMA is 0.28dB, is

thus smaller than that of APP detector. Furthermore, the IDMA 2-user and 4-user performance are expected to converge at lower BER for a given E_b/N_0 .

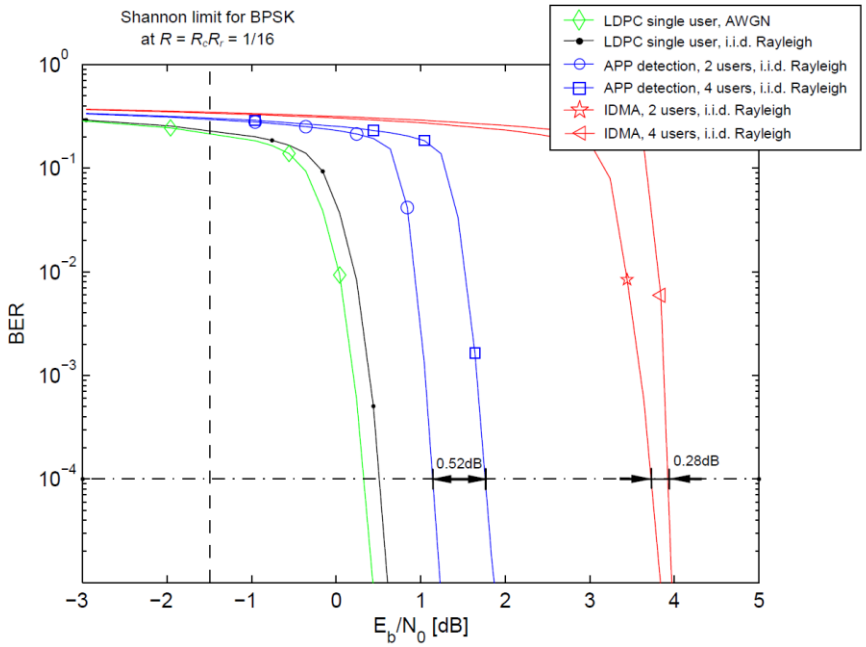

Figure 3.2.9: BER vs. E_b/N_0 , comparing 4 users to 2 users, with repetition $R_r = 1/4$, channel coding $R_c = 1/4$, BPSK

From Fig. 3.2.7 to Fig. 3.2.9, we basically compared an IDMA system (with ESE) to APP detection in a synchronous environment, and presented the relative performance loss, if the number of users increases. Obviously, in an asynchronous environment, the performance of the IDMA system will not change a lot, which becomes clear when looking at the formulation of the ESE in appendix B.2, relying purely on statistical information from other users. Nevertheless, APP detection will have certain technical difficulties, thus will suffer from additional performance degradation.
In the future work, we will try to integrate the IDMA concept to the Universal-Filtered Multi-Carrier (UFMC) technique, in order to support different type of asynchronous communications. On the other side, other practical issues, e.g. channel estimation, can be interesting for investigating the IDMA system.

3.3 Sparsity aware Random Access

3.3.1 Introduction

5GNOW addresses sporadic traffic as an enabler of the IoT. Typical sources for sporadic traffic are short message delivery for smartphones and increasing MTC traffic. The main approach is hereby a combination of waveform design and sparse signal processing in an extended PRACH to achieve efficiently link acquisition (user identification, channel estimation) and (possibly small) payload transmission in one shot (subframe). In the following investigations, for comparison a standard LTE system serves as a baseline. While in standard PRACH data payload is not foreseen and PUSCH and PRACH are separated by orthogonal design, this concept is given up in the new design where a new data section is introduced between synchronous PUSCH and standard PRACH called **D-PRACH (Data-**

PRACH) which allows for asynchronous data traffic To address the data, the D-PRACH is controlled by new **C-PRACH (Control-PRACH)** which substitutes standard LTE PRACH and might overlap with D-PRACH. The bandwidth of both channels shall be determined by higher layers. Note that in the standard LTE approach the D-PRACH would not be used for carrying data, but would simply remain unused as a guard band and then, moreover, C-PRACH equals standard LTE PRACH.

3.3.2 Sparse structured signals

Sparse structured signals are a new viable source for innovation in wireless communication. It is driven by the fact that in many scenarios Nyquist sampling is actually not feasible under the premises of efficient system design and corresponding signaling resources. Sparse signal processing, by contrast, exploits the observation that often the essential number of non-zero elements is much smaller as compared to Nyquist sampling. Here, in our setting, each node sends user plane data and control data to the access point in a contention based form and we assume that channel as well as data is sparse within the total dimensions of the LTE subframe of 1ms. Note that exploiting sparsity in multiuser detection has been thoroughly investigated by [ZG11, HB12, KMB+13] or in case of block sparsity by [EB09]. We will go beyond the state of the art by investigating a joint identification, estimation and detection problem at the same time for the setting.

For the derivation of results we will use the following methodology: suppose X is a vector or a matrix with N elements lying in some (unknown) line subspace or manifold. We get information about X by (noisy) observations of the form

$$\phi_1(\mathrm{X}), \dots, \phi_{\mathrm{M}}(\mathrm{X}), \mathrm{M} \geq 1 \tag{3.3.1}$$

where $\mathrm{M} \ll \mathrm{N}$and X has a representation

$$\mathrm{X} = \sum_{\mathrm{i}=1}^{\mathrm{K}} \alpha_{\mathrm{i}} \psi_{\mathrm{i}} \tag{3.3.2}$$

with $\mathrm{K} < M \ll N$. In many practical cases the dimension of X is not known (e.g. when it is the result of convolution of two sparse vectors. The following standard problems can be stated:

I) Compressed (or compressive) sensing: In the standard form we have linear observations, i.e.

$$\phi(\mathrm{X}) = \Phi\mathrm{X} \tag{3.3.3}$$

and Φ is an M x N matrix. The goal is to recover X from (3.3.3). This problem is well understood and it can be shown that under suitable conditions on the measurement matrix Φ and if $\mathrm{M} \geq \mathrm{c}_0 \mathrm{K} \log(\frac{\mathrm{N}}{\mathrm{K}})$ then X can be recovered by nonlinear optimization.

II) Phase retrieval problem: In this problem class we have

$$\phi_{\mathrm{i}}(\mathrm{X}) = \left|\phi_{\mathrm{i}}{}^{H}\mathrm{X}_{\mathrm{i}}\right| \qquad \text{i=1,…,M,} \tag{3.3.4}$$

where ϕ_{i} is an N vector and the absolute value operation is per measurement. This problem then is to recover X from (3.3.4). The solvability highly depends on the structure of X.

III) Matrix completion problem: In the problem class we have

$$\phi_{\mathrm{i}}(\mathrm{X}) = \mathrm{tr}(\Phi_i \mathrm{X}) \qquad \text{i=1,…,M,} \tag{3.3.5}$$

where Φ_i is an N x N matrix and again the problem is to recover X from (3.3.5).

3.3.3 System model

The system is described in the space/time domain such that the received signal over the coherence slot is given by $\mathrm{Y} \in \mathbb{C}^{\mathrm{nxn_r}}$, hence the receive signal is described jointly over the time domain and receive antenna domain (at the moment set to 1 receive antenna throughout the simulations). For

the sake of exposition we also omit non-orthogonal BFDM design in the mathematical model (please see the BFDM section). On each user antenna m a signal of length $s_m \in \mathbb{C}^n$ is transmitted, so that the equation for n_t transmit antennas (nodes) can be written as:

$$Y = \sum_{m=1}^{n_t} \Phi_m S_m H_m + Z \quad (3.3.6)$$

Here, $S_m = [s_m, T^1 s_m, \dots, T^{n-1} s_m] \in \mathbb{C}^{nxn}$, where T is the periodical downshift shift operator, e.g. $T^1 s_m = [s_m^{n-1}, s_m^0, \dots, s_m^{n-2}]^T$, and $s_m \in \mathbb{C}^n$ is the transmitted sequence of node m. The matrix $H_m = \left[h_1^m, \dots, h_{n_r}^m\right] \in \mathbb{C}^{nxn_r}$ is composed of vectors which themselves contain the coefficients of the channel impulse response (CIR). The matrix Z denotes the additive white Gaussian noise of power σ^2. We assume throughout this work package that compared to n the support of the CIR covers only a small fraction of the vectors. In typical scenarios $h_1^m, \dots, h_{n_r}^m$ is s-sparse, i.e. the support $\mathrm{supp}(i|(h_T)_i \neq 0)$ fulfills $|\mathrm{supp}(h_T)| \leq s$. The exact positions $0 \leq i < m$ where $\left(h_q^m\right)_i \neq 0$ are unknown. The performance to be optimized is the MSE $\mathbb{E}\left\|H_m - \widehat{H}_m\right\|_2$.We will call this a multiple access channel with sparsity constraints (***MAC-SC***) for which we aim to design an optimal receiver.

The following is known: The coherence μ of a matrix A is the largest absolute inner product between any two columns: a_i and a_j of A:

$$\mu(A) = \max_{i<j} \frac{|<a_i, a_j>|}{\|a_i\|_2 \|a_j\|_2} \quad (3.3.7)$$

If

$$k < \frac{1}{2}\left(1 + \frac{1}{\mu(A)}\right) \quad (3.3.8)$$

then for each measurement vector $y \in \mathbb{C}^m$ there exists at most one signal $x \in \Sigma_k$ such that y = Ax.

We investigate basically two algorithms CoSaMP and SPIN. Compressive Sampling Matching Pursuit (CoSaMP) was introduced by Tropp and Needell in [NT10] and is a greedy algorithm based on orthogonal matching pursuit(OMP). It delivers the same guarantees as the best optimization-based approaches. Moreover, this algorithm offers rigorous bounds on computational cost and storage. SPIN (Successive Projections onto INcoherent manifolds) was introduced by Chinmay Hegde and Richard G. Baraniuk in [HB12b]. It is a first-order projected gradient method to recover the multi-user signals, which are in different, possibly non-differentiable sub-manifolds of the signal space.

3.3.4 MAC-SC in standard PRACH

In this setting, C-PRACH equals the standard LTE PRACH. For a single user, the system model reads as

$$\begin{aligned} y &= \underbrace{D \cdot W}_{\Phi} \cdot h \\ &= diag\left(fft(d_{FZC})\right) \cdot W \cdot h \end{aligned} \quad (3.3.9)$$

where $W \in \mathbb{C}^{mxn}$ is taken from the first n columns and central m rows of a $\mathbb{C}^{24576x24576}$ FFT matrix, with entries

$$F_{p,q} = \exp\left(-\frac{i2\pi pq}{24576}\right) \quad (3.3.10)$$

and $p, q = 1,2, \dots, 24576$. This value 24576 is excactly the length of the subframe without CP and guard interval. $d_{FZC} \in \mathbb{C}^{1xm}$ denotes the Frank-Zadoff-Chu (ZC) sequence. In the following we use this periodic model only.

In our first simulation we set the length of the channel n = 300 (delay spread) and the length of the preamble m = 839 (which is the length of the ZC sequence). The value of n was chosen

corresponding to a maximum delay spread of roughly 5µs which corresponds to a cell radius of 1.5 km.

Table 3.3.1: CoSaMP with 1 user, n=300, single tap

Channel Sparsity	Successful recovery rate
1	100%
2	58%
3	4%

In Table 3.3.1 we show the rate of successful channel recovery with varying number of channel taps (*sparsity*). It is shown that CoSaMP can essentially recover 1 path. The coherence of Φ is equal to 0.9981. The result is disappointing since it indicates too bad recovery performance in typical MTC environment, where typically more than one path has to be recovered.

In our second simulation, the non-zero paths of the channel response *h* will be normalized after being multiplied by a factor $e^{-\lambda(p-1)}$. We define p to be the ordinal number of non-zeros. The normalization is performed as follows: Consider a vector v is a k-sparse signal with length 300. Let each non-zero path of v be multiplied by the factor, where p = 1, 2, ... , k, is the ordinal number of the non-zero paths. Using this sparse vector v, we obtain the normalized channel response $h = \frac{v}{\|v\|_2}$. In the simulation $\|h\|_0 = 6$, i.e. we have 6 channel taps. In Table 3.3.2 we show the successful recovery rate when we want the CoSaMP algorithm to recover 1, 2, … non-zero paths from this channel. Here we use a scaling factor of $\lambda = 1$, which means no scaling is used. It can be seen that in this configuration a successful recovery is almost impossible even worsening the results of the first simulation.

Table 3.3.2: CoSaMP with 1 user, n=300, λ=1

Recovered Taps	Successful recovery rate
1 from 6	17%
2 from 6	3%
3 from 6	0%

Table 3.3.3 shows the performance when we increase the value of λ. Obviously the performance increases as expected.

Table 3.3.3: CoSaMP with 1 user, n=300, recover 1 from 6 taps, different scaling

Scaling factor	Successful recovery rate
$\lambda = 4$	94%
$\lambda = 5$	100%

In Table 3.3.4 we show results of simulations with varying number of users. Each user thereby has a channel comprising 6 taps. Again we search for only one tap.

Table 3.3.4: CoSaMP with varying number of users, n=300, λ=5

Recovered Taps	Successful recovery rate
find 1 from 12 non-zeros paths (2 users, each has 6 non-zeros path)	99%
1 from 18 (3 users)	96%
1 from 24 (4 users)	95%
1 from 30 (5 users)	95%
1 from 36 (6 users)	93%

Let us compare the sparse approach to the case of standard lease squared estimation which now also incorporates the D-PRACH. The mathematical model is the same as in the first simulation, i.e. n = 300, m = 839:

$$y = \underbrace{D \cdot W}_{\Phi} \cdot h \tag{3.3.11}$$

Let us define the MSE, which shall be now minimized, as follows:

$$MSE = \frac{1}{n}\left\|W_D h - W_d \hat{h}(y)\right\|_2^2 \tag{3.3.12}$$

Here, the matrix $\boldsymbol{W_D}$ is composed of the c rows before and after W (c=10, 20, 40…) as defined above, and is essentially describing the subcarriers of the D-PRACH.

First we find the condition number of $\Phi^H\Phi$ which is given by

$$\Phi^H\Phi = (DW)^H DW \tag{3.3.13}$$

It turns out that the condition number of $\Phi^H\Phi$ is equal to 2.7774×10^{18}. The rank of $\Phi^H\Phi$ is equal to 30 (it is not a full rank matrix). Next we solve the optimal estimation equation $\Phi^H\Phi\hat{h} = \Phi^H y$

a) In the first case, the estimation will be

$$\hat{h} = (\Phi^H\Phi)^{-1}\Phi^H y \tag{3.3.14}$$

In this situation we can use the pseudo-inverse estimation.

b) In our situation, Φ is ill-conditioned, therefore, we can use Tikhonov Regularization to solve the equation

$$\hat{h} = (\Phi^H\Phi + \Gamma^H\Gamma)^{-1}\Phi^H y \tag{3.3.15}$$

In most situations Γ is an identity matrix. The condition number of $(\Phi^H\Phi + \Gamma^H\Gamma)$ is 2.0619×10^7 and the rank of it is equal to 300.

In the following we calculate the MSE between $W_D\,\hat{h}$ and $W_D h$. Table 3.3.5 depicts the MSE when using different sizes of the matrix W_D. It can be seen that a good estimation performance is achieved up to a size of 320 rows.

Table 3.3.5: MSE between $\boldsymbol{W_D h}$ and $\boldsymbol{W_D\hat{h}}$ for different $\boldsymbol{W_D}$

$\mathbf{W_D} \in$	MSE
$\mathbb{C}^{20x300}$	3.2362×10^{-10}
$\mathbb{C}^{40x300}$	1.0649×10^{-9}
$\mathbb{C}^{80x300}$	9.0816×10^{-8}
$\mathbb{C}^{160x300}$	5.8950×10^{-5}

$\mathbb{C}^{320x300}$	0.0899
$\mathbb{C}^{640x300}$	63.4221
$\mathbb{C}^{1280x300}$	666.1718

The main conclusions of this subsection are:

1. Since too few paths can be recovered in D-PRACH and thus too few users can be supported, the standard PRACH setting must be extended in order to incorporate the envisioned high number of devices.
2. A single user per 1ms can be supported roughly with 320 data subcarriers without extending the standard PRACH. Thereby supported means, that no significant error floor is introduced and the performance depends only on modulation and coding and the SNR conditions.

We are extending the standard PRACH setting in the next section.

3.3.5 MAC-SC with non-standard PRACH

In this setting new C-PRACH is combined with new D-PRACH. Below we investigate a different approach where the D-PRACH and the C-PRACH overlap. Furthermore we choose a certain control sequence at length 839 which can guarantee similar acquisition performance as in standard PRACH. The details are shown in [WJW13] as well as in 5GNOW Deliverable 4.1.

Table 3.3.6 shows the number of taps per user that can be fully reconstructed, depending on the number of users (50 users have been simulated but the processing complexity seems too high at this stage). It can be concluded that with this fully new approach the number of MTC devices in PRACH with data in D-PRACH is mostly limited by the receiver processing.

Table 3.3.6: Number of taps that can be reconstructed per user, depending on total number of users in D-PRACH

Number of Users	(Maximum) sparsity (taps) for each user
1	150
2	150
3	91
4	69
5	52
6	43

In extensive simulation we simulated symbol error rates (SERs) with the algorithm CoSaMP over different values of control versus data signaling power. The main question which we want to explore is whether or whether not the existing sparse signal processing algorithms such as CoSaMP are strong enough to enable sufficient performance. This cannot be devised from existing analysis. In Figure 3.3.2 we show that sufficient “raw” SERs can be achieved at the expense of higher control signaling power. This is in fact really surprising as the bandwidth is high, i.e. the corresponding vectors dimensions are large.

The main conclusions of this subsection are:

1) The D-PRACH is well suited to incorporate large number of MTC devices in one subframe, so far only limited by the processing power of the base station.
2) The overall performance depends crucially on D-PRACH control signal power vs. D-PRACH payload signal power as well as the overall design of the control signals. At this stage we have only shown a proof of concept and further steps to improve detection of messages must be taken. The results will be published in [WJW13]

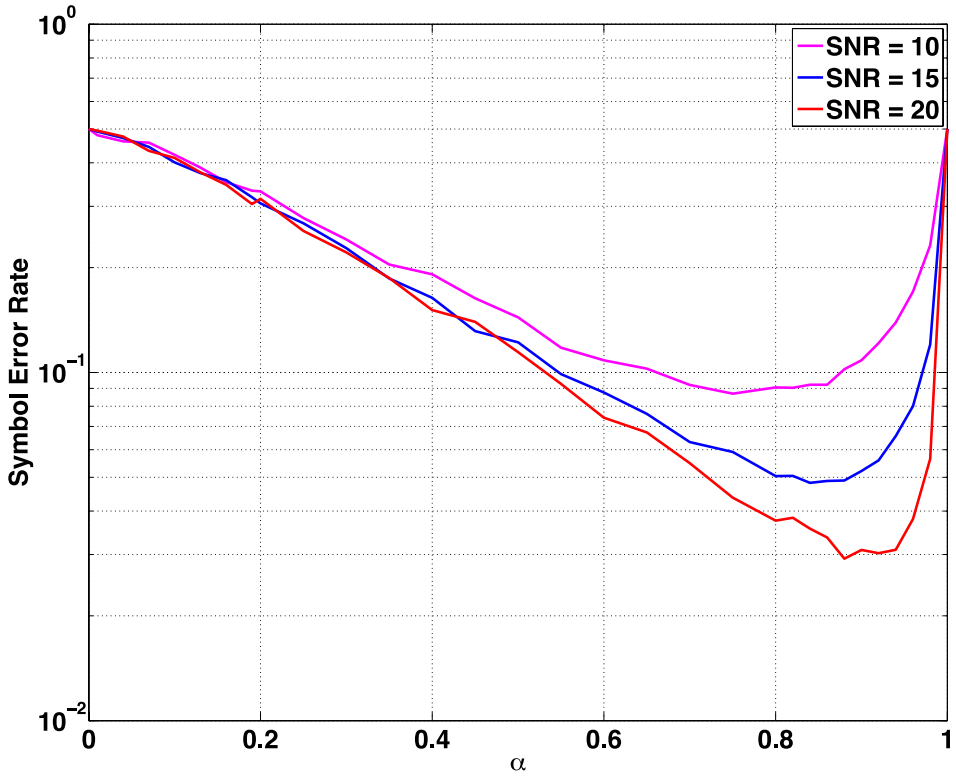

Figure 3.3.2: Simulation of symbol error rates of 10 users in 20MHz bandwidth D-PRACH over α which measures relation of control and data signaling effort over different SNR

4 Reference Scenarios

Throughout this chapter, the 3 main reference scenarios of 5GNOW are introduced: CoMP, MTC and fragmented spectrum. Candidate waveform settings are presented together with simulation results.

4.1 CoMP and Heterogeneous Networks

4.1.1 Uplink

The reference scenario for UL CoMP is illustrated in Figure 4.1.1.

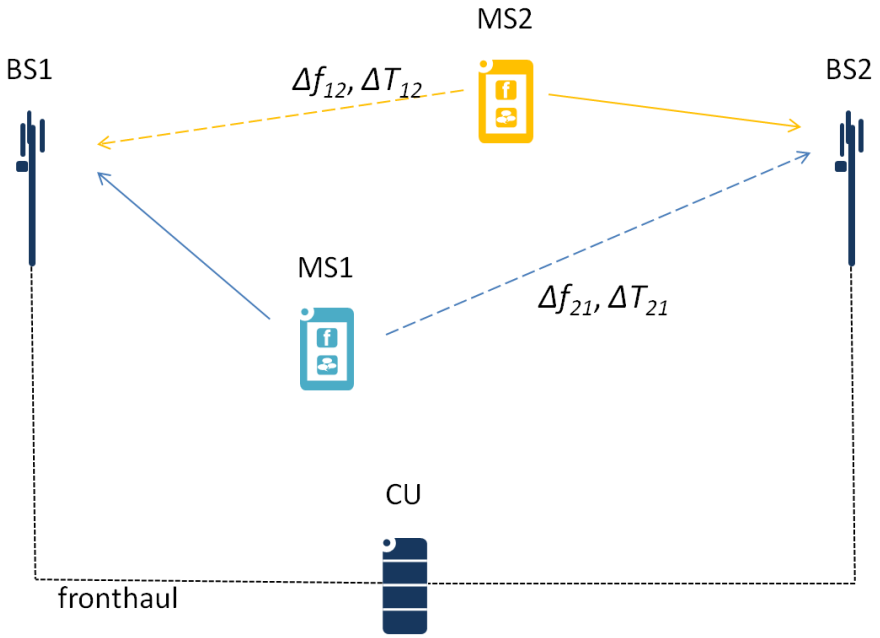

Figure 4.1.1: Reference scenario UL CoMP

Two mobiles MS1 and MS2 are transmitting data using the same time-frequency resources. Two close by base stations BS1 and BS2 are receiving these transmissions forwarding them to a common central unit (CU). The CU applies joint reception to detect the data streams.

BS1 is the serving base station for MS1 (primary base station), while BS2 is the secondary base station for MS1. For MS2 the relations are accordingly (BS2 primary, BS1 secondary). The scenario assumes a LTE-like ranging procedure. So, MS1 is aligned (timing and carrier frequency) to BS1 while MS2 is aligned to BS2. Though different base stations within a given single-frequency network (SFN) are synchronized with respect to their carrier frequency, there still may occur fractional carrier frequency differences. (MS1 and MS2 synchronize themselves to the downlink signals of their respective serving base station, then they do uplink transmission based on this time-frequency synchronization outcome. In this whole chain, any phase jitter, oscillator inaccuracy, etc. will lead to carrier frequency offsets between the signals of MS1 and MS2 received at one of the BS.)
So, as a given mobile only may be aligned to a single base station (its serving basestation), the respective transmission to the secondary base station suffers from a carrier frequency offset (CFO, Δf_{12} and Δf_{21}). Similarly, the transmission to the secondary base station suffers from time delay (ΔT_{12} and ΔT_{21}) as the propagation delays (MS1 to BS1 and MS1 to BS2, MS2 accordingly) are typically

different. Both CFO and time delay are introducing inter-carrier interference degrading the performance.
The detailed mathematical system model and the used joint reception scheme are described in appendix C.1 and are treated in a similar manner in [VWS+13]

The transmissions between *BSi (i* = [1, 2]) and the CU via fronthaul is assumed to be ideal (error free and with sufficient resolution, so that any quantization effects are negligible; e.g. using a CPRI interface).

Ultimate target of this reference scenario is to compare the capabilities of different waveforms to harvest on the gains UL CoMP is promising under realistic synchronization assumptions.
Simulations have been carried out in order to assess the performance gains of UFMC over OFDM. For now, the considered timing offsets are still $\Delta T_{12} = \Delta T_{21}=0$, so, only the impact of frequency offsets on the cross-links are considered, yet. The simulation settings are depicted in Table 4.1.1. The receiver is assumed to have perfect channel state information.

Table 4.1.1: UFMC UL joint reception simulation settings.

Simulation Parameter	Value
Subcarriers per PRB	12
FFT size	128
No. of used PRBs	6
Subcarrier modulation	QPSK
UFMC filter length / cyclic prefix length	16
Frequency Offset	0.1 in subcarrier spacings
Propagation Channel	Block-fading, frequency selective, 16-tap multi-path
Antenna configuration	1 antenna per MS and BS

The simulation results are depicted in Figure 4.1.2.

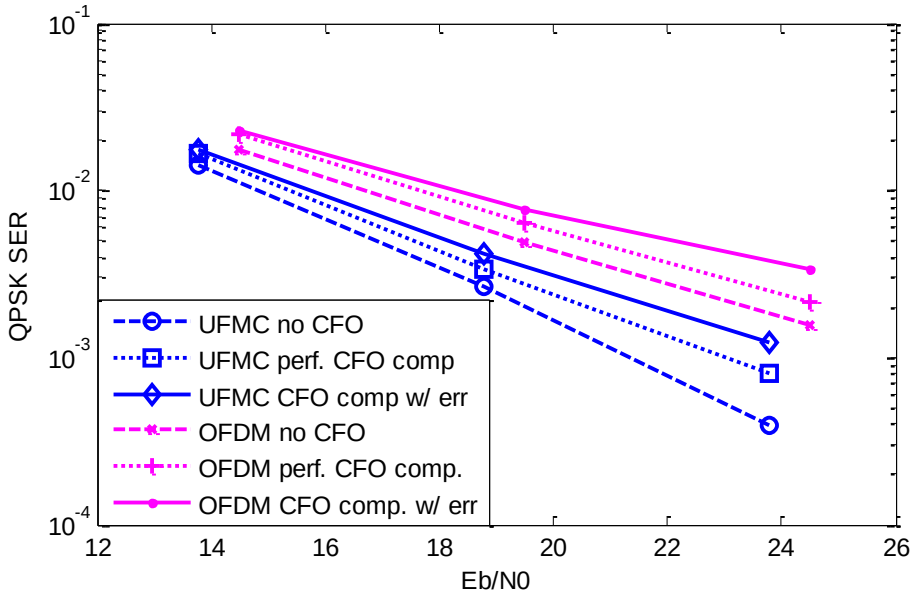

Figure 4.1.2: SER vs Eb/N0 – comparison between UFMC and OFDM for absence of carrier frequency offset (no CFO), perfectly known and compensated carrier frequency (per. CFO comp) and a CFO compensation with a residual mismatch of 10% of the total CFO.

Depending on the SNR operation point, performance gains of several dBs for UFMC over OFDM can be observed, because of better inter-carrier interference suppression by the reduced side-lobe levels of the waveform. This demonstrates that UFMC is a powerful candidate 5G waveform in the CoMP scenario in case of synchronization mismatch. This allows that synchronization requirements can be relaxed and in the case of MTC devices transmitting in CoMP joint reception systems, a better support of low-end devices with relaxed oscillator requirements can be provided by the help of UFMC.

4.1.2 Downlink

In this section, the opportunity to use FBMC for Multi-User (MU) DL cooperation between cells (CoMP) is discussed. MU CoMP enables to provide good quality of service (QoS) to cell edge users while maintaining a high spectral efficiency in the system. Multi-User transmissions exploit the spatial dimension to separate the users (transmission is done for all users in the same band in the same time slots) while cooperation aims at increasing the SINR of UEs far from their serving BS. Figure 4.1.1 (left hand side) shows an example of scenario for MU CoMP transmission. Figure 4.1.1 (right hand side) represents a transmission with the same spectral efficiency, without MU CoMP. All the transmissions are realized on the same time-frequency resource. The black dashed arrows represent the BS array broadsides.

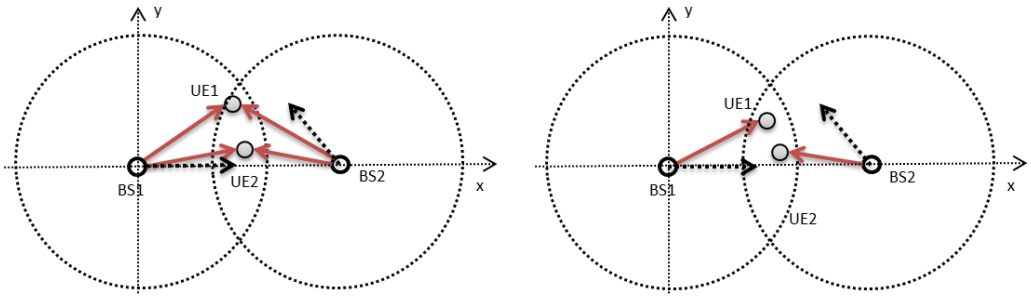

Figure 4.1.1. (left) Multi-User Coordinated MultiPoint transmission (right) Single-User Point to Point transmission

There are many challenges for such a cooperative transmission scheme. First, when BSs are transmitting to a UE, the different distances between the UE and the cooperating BSs create time de-synchronization at the UE that cannot be compensated by a GI. Independent quartz at the BSs and receiver clocks also generate frequency de-synchronization (Carrier Frequency Offset). Furthermore, MU transmission requires reliable spatial filtering at the BSs, so that the interference at the receivers remains low. Filters are computed based on feedback of channel state information from the UEs to the BSs, keeping in mind that the bandwidth occupied by this control information must be kept as low as possible.

Several operations are to be realized to get to MU CoMP on Figure 4.1.1. Each UE must first be synchronized in frequency and in time with both BSs. When UEs are synchronized, they are able to estimate their channel and feedback the necessary information for BSs to decide the MU transmissions parameters.

In Section 4.1 time and frequency synchronization issues for one given UE are studied in order to highlight the benefits of FBMC with respect to OFDM waveform. First steps of the study related to the Multi-User transmission are detailed in the annex of the deliverable (see Appendix section C.1.2).

4.1.2.1 System model for cooperation

Figure 4.1.2 presents the system model for cooperation between cells. The BSs are 500 m apart. The UE is supposed to move on the axis y=0 (Figure 4.1.1) and the antennas at the BSs are considered omnidirectional, without loss of generality. The distance from BS1 is d. The UE is equipped with two receive antennas and performs Maximum Ratio Combining. Each BS is equipped with one transmit antenna. The whole system then forms a virtual 2x2 MIMO transmitter-receiver. The two BSs transmit in the same Resource Blocks (RB). Signal from BS2 is received at the UE with a delay τ regarding to the signal from BS1. This delay reflects the difference of over the air transmission times from both BSs. BS1 and BS2 are considered synchronized in frequency but not in phase. The CFO between the BSs and the UE is $\delta_{\Delta f}$ (expressed in percentage of the carrier spacing) and the initial phases are noted φ_1 and φ_2.

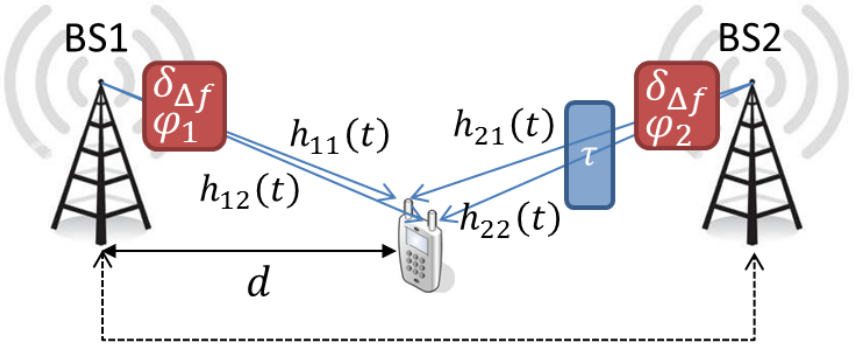

Figure 4.1.2. 2x2 cooperation scenario

The parameters used for the study are given in Table 4.1.1. Those parameters correspond to the LTE standard with 10 MHz bandwidth.

Table 4.1.1. Parameters of the system in DL with FBMC

Parameter	Value	Unit	Abbreviation
Useful bandwidth	10	MHz	
Number of carriers	1024		N_C
Number of active carriers	601		N_{ac}
Carrier spacing	15	kHz	Δ_f
Sampling rate	15.36	MHz	f_S
Sampling period	65.10	Ns	$T_S = 1/f_S$
Number of preamble symbols in the frame	To be defined		
Number of data symbols in the frame	16		
Frame duration	≈ 1.6	Ms	
Overlapping factor	4		K
Delay	< 14.5 (230)	μs (samples)	τ
CFO (Carrier Frequency Offset)	Any	% of Δ_f	$\delta_{\Delta f}$

4.1.2.2 Channel modelling

Each $h_{ij}(t)$ channel, Figure 4.1.2, is completely characterized by a single parameter γ_{RMS}, the Root Mean Square (RMS) delay spread. The shape of the path delay profile for this model is given by Eq. (4.1.1), with γ the delay of the path.

$$P[\gamma] = \frac{1}{\gamma_{RMS}} e^{-\frac{\gamma}{\gamma_{RMS}}} e^{j\zeta[\gamma]} \quad (4.1.1)$$

The phase $\zeta[\gamma]$ of each path is randomly drawn between 0 and 2π.
The RMS delay spread is given by Eq. (4.1.2), where A is the amplitude of the smallest "noticeable" amplitude given in dB relative to the amplitude of the 0th delay path and γ_{max} is the maximum excess delay.

$$\gamma_{RMS} = \gamma_{\max} 10\log 10(e)/A \quad (4.1.2)$$

In the following, for each $h_{ij}(t)$ channel realization the parameter γ_{max} will be randomly drawn between $0.2\ \mu s$ and $3\ \mu s$. Those are typical values for open areas to urban areas [LIN]. Nevertheless γ_{max} is chosen to be the same for the two channels from one BS to the UE. A is set to 20 dB.
The equivalent channel from both BSs to the receive antenna j is defined by Eq. (4.1.3):

$$h_{eq,j}(t) = h_{1j}(t) + h_{2j}(t-\tau) \quad (4.1.3)$$

4.1.2.3 Frequency synchronization

Effect of the Carrier Frequency Offset

The effect of the Carrier Frequency Offset (CFO) on received time sample n ($n = 0,1,\dots,KN_C - 1$) of FBMC symbol m ($m \geq 0$) between BS i and the UE is a phase rotation $e^{j\pi\delta_{\Delta f}m}e^{j\varphi_i}c[n]$, with:

$$c[n] = exp\left(j2\pi\delta_{\Delta f}n/N_c\right) \quad (4.1.4)$$

In the frequency domain, the received signal convolves with the CFO. Eq. (4.1.5) then shows the received symbol $\mathbf{R}_m$ from both BSs affected by the CFO, with $\mathbf{R}_m^i$ given by Eq. (2.3.5):

$$\begin{aligned}\mathbf{R}_m &= \mathbf{R}_m^1\left(e^{j\pi\delta_{\Delta f}m}\mathbf{C}\,e^{j\varphi_1}\right) + \mathbf{R}_m^2\left(e^{j\pi\delta_{\Delta f}m}\mathbf{C}\,e^{j\varphi_2}\right)\\ &= e^{j\pi\delta_{\Delta f}m}\mathbf{X}_m\left(\mathbf{H}_m^1 e^{j\varphi_1} + \mathbf{H}_m^2\mathbf{D}_\tau e^{j\varphi_2}\right)\mathbf{C} + \mathbf{Z}'_m\\ &= e^{j\pi\delta_{\Delta f}m}\mathbf{X}_m\mathbf{H}_m\mathbf{C} + \mathbf{Z}'_m\end{aligned} \quad (4.1.5)$$

With $\mathbf{D}_\tau \in \mathbb{C}^{KN_c\times KN_c}$ a diagonal matrix such that $D_\tau(i,i) = e^{-2j\pi\tau i}$.
$\mathbf{H}_m\left(= \mathbf{H}_m^1 e^{j\varphi_1} + \mathbf{H}_m^2\mathbf{D}_\tau e^{j\varphi_2}\right) \in \mathbb{C}^{KN_c\times KN_c}$ is a diagonal matrix and $\mathbf{C} \in \mathbb{C}^{KN_c\times KN_c}$ is the CFO matrix, given by Eq. (4.1.6). $N = KN_c$.

$$\mathbf{C} = \begin{bmatrix} C[0] & C[-1] & \cdots & C[-(N-1)] \\ C[1] & C[0] & & C[-(N-1)+1] \\ \vdots & \vdots & \ddots & \vdots \\ C[N-1] & C[N-2] & \cdots & C[0] \end{bmatrix} \quad (4.1.6)$$

Coefficients $C[r]$, see Eq. (4.1.7), are computed thanks to the FFT of the coefficients $c[n]$, for $-(N-1) \leq r \leq N-1$.

$$\begin{aligned}C[r] &= \frac{1}{N}\sum_{n=0}^{N-1} c[n] e^{-j\frac{2\pi}{N}rn}\\ &= e^{j\pi\left(\frac{N-1}{N}\right)\left(K\delta_{\Delta f}-r\right)}\,\mathrm{sinc}\left(K\delta_{\Delta f}-r\right)/\mathrm{sinc}\left(\left(K\delta_{\Delta f}-r\right)/N\right)\end{aligned} \quad (4.1.7)$$

A Carrier Frequency Offset $\delta_{\Delta f} \neq 0$ thus causes:

- Inter Carrier Interference, due to $C[r], r \neq 0$ (see Figure 4.1.3)
- Signal power loss, due to $|C[0]| < 1$.

$\mathbf{C}$ is a Toeplitz matrix that can be easily computed thanks to FFTs and IFFTs. It is worth noticing that $\mathbf{C}^H = \mathbf{C}^{-1}$: $\mathbf{C}$ can be written $\mathbf{C} = \mathbf{F}\mathbf{c}\mathbf{F}^H$ with $\mathbf{F}$ the Fourier matrix $F[k,l] = exp(-j2\pi kl/N)$, and $\mathbf{c}$ the diagonal matrix composed of the N coefficients $c[n], n = 0, \dots, N-1$. Then $\mathbf{C}^{-1} = (\mathbf{F}\mathbf{c}\mathbf{F}^H)^{-1} = \mathbf{F}\boldsymbol{c}^{-1}\mathbf{F}^H$. Finally, because $1/c[n] = c^H[n]$, $\boldsymbol{c}^{-1} = \boldsymbol{c}^H$ and $\mathbf{C}^{-1} = \mathbf{C}^H$.

Figure 4.1.3 shows $|C[r]|$ for $K = 4$. Few carriers actually interfer on carrier 0; beyond five carriers on each side the interference becomes negligible. For $\delta_{\Delta f} > 12{,}5\ \% = 1/(2K)$, $C[0]$ is no longer the dominant term, most of the energy is concentrated on the carriers next to the carriers of interest. From this observation, in the following the notation of Eq. (4.1.8) will be used, with $q \in \mathbb{N}$ the 'entire part' of the CFO and $y \in \mathbb{R}, |y| < 1/(2K)$ the 'fractional part' of the CFO:

$$\delta_{\Delta f} = q/K + y \tag{4.1.8}$$

Coefficients $c'[n]$ and $C'[n]$, used in the following for the correction of the CFO, are defined as in Eq. (4.1.9):

$$c'[n] = exp(j2\pi yn/N_c) \tag{4.1.9}$$
$$C'[r] = e^{\frac{j\pi(N-1)(Ky-r)}{N}} sinc(Ky-r)/sinc\big((Ky-r)/N\big)$$

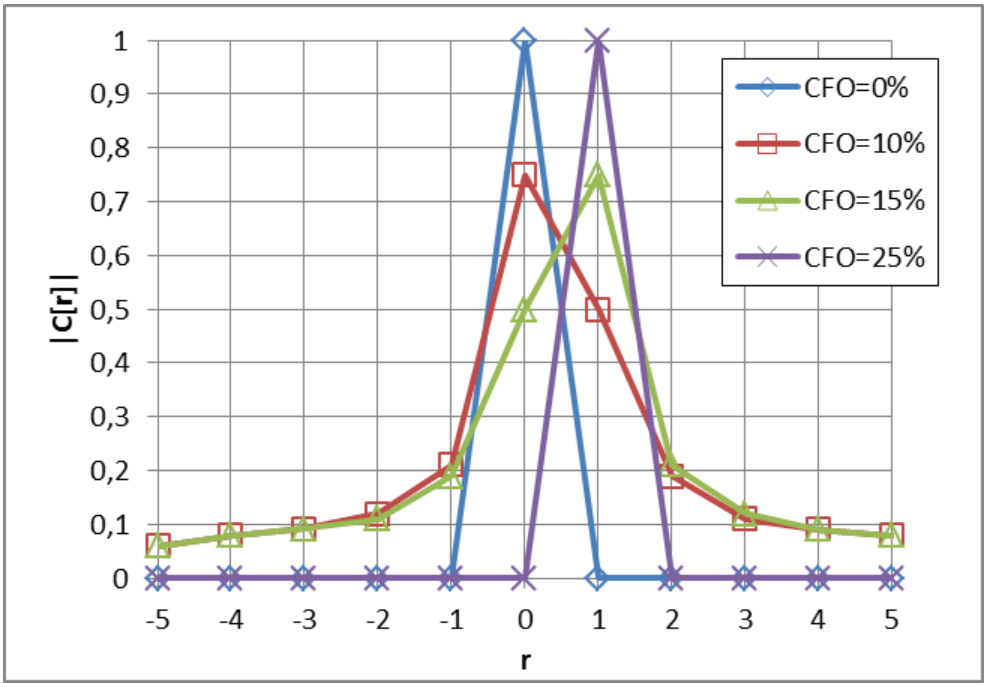

Figure 4.1.3. Inter carrier interference due to CFO

In [MKS03] the impact of the CFO on the BER of OFDM systems was computed. The black curve with squares on Figure 4.1.4 shows the results in an AWGN channel, with an uncoded QPSK modulation and a frame length of 0.1 ms (CP of 20 µs), at Eb/N0 = 10 dB. CFOs higher than 0.05 % of the subcarrier spacing cannot be tolerated without compensation. On Figure 4.1.4 the impact of the CFO on the performance of an FBMC transmitter-receiver is also illustrated. Here the frame is composed of 4 symbols for the preamble and {8,16} symbols of data, for a total duration of {1.1,1.6} ms, thus

longer than in the simulation in [MKS03] (a longer frame is an unfavorable case when CFO is present). The BER is measured in an AWGN channel, for a point to point QPSK 3/4 transmission, at SNR = {3.28,4.17} dB. The other parameters are those of Table 4.1.1.

First, as expected, when looking at FBMC simulation results, the CFO most impacts longer frames: the BER increases more quickly with the CFO for the 1.6 ms frame compared to the 1.1 ms frame case. Then it must be noticed that FBMC is more robust to CFO than OFDM, even for long frames.

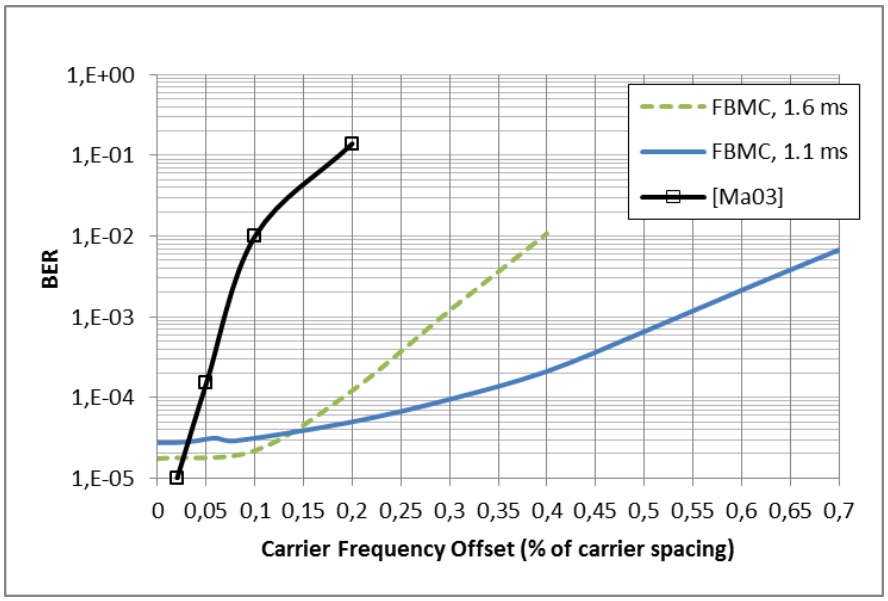

Figure 4.1.4. Impact of the CFO on the BER, with no correction

Estimation of the CFO

The scheme proposed for the estimation of CFO relies on a preamble transmitted by the cooperating BSs. This preamble is composed of M FBMC symbols in which BS1 and BS2 transmit pilots on the same carriers. Based on Eq. (4.1.5), with the omission of the noise, and with $\mathbf{R}_m$ and $\mathbf{R}_{m+p}, p+m<M$, two received symbols of the preamble, the product of these two terms can be written as:

$$\begin{aligned}\mathbf{R}_m\mathbf{R}_{m+p}^H &= \left(e^{j\pi\delta_{\Delta f}m}\mathbf{X}_m\mathbf{H}_m\mathbf{C}\right)\left(e^{j\pi\delta_{\Delta f}(m+p)}\mathbf{X}_{m+p}\mathbf{H}_{m+p}\mathbf{C}\right)^H \\ &= e^{-jp\pi\delta_{\Delta f}}\mathbf{X}_m\mathbf{H}_m\mathbf{C}\mathbf{C}^H\mathbf{H}_{m+p}^H\mathbf{X}_{m+p}^H\end{aligned} \quad (4.1.10)$$

Remembering that $\mathbf{C}^H=\mathbf{C}^{-1}$ and $\mathbf{H}_m$ being a diagonal matrix, and with the two following assumptions:

- The channel is constant during the reception of the preamble: $H_m[f]=H_{m+p}[f]$,
- Carrier frequencies of FBMC symbols m and $m+p$ of the preamble carry the same information: $X_m[f]=X_{m+p}[f]$,

an estimation of the CFO is then given by the phase of the product $\mathbf{R}_m\mathbf{R}_{m+p}^H$ divided by $-p\pi$. Nevertheless this product requires lots of operations. To decrease the computational complexity the product could be done on any subset of carriers, consecutive or not, of the N pilot carriers of symbols $\mathbf{R}_m$ and $\mathbf{R}_{m+p}$.

This method allows an accurate estimation of CFOs such that $|\delta_{\Delta f}| < 1/(2K)$. Indeed, as shown by Eq. (4.1.7), for $|\delta_{\Delta f}| > 1/(2K)$ $\exists\, r \neq 0$ such that $|C[r]| > |C[0]|$ and the highest part of the energy at the receiver is no longer on the pilot carriers but on neighboring carriers (see also Figure 4.1.3). The first step in the estimation of the CFO is then to scan the frequencies next to the pilot frequencies to find the carriers with the highest energy. This operation returns the value $\tilde{q}$, with the superscript $\tilde{.}$ standing for the estimation. The second step is the estimation of y on carriers $\tilde{q}$ carriers apart from the pilot carriers thanks to Eq. (4.1.10).

To put it in a nutshell, it was established in this section that FBMC is more resistant to frequency de-synchronization than OFDM, due to the very good frequency localization of FBMC carriers. Frequency synchronization (estimation and compensation of the CFO) with FBMC can be entirely realized at the UE in the frequency domain. The most part of the CFO can be easily and accurately estimated thanks to a simple energy detection algorithm on the preamble carriers. The residual part of the CFO after this first coarse estimation is lower than 100/(2K)% (12.5 % with K=4) of carrier spacing. The same method applied to OFDM would lead to a much higher residual CFO of 50 % at maximum and thus worst performance in terms of BER would be obtained. Furthermore, the algorithm proposed to estimate the residual part exhibits reduced complexity while achieving good performance.

4.1.2.4 Time synchronization

Cooperative MIMO-OFDM deals with Inter Symbol Interference (ISI) thanks to the use of a CP: when delay difference between the cooperative BSs is shorter than the CP, all ISI that may deteriorate the quality of service at the receiver is suppressed. For cooperative MIMO-OFDM, due to high propagation distances, the CP must be longer than for non-cooperative OFDM. In LTE 10 MHz the short CP is 72 samples long and the long CP has the duration of 256 samples. Contrary to OFDM symbols, FBMC symbols structurally overlap in the time domain at the transmitter, the use of a CP thus becomes useless. Figure 4.1.5 shows the influence of the delay on the BER at the UE for the scheme of Figure 4.1.2, for 16QAM modulation with convolutional code of rate 3/4. The distance d is 250 m. The CFO is null and neither estimated nor corrected. At the UE, on each antenna j the equivalent channel $h_{eq,j}(t) = h_{1j}(t) + h_{2j}(t-\tau)$ is either supposed perfectly known (dotted line curve) or estimated (solid line curve). The estimation is realized thanks to preamble symbols with one carrier over four being a pilot carrier.

It first must be noted that with perfect channel estimation, performance does not decrease even for very high delays. It is then shown that FBMC, with real channel estimation, can cope with delays up to 120 times samples (7.8 µs) without any estimation or correction with the proposed pilot scheme. For the parameters of LTE with 10 MHz channel bandwidth, this corresponds to a distance of 2340 m. FBMC modulation is thus demonstrated to be very resistant to time propagation differences between signals from the two BSs, due to its overlapping structure. To the contrary of OFDM [IM08], FBMC does not need any Cyclic Prefix to cope with time propagation differences; FBMC spectral efficiency is then preserved without impact on time synchronization.

The causes of the deterioration of the BER for real channel estimation with high delays are the phase rotations due to the delay τ that increase the frequency selectivity of the equivalent channel $h_{eq,j}(t)$ (see Eq. (4.1.3)).

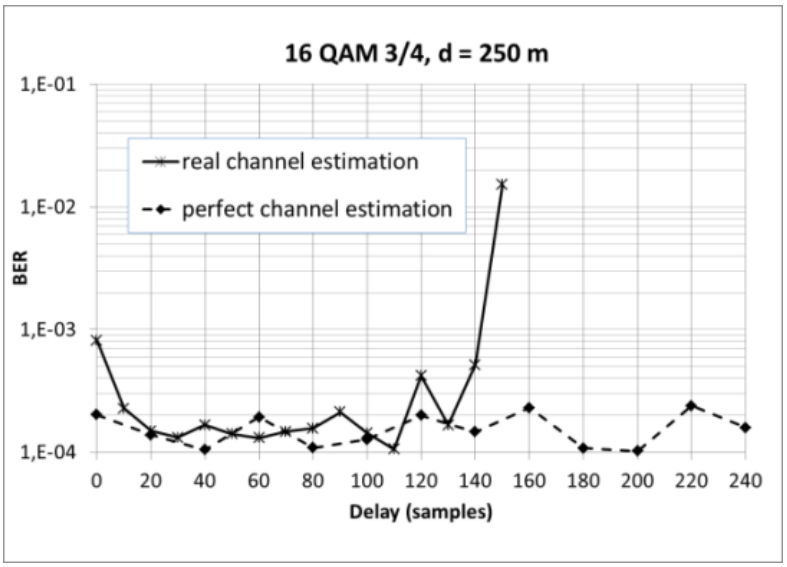

Figure 4.1.5. BER of CoMP FBMC with MRC at the receiver for different delays τ between BSs.

Indeed when the coherence bandwidth of the channel is much smaller than the pilot spacing, channel interpolation cannot be reliably computed. In order to decrease the effects of phase rotations of the channel due to high delays, an algorithm will be studied in the near future to estimate the delay. The objective is to design an algorithm that will be very robust to non-detection and false alarm and that will require very limited feedback information.

4.2 MTC and Tactile Internet

Wireless communications has enabled a variety of applications and services from 2G to 4G. Current trends point that with 5G on the horizon, the Internet of Things (IoT) will be one of the next big things. While IoT itself is a very exhaustive field that covers many topics and research areas, the scenario of interest within this section focuses on the machine-type communication (MTC) aspect and envisions a 'Tactile Internet' scenario as a new service and technology enabling ingredient. This is an application that imposes strict requirements to latency and resilience of the transmission of short and asynchronous bursts of data [Fet12]. The scenario features low-effort synchronization, in order to keep affordable complexity on the MTC terminals, the production cost low and the settling time required for waking a device from sleep mode minimal. Thus, instead of oscillator accuracy requirements of 0.1 ppm in the current 4G standard, this means that the 5G transmission scheme needs to be able to handle significant frequency offsets, orders of magnitude higher. In the past, the use of Generalized Frequency Division Multiplexing (GFDM) has been already proposed for MTC [FKB09].

A following set of parameters for GFDM is initially proposed to address these specific requirements. For an MTC uplink in a cellular network, the overall goal is to transmit data bursts of up to 1000 bits within 100 µs, resulting in a data rate of 10 Mbit/s and ultimately aims to enable end-to-end delays within a few milliseconds in a local network. Assuming cell radii with no more than 1km, delay spread in the order of 4µs duration is expected (1µs delay corresponds to 300m of multipath deviation). This value is used in Table 4.2.1 to define guard interval and, as an initial approach, also the symbol

duration is chosen to be equal the guard interval, resulting in a subcarrier spacing of 250 kHz (matching the coherence bandwidth of the channel). The model initially considers high order QAM (64QAM) and high SNR (i.e. 25dB). The number of subcarriers K and the number of symbols per subcarrier M are chosen initially to be 10 and 16, resulting in a total of transmitted bits to be 10 * 16 * 6 = 960 bits per GFDM block.

Table 4.2.1: GFDM parameters

Parameter	**Value**
GFDM CP-length/ Symbol duration (Ts)	4µs (1 symbol of the subcarrier)
Subcarrier spacing (Δf)	240kHz (1/4µs)
Modulation	64QAM
K (No. of used Subcarriers)	10
M (No. of used Symbols per Subcarrier)	16
Block duration	4µs * 16 + 4µs = 68us
Receiver	MF, ZF or MMSE
Channel	AWGN / Veh A block fading
Freq. offset (*)	[0 … 0.1Δf]
Timing offset	[0 … 0.1Ts]

The proposed multicarrier approach has the advantage of flexible allocation in non-continuous bandwidth portions. Alternatively lower PAPR results can be obtained by employing minimal number of subcarriers, by choosing just one with larger number of symbols GFDM turns into an extreme case where GFDM concept address a SC-FDE case.

Table 4.2.2: GFDM parameters

Parameter	**Value**
GFDM CP-length/ Symbol duration (Ts)	4µs (10 symbol of the subcarrier)
Subcarrier spacing (Δf)	2.4MkHz (1/0.4µs)
Modulation	64QAM
K (No. of used Subcarrier)	1
M (No. of used Symbols per Subcarrier)	160
Block duration	0.4µs * 160 + 4µs = 68us
Receiver	MF, ZF or MMSE
Channel	AWGN / Veh A block fading
Freq. offset (*)	[0 … 0.1Δf]
Timing offset	[0 … 0.1Ts]

Further result details are presented in the appendix C.2. The bit error ratio (BER) performance and the out of band radiation of GFDM are studied in C.2.1 for an intermediate set of parameters showing that theoretical results can still be obtained with its non-orthogonal approach due a more localized spectrum. A hypothetical opportunistic use of spectrum is illustrated in C.2.2 showing the benefits of the waveform over traditional OFDM. In C.2.3 the issue of complexity is presented and with frequency domain processing the scheme can be implemented with reasonable resources. Last in C.2.4 the PAPR aspects are addressed and by allocating just one subcarrier GFDM can keep it at low levels, constituting an interesting configuration for the uplink.

4.3 Fragmented Spectrum

Due to the asynchronous and dynamic use of the available spectrum, user equipment may need to transmit in a set of smaller and smaller time / frequency slots. When the system is first initialized, the spectrum may contain a large amount of contiguous resource blocks (RB). However when non-synchronous services are stopped, new region of RBs are created. When a new service appears, it may be impossible to resume the allocation exactly where the service has ended as another service may already have been allocated in that resource block. A new portion of RB has to be used. As time goes on, large RB becomes less available and with the reappearance of services the spectrum tends to split up even further. Only smaller regions of RB become available to the radio resource management entity at any given instant. This means that the resource management entity is no longer able to free-up contiguous resource blocks but instead has to break them into fragments. This is especially the case of heavy network traffic load— longer contiguous regions of RB are less likely to be available. This will lead to a highly fragmented spectrum.

As described in [D2.1], the asynchronism feature of the waveform is a key technical challenge. For example, devices should not be forced to be integrated into the bulky synchronization procedure which has been deliberately designed to meet orthogonal constraints. Instead, they optimally should be able to awake only occasionally and transmit their message right away without being strictly synchronized (coarse synchronization). By doing so traffic may be removed from standard uplink data pipes and signalling overhead should be reduced.

The base station monitors the time when the transmission arrives and sends an instruction to the mobile station via the downlink channel to inform the mobile station the time of advance transmission. In other words, in the case of UL transmission, all the users should be synchronized. Every signal arrival time should be placed in the guard interval as illustrated in Figure 4.3.1 in order to simultaneously demodulate multiple users while guaranteeing the orthogonality condition. This mechanism requires a constant exchange of control information, introducing an overhead on the network that could be significant for low data rate transmissions in the UL. The design of non-orthogonal and asynchronous waveform is required.

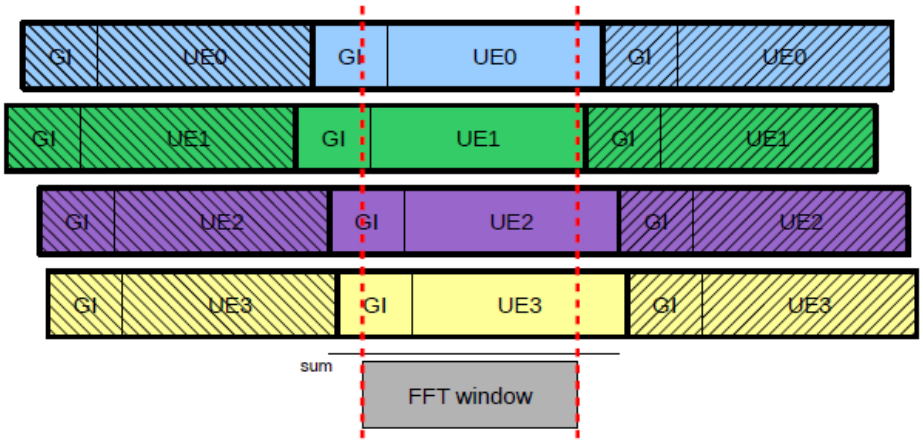

Figure 4.3.1. Example of OFDMA with perfect synchronisation of the users

In the case of non-synchronized users as shown in Figure 4.3.2, the orthogonally condition is not respected. As user 0 is not time aligned, interference in the cell is introduced.

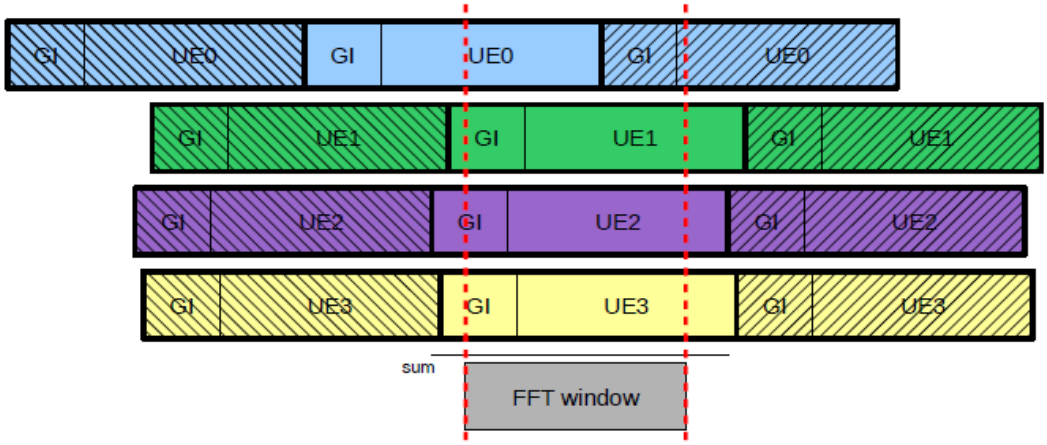

Figure 4.3.2. Example of OFDMA with non synchronized users

In that case, Inter Carrier Interference (ICI) and Inter Symbol Interference (ISI) dramatically deteriorate performance. If the FFT process is applied per user, it is possible to quantify the level of interference introduced by the non-synchronized users. This problem has been extensively investigated in the literature (see [XTY+03] for instance). The most common scheme consists in modelling the interference by a normal random process. When the interference is related to a large number of independent signals (the central limit theorem applies), this method is appropriate. However, when the central limit theorem does not apply (low number of carriers), the probability density function of the interference differs from those predicted by the Gaussian model.

In [MTR+11] the authors proposed an accurate model based on interference tables taking into account timing offset. Figure 4.3.3 illustrates the interference table for OFDM waveform with a guard interval of T/8, where T stands for the OFDM symbol duration. We clearly see that the interference is spread over a high number of sub carriers with a high level of magnitude. It is worth mentioning that a subcarrier gap of more than six carriers is required to limit the interference level below 3.10^{-3} (-25dB).

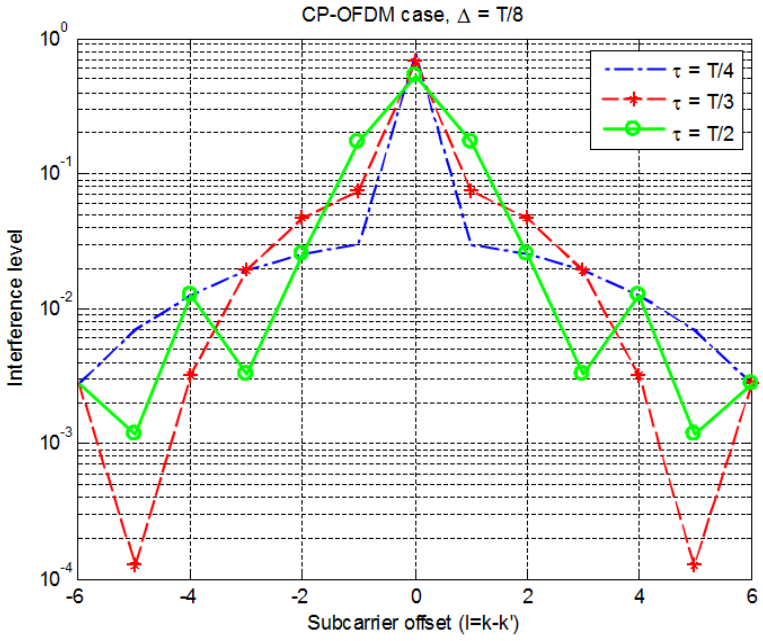

Figure 4.3.3. OFDM instantaneous interference table for various timing offset (from [MTR+11])

Now let's consider the case of FBMC waveform. By considering the metric proposed by [MTR+11], it is possible to compute the instantaneous interference table of FBMC waveform. In the filter bank based system, transmit pulses are well localized in time and in frequency. The orthogonality between sub-carriers is maintained by introducing a half symbol period delay between the in-phase and the quadrature components of each complex symbol. Figure 4.3.4 illustrates the interference table for a FBMC waveform with an overlapping factor of K=4.

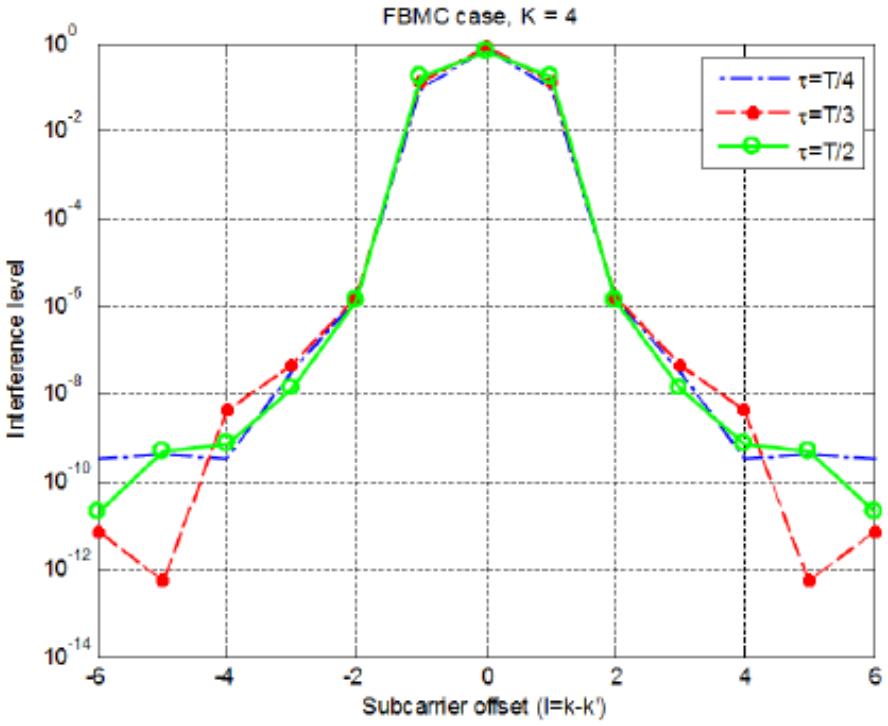

Figure 4.3.4. FBMC instantaneous interference table for various timing offset (from [MTR+11])

We observe that only adjacent sub carriers introduce interference. It can be explained by the better frequency localization of the prototype filter. This fact demonstrates that FBMC waveform may be used in a non-synchronous context and especially in the fragmented scenario. Indeed it is worth mentioning that a subcarrier gap of only two carriers is required to allow non-synchronous transmission with FBMC. The prototype filters are more frequency localized and increase the robustness of the FBMC waveform against asynchronous transmissions.

The impact of the interference on the Bit Error Rate (BER) may also be evaluated. The impact of the guard band of a FBMC (K=4) and an OFDM (using a Guard Interval of 1/8) system on AWGN channel has been simulated and performance are given in Figure 4.3.5. The BER is estimated over various timing offset values by means of a random variable. A non-synchronous signal is generated on adjacent carriers with a guard band of δ sub carriers. Perfect synchronization by the receiver on the desired signal has been assumed. FBMC waveform exhibits good performance and provides for δ=1 the same level of performance as the perfectly synchronized case. For the case of OFDM an error floor appears even for large guard band of size δ=20. Indeed, the interference term slowly decreases with the carrier index as illustrated in Figure 4.3.3.

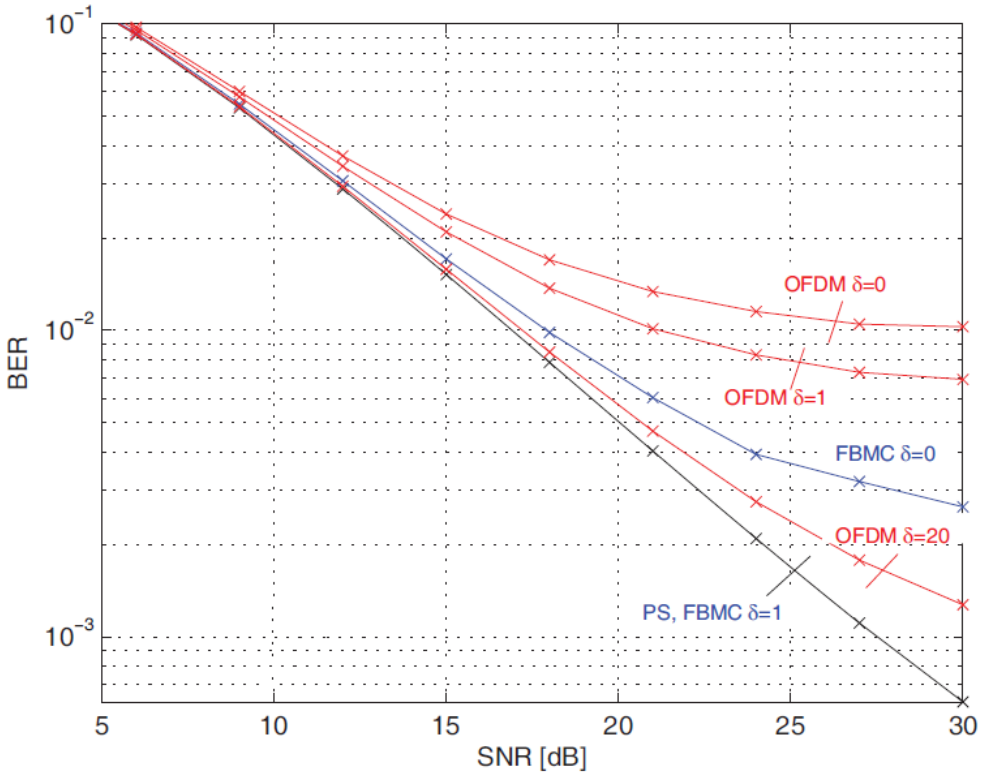

Figure 4.3.5. BER performance for different frequency guard band sizes assuming non synchronized interferer

Based on these results it should be interesting to quantify the gain offered by FBMC waveform on a LTE fragmented based scenario. We considered the following LTE parameters given in Table 4.3.1.

Table 4.3.1. Considered LTE parameters for performance comparison

Channel Bandwidth (MHz)	**1.4**	**3**	**5**	**10**	**15**	**20**
Transmission Bandwidth (MHz)	1.08	2.7	4.5	9	13.5	18
Subcarrier Spacing	15 kHz					
Sampling Frequency	1.92	3.84	7.68	15.36	23.04	30.72
FFT Size	128	256	512	1024	1536	2048
Active Carriers	73	181	301	601	901	1201

We assume traffic-type services using the 1.4MHz configuration. It could be for instance MTC service. We proposed to compute the number of services that may be aggregated into the channel bandwidth according to the scheme described in Figure 4.3.6.

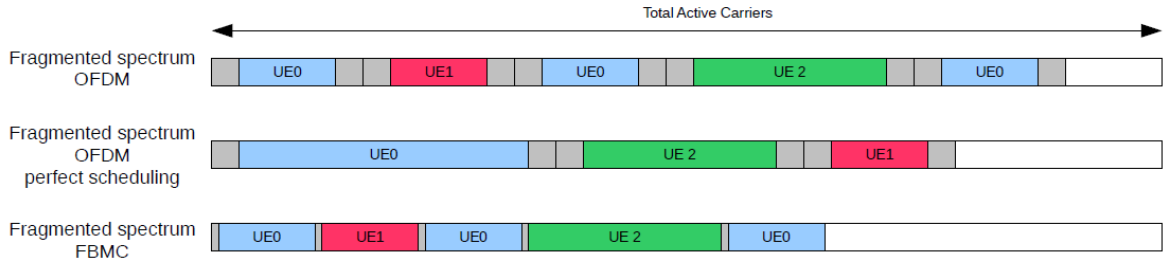

Figure 4.3.6. Example of fragmented spectrum for OFDM and FBMC waveform

The following table illustrates the gain achieved when using FBMC considering δ=2 and when using OFDM considering δ=20:

Table 4.3.2. FBMC vs. OFDM spectral efficiency comparison using LTE parameters

Channel Bandwidth (MHz)	1.4	3	5	10	15	20
Active Carriers	73	181	301	601	901	1201
Number of MTC OFDM case	1	$\left\lfloor \frac{181}{73+20} \right\rfloor = 1$	3	6	9	12
Number of MTC FBMC case	1	$\left\lfloor \frac{181}{73+2} \right\rfloor = 2$	4	8	12	16
Gain	0	50%	33.33%	33.33%	33.33%	33.33%

Because OFDM waveforms are badly localized in frequency, the spectral efficiency of a fragmented OFDM spectrum is poor. Indeed a large guard band is required to manage the intercell interference. Therefore a complex dynamic resource allocation algorithm must be set up and as a consequence a large signaling overhead is necessary. On the other hand FBMC waveforms only require a small guard band and are therefore more efficient in presence of spectrum fragmentation. A radio resource scheduler is still required but the constraints on scheduling and the cell signaling overhead may be significantly relaxed. A gain of 33.33% may be expected in terms of spectral efficiency if a FBMC waveform (K=4) with δ=2 is considered. It is worth mentioning that the gains are asymptotical since the duration of a FBMC burst may be larger than the OFDM.

Another important issue with respect to fragmented spectrum usage is related to robust channel estimation. Preliminary discussion on this topic is given in the annexe of the document (see appendix, section C.3).

5 Comparison and Discussion of Candidate Waveform Properties

This chapter provides an overview on the candidate waveform properties, showing their potential for the new 5G scenarios and requirements to be well suited and to outperform OFDM. At this stage of the project we have done no efforts to favor one waveform approach over the other as they are applied in very different settings. On the other hand, in their specific settings the selected waveform show very clear advantages over existing standard LTE approach as we have shown in the previous sections. The following tables show a first summary of waveform properties to be used in further (ongoing) discussions in the project.

5.1 Overview of waveform properties

Tables 5.1.1.-5.1.4 summarize the main properties of the waveform candidates in the 5GNOW project.

FBMC

Table 5.1.1: Main properties of FBMC

BER	Similar to CP-OFDM
PAPR	Similar to OFDM (LTE-A)
Out of band radiation	Very well localized spectrum, up to -60dB attenuation at adjacent subcarriers
Throughput	Higher throughput due to cyclic prefix removal
Spectral efficiency	Supports OQAM modulations, high spectral efficiency due to cyclic prefix absence and lower side lobes
Complexity	FFT/IFFT structure, higher complexity than OFDM (polyphase network)
Training structure	Burst modes with preambles allows time-frequency synchronisation and channel estimation
Sensitive to time and frequency offsets	Very robust to time and frequency offsets
Multiuser capability	Block based modulation configurable in time and frequency, adapted to asynchronous users scenario
Multipoint capability	Avoid multiple access interference in uplink, less complex than equivalent CP-OFDM with MAI-cancellation, better than OFDM for given scenario with impairments (e.g. precision of local

	oscillators)
Resource allocation mechanisms/ channel adaptive scheduling	LTE like
Adaptivity potential	Flexible parameters: number of symbols per subcarrier, number of subcarriers,…
Coexistence to legacy systems	Low out of band radiation,
Key open problems	Frame/frameless structure, synchronization, channel estimation (fragmented spectrum) and equalization
Test environments	Single/parallel-user links with AWGN and multipath channels
Implementation/demonstrator of waveforms	CEA-LETI platform (FPGA/ARM-cortex8) and NI RF front-ends
Intrinsic motivation for	Explore the advantages of well-localized spectrum and increase of spectral efficiency. Keep the advantages of LTE in not so synchronous and orthogonal scenario

GFDM

Table 5.1.2: Main properties of GFDM

BER	Can match standard performances [MKLF12], [DMLF12]
PAPR	Covers from single carrier up to Gaussian (OFDM)
Out of band radiation	Lower than OFDM. Pulse shaped subcarriers
Throughput	In synchronous mode it is expected to perform at least as LTE. Combined use of CP and more localized spectrum properties offers opportunities for improvements on efficiency. Flexible short burst asynchronous scenario may imply in some efficiency loss.
Spectral efficiency	Supports MQAM modulations
Complexity	The complexity is as in the FFT/IFFT structure of SC-FDMA with little additional frequency domain process for filtering and linearly increased complexity for interference cancellation in receiver [GMN+13]
Training structure	The multi-symbol structure allows the insertion of training sequence in a per subcarrier base. GFDM fingerprint [DPF12] (self-correlation in time/frequency domain) exhibits potential for

	synchronization.
Sensitive to time and frequency offsets	ICI cancelation structure is inherent to the GFDM receiver. Expected to support for CFOs up to 10%of the subcarrier bandwidth, in contrast to 1% in case of OFDM mode
Multiuser capability	Block based modulation configurable in time and frequency resources.
Multipoint capability	Not yet investigated
Resource allocation mechanisms/ channel adaptive scheduling	LTE like
Adaptivity potential	Flexible parameters (constellation, number of symbols per subcarrier – M=4/8/16/32/64, number of subcarriers – MxK = 8192/4096/2048/1024 -> K=32/…/2048, rolloff)
Coexistence to legacy systems	Low out of band radiation. Turns into OFDM when M=1
Key open problems	Frame/Frameless structure, appropriate scheme for time and frequency synchronization and channel estimation
Test environments	Single/Multiple/Parallel-user links with AWGN and Rayleigh channels; consider also differences/specifics of DL and UL. In DL single TX and non-cooperative RX, in UL non-cooperative TX and single RX. The scenarios give different requirements i.e. on synchronization.
Implementation/Demonstrator of waveforms	National Instruments PXI platform
Intrinsic motivation for	Keep the advantages of LTE in relaxed synchronicity and orthogonality scenario, accepts a huge amount (100x) of low rate subscribers (MTC devices)

UFMC:

Table 5.1.3: Main properties of UFMC

BER	In AWGN slightly better than OFDM (no energy wasted for CP). In asynchronous settings better than OFDM, see chapter 3.1.
PAPR	Similar as with OFDM
Out of band radiation	Reduced through filtering (between PRBs), see Figure 2.2.4.
Throughput	Better than OFDM (smaller guards). In the presence of impairments (e.g. CFO, timing offsets) gains to be expected, see chapter 3.1.
Spectral efficiency	Better than OFDM (smaller guards, better performance in asynchronous settings) , see

	chapter 3.1.
Complexity	Slightly higher than OFDM, due to subband filtering
Training structure	Similar to OFDM
Sensitive to time and frequency offsets	Fractional time delay: as long as offset + delay spread stays within CP length worse than OFDM, than better (smooth decay with BFMC, hard decay with OFDM) CFO: better than OFDM (reduced out-of-band radiation). Impact of asynchrony between different users reduced, see chapter 3.1.
Multiuser capability	Block based modulation configurable in time and frequency, adapted to asynchronous users scenario as with OFDM. Synergy potential with IDMA will be investigated.
Multipoint capability	Better than OFDM for given scenario with impairments – e.g. UL CoMP with CFOs suffers from less ICI than OFDM, due to reduced signal side lobe levels, see chapter 4.1.1.
Resource allocation mechanisms/ Channel adaptive scheduling	As with OFDM
Adaptivity potential	As with any MC-signal with additional adaptivity of filtering function
Coexistence to legacy systems	Better than with OFDM (low out-of-band radiation)
Key open problems	Quantification of UFMC behaviour in asynchronous settings
Test environments	UL CoMP, unified frame structure with relaxed synchronicity for MTC support, fragmented spectrum
Implementation/demonstrator of waveforms	tbd
Intrinsic motivation for	Achieve the merits of filtered multi-carrier (low out-of-band radiation and the subsequent consequences) while avoiding potential traps (long

	filter length, OQAM, significant self-interference)

BFDM

Table 5.1.4: Main properties of BFDM

BER	Similar to OFDM in AWGN, better in time-variant channels
PAPR	No significant difference to others
Out of band radiation	Better than OFDM, worse than e.g. FBMC
Throughput	Higher in time-variant channels
Spectral efficiency	Higher in time-variant channels
Complexity	In the order of FBMC
Training structure	Similar to OFDM in PRACH setting
Sensitive to time and frequency offsets	In the order of FBMC
Multiuser capability	Yes, applied in multiuser PRACH mac
Multipoint capability	tbd
Resource allocation mechanisms/ Channel adaptive scheduling	Possible
Adaptivity potential	tbd
Coexistence to legacy systems	Possible with OFDM
Key open problems	tbd
Test environments	P-RACH setting
Implementation/demonstrator of waveforms	tbd
Intrinsic motivation for	tbd

5.2 Discussion

As we have said no candidate waveform is favored but some general properties might be pointed out already at this stage. This general line of arguments is the reasoning behind why certain waveforms have been selected for specific scenarios. Clearly, the FBMC framework is the by far most developed framework and is well suited for long burst, best effort traffic where up- and down- ramp time is not

so important Moreover, within the project very efficient synchronization schemes have been developed which make the approach now applicable specific for CoMP scenarios where the inherent time and frequency offsets severely degrade the performance. It is clear that FBMC is a strong candidate in this setting. First results have been reported on conference level. Moreover, the maturity is already proven by hardware implementation demonstration at this year's FuNeMS'13 conference.

UFMC is a new technique still to be presented to a broader audience. It is developed in parallel to the unified frame vision which requires a very adaptive waveform able to cope with flexible coding schemes for diverse traffic conditions. It combines properties of filtered OFDM and FBMC underlying its potential and suitability for mixed traffic scenario. On the other hand the technique is still at an early stage and must be further developed.

GFDM is a block oriented transmission alleviating the tail problems of e.g. FBMC. Moreover, the technique is very flexible and suited for standard signal processing (linear receiver, successive interference cancellation etc.). These properties make the technique advantageous for very short burst transmission in general which has been already presented in this year's conferences. On the other hand the high complexity might result in time-consuming signal processing. While these points will be clarified in the course of the project hardware implementation and demonstration is beyond infancy stage already (see deliverable D5.1). BFDM can be seen as a special case of this technique with a suitable pulse-shaping technique and bi-orthogonalization step for receiver processing on top. This is actually well suited for the random access scenario where long symbols can be assumed. In ongoing analysis the proposed spline based approach will be further sustained exploring whether or whether not the specific properties are advantageous.

6 Conclusion

6.1 Summary of D3.1

This deliverable has provided a discussion of candidate waveforms for 5G wireless systems, as well as selection criteria and benchmarking results. New waveform candidates are motivated and driven by the requirements of future 5G systems.
Specific corner cases of the requirements are set up by the different scenarios introduced in chapter 4: coordinated multi-point (CoMP) and heterogeneous networks (HetNet), the Tactile Internet and usage of fragmented spectrum. For all of those key scenarios addressed by 5GNOW, candidate waveforms, which are described in chapter 2, are discussed and results are provided, where performance gains motivate the usage of alternatives to classical OFDM used in current generation systems.
Another strong driver for new physical layer signal formats is the multiple access. 5GNOW provides in chapter 3 a multiple access vision, suitable for the very inhomogeneous traffic type requirements. The concept of the Unified Frame Structure e.g. allows handling synchronous and asynchronous users within the same band. The relaxation of synchronicity (and thus orthogonality) is an appealing feature to get rid of signalling overhead, growing with larger number of devices which 5G systems have to handle due to the Internet of Things (IoT) and Machine Type Communication (MTC). The flexibility of multi-carrier signal formats is very desirable for the Unified Frame Structure, but here classical OFDM would suffer from inter-carrier (ICI) and inter-symbol interference (ISI). So the proposed 5GNOW candidate waveforms from chapter 2, having a much better robustness against ICI and ISI, enable and support the Unified Frame Structure. The usage of multiple signal layers increases the flexibility of the multiple access and is appealing in conjunction with multi-user / multi-cell processing, required in modern systems. So it is as well part of the Unified Frame Structure and discussed in chapter 3. As random access is an important aspect in conjunction with large number of devices (driven by IoT and MTC) it is handled as well in chapter 3.
The four 5GNOW candidate waveform approaches are Generalized Frequency Division Multiplexing (GFDM), Filterbank-based Multi-Carrier (FBMC), Universal Filtered Multi-Carrier (UFMC) and Bi-orthogonal Frequency Division Multiplexing (BFDM). There are commonalities among those schemes, like including filtering, reduced spectral side-lobe levels and multi-carrier aspects, but also differences.
FBMC has been already discussed for some time in the literature and is within the 5GNOW project investigated as DL CoMP candidate scheme and for operation in fragmented spectrum. FBMC is characterized by per-sub-carrier filtering, long filter lengths and is typically used in conjunction with offset QAM. It is quasi-orthogonal (in the real domain). GFDM drops the orthogonality altogether and is focused on block-wise processing. It is especially targeting short bursts which are desirable for the Tactile Internet. UFMC is a generalization of filtered OFDM and FBMC. It uses a per-subcarrier-block-wise filtering and supports QAM. Within blocks, orthogonality is provided, between blocks it is dropped. It has been shown to be advantageous for the Unified Frame Structure, supporting a mix of synchronous and asynchronous traffic. BFDM with very long symbol lengths is especially efficient in the random access scenario and can then exploit the capabilities of advanced sparsity-aware signal processing.

6.2 Outlook and Future Work

Future steps will be to pick up the 5GNOW waveform candidate schemes, refine their investigation and construct the concept for a new 5G physical layer out of it. D3.2, titled “Intermediate 5GNOW Transceiver and frame structure concept”, thus will add further details to transceivers and frame structure. D3.3, titled “Final 5GNOW Transceiver and frame structure concept” will contain final performance results and optimal waveform parameters for specific scenarios.

7 Abbreviations and References

3GPP	3rd Generation Partnership Project
4G	Fourth Generation
5G	Fifth Generation
5GNOW	5th Generation Non-orthogonal Waveforms for Asynchronous Signaling
ADC	Analog-to-Digital Converter
BER	Bit Error Rate
BFDM	Biorthogonal Frequency Divison Multiplexing
BS	Base Station
CDMA	Code Division Multiple Access
CFO	Carrier Frequency Offset(s)
CoMP	Coordinated Multipoint
CP	Cyclic prefix
CSI	Channel State Information
DAC	Digital-to-Analog Converter
EXALTED	Expanding LTE for Devices
FBMC	Filter Bank Multi-Carrier
FP7	7th Framework Programme
GFDM	Generalized Frequency Division Multiplexing
GSM	Global System for Mobile Communications
H2H	Human-to-Human
IDMA	Interleave Division Multiple Access
ICI	Inter-Carrier Interference
ISI	Inter-Symbol Interference
KPI	Key Performance Indicator
LTE	Long Term Evolution
LTE-A	Long Term Evolution Advanced
MAC	Medium Access Control (layer)
MTC	Machine Type Communication
OFDM	Orthogonal Frequency Divison Multiplexing
PAPR	Peak-to-average power ratio
SER	Symbol error rate
UFMC	Universal Filtered Multi-Carrier

References:

[3GP09] http://www.3gpp.org/ftp/workshop/2009-12-17_ITU-R_IMT-Adv_eval/docs/pdf/REV-090006.pdf, last access 13.11.2012

[3GP10] 3GPP TR 36.814, Further Advancements for E-UTRA Physical Layer Aspects, v9.0.0, Mar. 2010

[3GP11] 3GPP TR 36.819 V11.1.0, Coordinated Multi-point Operation for LTE Physical Layer Aspects, December 2011

[3GP11a] Technical Specification 22.368 V11.2.0 (2011-06) Stage 1 (Release 11), http://www.3gpp.org/ftp/Specs/html-info/22368.htm

[5GPP] 5GNOW Project Proposal, Part B

[BEL10] Bellanger, M., "Efficiency of Filter Bank Multicarrier Techniques in Burst Radio Transmission," Global Telecommunications Conference (GLOBECOM 2010), 2010 IEEE, pp.1,4, 6-10 Dec. 2010.

[BEL10b] M.G. Bellanger et al, "FBMC physical layer: a primer", 06/2010.

[BEL12] Bellanger, M., "FS-FBMC: An alternative scheme for filter bank based multicarrier transmission," Communications Control and Signal Processing (ISCCSP), 2012 5th International Symposium on, pp.1-4, 2-4 May 2012.

[Bel63] P. Bello, "Characterization of randomly time-variant linear channels," *IEEE Trans. Commun.*, vol. COM-11, no. 4, pp. 360–393, Dec. 1963.

[Böl01] H. Bölcskei, "Blind estimation of symbol timing and carrier frequency offset in wireless OFDM system," IEEE Transaction on communication, vol. 49, no. 6, pp. 988–999, 2001.

[Böl02] H. Bölcskei, "Orthogonal frequency division multiplexing based on offset QAM," in *Chapter in "Advances in Gabor Theory*," H. G. Feichtinger and T. Strohmer, Eds. Cambridge, MA; Birkhäuser, 2002.

[Böl03] H. Bölcskei, P. Duhamel, and R. Hleiss, "Orthogonalization of OFDM/OQAM pulse shaping filters using the discrete Zak transform," Signal Process. (EURASIP), vol. 83, no. 7, pp. 1379–1391, Jul. 2003.

[Cis10] Cisco, "Architectural Considerations for Backhaul of 2G/3G and Long Term Evolution Networks", White Paper, 2010 [Available: http://www.cisco.com/en/US/solutions/collateral/ns341/ns973/white_paper_c11-613002.pdf]

[CT06] Cover, T.M.; Thomas, J.A.; "Elements of Information Theory, 2nd ed.," *Wiley-Interscience, New York*, Jul. 2006.

[D2.1] 5GNOW, "5G Cellular Communications Scenarios and System Requirements", Deliverable 2.1, March 2013

[Dau92] I. Daubechies, Ten Lecures onWavelets. Philadelphia, PA: SIAM, 1992.

[DJJ91] I. Daubechies, S. Jaffard, and J. Journé, "A simple Wilson orthonormal basis with exponential decay," SIAM J. Math. Anal., vol. 22, no. 2, pp. 554–572, 1991.

[DL07] Doukopoulos, X.G.; Legouable, R., "Robust Channel Estimation via FFT Interpolation for Multicarrier Systems," Vehicular Technology Conference, 2007. VTC2007-Spring, IEEE 65th, pp.1861-1865, 22-25 April 2007.

[EB09] Eldar, Y.C.; Bölcskei, H., "Block-sparsity: Coherence and efficient recovery," Acoustics, Speech and Signal Processing, 2009. ICASSP 2009. IEEE International Conference on , vol., no., pp.2885,2888, 19-24 April 2009

[FAB95] B. L. Floch, M. Alard, and C. Berrou, "Coded orthogonal frequency division multiplex," Proc. IEEE, vol. 83, no. 6, pp. 982–996, Jun. 1995.

[Far11] B. Farhang-Boroujeny, "OFDM versus filter bank multicarrier," IEEE Signal Process. Mag., vol. 28, pp. 92 –112, May 2011.

[Fet12] G. Fettweis, "A 5G Wireless Communications Vision", Microwave Journal, http://www.microwavejournal.com/articles/print/18751-a-5g-wireless-communications-vision

[FKB09] G. Fettweis, M. Krondorf and S. Bittner, “GFDM - Generalized Frequency Division Multiplexing” in Proceedings of the 69th IEEE Vehicular Technology Conference (VTC Spring'09), Barcelona, Spain

[Fol89] G. B. Folland, Harmonic Analysis in Phase Space. Princeton, NJ: Princeton University Press, 1989.

[GMN+13] I. Gaspar, N. Michailow, A. Navarro, E. Ohlmer, S. Krone, and G. Fettweis, “Low Complexity GFDM Receiver Based On Sparse Frequency Domain Processing” in Proc. 77th IEEE Vehicular Technology Conference, VTC Spring 2013.

[HB12] Chinmay Hegde and Richard G. Baraniuk, “Signal Recovery on Incoherent Manifolds”, ArXiv Preprint, June 2012

[HB12b] C. Hegde and R. G. Baraniuk, "SPIN: Iterative signal recovery on incoherent manifolds," Information Theory Proceedings (ISIT), IEEE International Symposium on pp. 1296-1300, 2012.

[HSF08] Hoeher, P.A.; Schoeneich, H.; and Fricke, J.C.; “Multi-layer interleave division multiple access: theory and practice,” *Europ. Trans. Telecommun. (ETT)*, Vol. 19, Issue 5, pp. 523–536., Aug. 2008.

[IM08] A. Ibing, K. Manolakis, “MMSE Channel Estimation and Time Synchronization Tracking for Cooperative MIMO-OFDM with Propagation Delay Differences”, IEEE ISWCS 2008.

[JB00] A. Janssen and H. Boelcskei, “Equivalence of two methods for constructing tight Gabor frames,” IEEE Signal Process. Lett., vol. 7, no. 4, pp. 79–82, Apr. 2000.

[JS02] A. Janssen and T. Strohmer, “Characterization and computation of canonical tight windows for Gabor frames,” J. Fourier Anal. Appl., vol. 8, no. 1, pp. 1–28, 2002.

[Jun06] P. Jung. (2006).Weighted norms of cross ambiguity functions and Wigner distributions, in Proc. 2006 IEEE Int. Symp. Inf. Theory [Online]. Available: http://arxiv.org/abs/cs.IT/0601017

[JW05] P. Jung and G. Wunder, “On time-variant distortions in multicarrier with application to frequency offsets and phase noise,” IEEE Trans. Commun., vol. 53, no. 9, pp. 1561–1570, Sep. 2005

[JW05b] P. Jung and G.Wunder. (2005). A group-theoretic approach to the WSSUS pulse design problem, in Proc. 2005 IEEE Int. Symp. Inf. Theory [Online]. Available: http://arxiv.org/abs/cs.IT/0501082

[JW07] P. Jung and G.Wunder. (2005). The WSSUS Pulse Design Problem in. Multicarrier Transmission, in IEEE Trans. Commun., vol. 55, no. 9, pp. 1822–1832, Sep. 2007

[KB05] Kusume, K.; Bauch, G.; “CDMA and IDMA: Iterative Multiuser Detections for Near-Far Asynchronous Communications,” in Proc. 2005 IEEE Int. Symp. Personal, Indoor Mobile Radio Commun. (PIMRC’05), Vol. 1, pp. 426–431, Sep. 2005.

[KBU12] Kusume, K.; Bauch, G.; Utschick, W.; “IDMA vs. CDMA: Analysis and Comparison of Two Multiple Access Schemes,” IEEE Trans. Wireless Commun., Vol. 11, No. 1, pp. 78–87, Jan. 2012.

[KK00] Küpfmüller, Karl; Kohn, Gerhard (2000), Theoretische Elektrotechnik und Elektronik, Berlin, Heidelberg: Springer-Verlag, ISBN 978-3-540-56500-0

[KM98] W. Kozek and A. Molisch, “Nonorthogonal pulseshapes for multicarrier communications in doubly dispersive channels,” IEEE J. Sel. Areas Commun., vol. 16, no. 8, pp. 1579–1589, Oct. 1998.

[KMB+13] B. Knoop, Fabian Monsees, Carsten Bockelmann, Dirk Wübben, Steffen Paul, Armin Dekorsy, “Sparsity-Aware Successive Interference Cancellation with Practical constraints”, IEEE/ITG Workshop on Smart Antennas (WSA'13), March 2013

[Koz96] W. Kozek, “Matched Weyl–Heisenberg expansions of nonstationary environments,” Ph.D. dissertation, Vienna Univ. Technol., Vienna, Austria, 1996.

[KS05] G. Kutyniok and T. Strohmer, “Wilson bases for general time-frequency lattices,” SIAM J. Math. Anal., vol. 37, no. 3, pp. 685–711, 2005.

[LIN] Jean Paul Linnartz, “Wireless Communication, Jean Paul Linnartz' Reference Website”, http://www.wirelesscommunication.nl/reference/about.htm.

[LKM04] K. Liu, T. Kadous, and A. M. Sayeed, “Orthogonal time-frequency signaling over doubly dispersive channels,” IEEE Trans. Inf. Theory, vol. 50, no. 11, pp. 2583–2603, Nov. 2004.

[Löw50] P. Löwdin, “On the non-orthogonality problem connected with the use of atomic wave functions in the theory of molecules and crystals,” J. Chem. Phys., vol. 18, pp. 367–370, 1950.

[LTE10] TS 36.211 Evolved Universal Terrestrial Radio Access (E-UTRA); Physical channels and modulation.

[Met13] https://www.metis2020.com/, Project Website

[MGK+12] N. Michailow, I. Gaspar, S. Krone, M. Lentmaier and G. Fettweis “Generalized Frequency Division Multiplexing: Analysis of an Alternative Multi-Carrier Technique for Next Generation Cellular Systems”, in Proceedings of the 9th International Symposium on Wireless Communication Systems (ISWCS'12), Paris, France, August 2012

[Mil91] W. Miller, “Topics in harmonic analysis with application to radar and sonar,” in Radar and Sonar I, R. Blahut, Ed. New York: Springer, 1991.

[MKS03] Ma, X.; Kobayashi, H.; Schwartz, S.C., "Effect of frequency offset on BER of OFDM and single carrier systems," Personal, Indoor and Mobile Radio Communications (PIMRC), IEEE 14th International Symposium on , vol.3, pp.2239,2243, 7-10 Sept. 2003.

[MLJ06] Mahafeno, I.M.; Langlais, C.; Jégo, C.; “Reduced complexity iterative multi-user detector for IDMA (Interleave-Division Multiple Access) system,” in Proc. IEEE Global Telecommun. Conf. 2006 (GLOBECOM’06), Nov.–Dec. 2006.

[MTR+11] Medjahdi, Y.; Terre, M.; Le Ruyet, D.; Roviras, D.; Dziri, A., "Performance Analysis in the Downlink of Asynchronous OFDM/FBMC Based Multi-Cellular Networks," Wireless Communications, IEEE Transactions on , vol.10, no.8, pp.2630,2639, August 2011.

[NRS07] Nagy, O; Reed, M.C.; Shi, Zhenning; “Optimal Detection of IDMA Signals,” in Proc. 2007 IEEE Wireless Commun. Netw. Conf. (WCNC’07), pp. 1236–1240, Mar. 2007.

[NT10] Needell. Deanna and Joel. A. Tropp, "CoSaMP: iterative signal recovery from incomplete and inaccurate samples," Communications of the ACM, vol.53, no. 12, pp. 93-100, 2010.

[Nyq28] H. Nyquist, “Certain Topics in Telegraph Transmission Theory”, Winter Convention of the A.I.E.E., pp.617-644, Feb 13-17, 1928

[PFG12] Poveda, H.; Ferré, G.; Grivel, E.; “Frequency Synchronization and Channel Equalization for an OFDM-IDMA Uplink System,” 2012 IEEE Int. Conf. Acoust., Speech Signal Process. (ICASSP’12), pp. 3209–3212, Mar. 2012.

[PHY08a] Deliverable D5.1, “Prototype filter and filter bank structure”, ICT–211887 PHYDYAS, July 2008.

[PHY08b] Deliverable 2.1, “Transmit/receive processing (single antenna)”, ICT-211887 PHYDYAS, July 2008.

[PLL03] Li Ping; Lihai Liu; Leung, W. K., “A simple approach to near-optimal multiuser detection: interleave-division multiple-access,” IEEE WCNC 2003. March 2003

[PLW+02] Ping Li; Liu, Lihai; Wu, Keying; Leung, W.K.; “A Unified Approach to Multiuser Detection and Space-Time Coding with Low Complexity and Nearly Optimal Performance,” in Proc. 2002 Annu. Allerton Conf. Commun., Control, Comput., pp. 170–179, Oct. 2002.

[PLW+06] Ping, Li; Liu, Lihai; Wu, Keying; Leung, W.K.; “Interleave-Division Multiple Access,” IEEE Trans. Wireless Commun., Vol. 5, No. 4, pp. 938–947, Apr. 2006.

[PWL+02] Ping, Li; Wu, Keying; Liu, Lihai; Leung, W.K.; “A Simple, Unified Approach to Nearly Optimal Multiuser Detection and Space-Time Coding,” in Proc. 2002 IEEE Inf. Theory Workshop (ITW’02), pp. 53–56, Oct. 2002.

[SB03] T. Strohmer and S. Beaver, “Optimal OFDM design for time-frequency dispersive channels,” IEEE Trans. Commun., vol. 51, no. 7, pp. 1111– 1122, Jul. 2003.

[SGS+05] J. Salo, G. Del Galdo, J. Salmi, P. Kyösti, M. Milojevic, D. Laselva, and C. Schneider. (2005, Jan.) MATLAB implementation of the 3GPP Spatial Channel Model (3GPP TR 25.996) [Online]. Available: http://www.tkk.fi/Units/Radio/scm/

[SH05] Schoeneich, H.; Hoeher, P.A.; “Semi-Blind Pilot-Layer Aided Channel Estimation with Emphasis on Interleave-Division Multiple Access Systems,” in Proc. IEEE Global Telecommun. Conf. 2005 (GLOBECOM’05), pp. 3513–3517, Dec. 2005.

[SMH02] D. Schafhuber, G. Matz, and F. Hlawatsch, “Pulse-shaping ofdm/bfdm systems for time-varying channels: Isi/ici analysis, optimal pulse design, and efficient implementation,” in in Proc. IEEE Symp. PIMRC, pp. 1012–1016, 2002.

[Son12] P. Sondergaard, “Efficient algorithms for the discrete Gabor transform with a long FIR window,” J.Fourier Anal. Appl., vol. 18, no. 3, pp. 456–470, 2012.

[STB09] S. Sesia, I. Touk, and M. Baker, “LTE, The UMTS Long Term Evolution: From Theory to Practice”. Wiley Publishing, 2009.

[SW70] H. C. Schweinler and E. P. Wigner, “Orthogonalization methods,” J. Math. Phys., vol. 11, no. 5, pp. 1693–1694, May 1970.

[VSK12] Vishvaksenan, K.S.; Seshasayanan, R.; Krishnamoorthy, Y.; “Joint VBLAST/STBC Assisted MIMO MC-IDMA System in Frequency Selective Channels: Performance Results,” in Proc. 2012 Int. Conf. Commun. Signal Process. (ICCSP’12), Apr. 2012.

[VWS+13] V. Vakilian, T. Wild, F. Schaich, S. t. Brink, J.-F. Frigon, “Universal Filtered Multi-Carrier Technique for Wireless Systems Beyond LTE”, Accepted for 9th International Workshop on Broadband Wireless Access, IEEE Globecom'13, Atlanta, GA, USA, December 2013

[Wei] http://www.weightless.org/

[Wil91] C. H. Wilcox, “The synthesis problem for radar ambiguity functions,” in Radar and Sonar I, R. Blahut, Ed. New York: Springer, 1991.

[WKB+13] G. Wunder, M. Kasparick, S. ten Brink, F. Schaich, T. Wild, I. Gaspar, E. Ohlmer, S. Krone, N. Michailow, A. Navarro, G. Fettweis, D. Ktenas, V. Berg, M. Dryjanski, S. Pietrzyk, and B. Eged, “5GNOW: Challenging the LTE Design Paradigms of Orthogonality and Synchronicity”, Mobile and Wireless Communication Systems for 2020 and beyond, Workshop @ 77th IEEE Vehicular Technology Spring Conference (VTC2013 Spring), Dresden, Jun. 2013;

[WKW+13] G. Wunder, M. Kasparick, T. Wild, F. Schaich, Y. Chen, S. t. Brink, I. Gaspar, N. Michailow, A. Navarro, G. Fettweis, N. Cassiau, D. Ktenas, M. Dryjanski, S. Pietrzyk, and B. Eged, “5GNOW: Application Challenges and Initial Waveform Results “, Proceedings Future Network & Mobile Summit 2013, Lisbon, July 2013.

[WKM13] G. Wunder, Martin Kasparick, Dick Maryopi, „Optimality of Tail behavior of Nyquist filters for Random Access Operation”, *to be submitted to ICC 2013 (planned)*

[WJW13] G. Wunder, Peter Jung, Chen Wang, „Compressive Random Access”, *to be submitted to ICC 2013 (planned)*

[XTY+03] Xianbin Wang; Tjhung, T.T.; Yiyan Wu; Caron, B., "SER performance evaluation and optimization of OFDM system with residual frequency and timing offsets from imperfect synchronization," Broadcasting, IEEE Transactions on, vol.49, no.2, pp.170-177, June 2003.

[ZG11] H. Zhu and G. Giannakis , “Exploiting sparse user activity in multiuser detection”, IEEE Trans. on Communications, vol.59, no. 2, pp 454-465, Feb 2011

--- End of Document Main Body---

Appendix

Appendix A: Principles of Waveform Design and Pulse Shaping

A.1 Notations

$\bar{.}$ denotes complex conjugate
$.^*$ means conjugate transpose
i imaginary unit
$\hat{\gamma}$ is the Fourier transform of γ defined by the pair

$$\hat{\gamma}(\omega) = \int_{\mathbb{R}} \gamma(t) e^{-i\omega t} dt \quad \text{(A.1.1)}$$

$$\gamma(t) = \frac{1}{2\pi} \int_{\mathbb{R}} \hat{\gamma}(\omega) e^{i\omega t} d\omega \quad \text{(A.1.2)}$$

B Angular bandwidth
E Expectation operator
$\mathbb{Z}$ integers
$\mathbb{R}$ real numbers
$\mathcal{L}_p(\mathbb{R})$ continuous L_p signals, L_2 is the space of energy signals
ℓ_p discrete l_p signals

A.2 Classical waveform theory

In this section we introduce some of the elements of classical waveform theory forming the basis for the multicarrier theory. The following is a list of key properties of waveforms.

A.2.1 Nyquist criterion

Waveform design (or so-called pulse shaping) is as old as the field of digital communications itself. One of the oldest contributor is [Nyq28] to whom the first and second Nyquist criterion is dedicated. Specifically, the second Nyquist criterion is of some importance to communication engineers and reads as follows:

1^{st} Nyquist Criterion: Suppose we have a pulse γ with Bandwidth B: then γ has zeros at the sampling points $t_i = \frac{i\pi}{B}$ if and only if

$$\sum_k \hat{\gamma}\left(\omega - k\frac{L+1}{2}B\right) = \frac{\pi}{B} \quad \text{(A.2.1)}$$

The content establishes the first waveform design criterion in the communication literature. It says to communicate $\frac{B}{\pi}$ complex symbols/s without intersymbol interference the periodically extended frequency response of the pulse adds up to a constant. The condition is illustrated for some pulse depicted in Figure A.2.. The time domain description of this pulse is given by

$$\gamma_L(t) = \frac{2\sin\left(\frac{L+1}{2}Bt\right)\sin\left(\frac{L-1}{2}Bt\right)}{L(L-1)B^2t^2} \quad \text{(A.2.2)}$$

Here the factor L is the factor determing the excess bandwidth. Obviously the pulse with smallest bandwidth is the famous sinc kernel with L=1

$$\gamma(t) = \frac{\sin(Bt)}{Bt} \quad \text{(A.2.3)}$$

Another popular pulse is the raised cosine pulse. The pulses defer in their time behaviour significantly as discussed next.

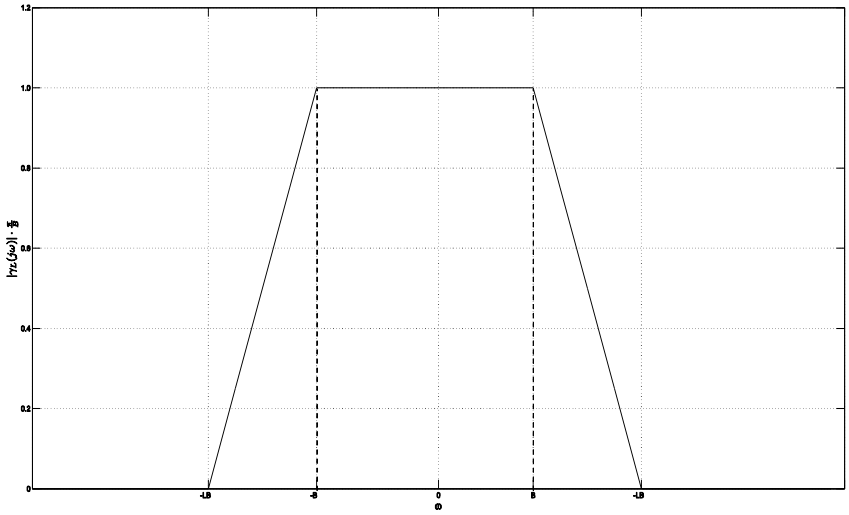

Figure A.2.13: Model pulse which satisfies the Nyquist criterion: Note that in case of zero excess bandwidth the pulse reduces to the sinc pulse (note that typically the bandwidth B is centered in the middle of the tail)

A.2.2 L_p norms

The energy of the sinc-pulse is

$$\|\gamma(t)\|_2^2 = \frac{1}{2\pi}\|\hat{\gamma}(\omega)\|_2^2 = \frac{\pi}{B} \quad \text{(A.2.4)}$$

Naturally, the sinc pulse satisfies

$$\|\gamma(t)\|_1 = \infty \quad \text{(A.2.5)}$$

However, for the pulse in Figure A.2.13 we have

$$\frac{B}{\pi}\|\gamma_L(t)\|_1 \leq \sqrt{\frac{L+1}{L-1}} \tag{A.2.6}$$

Hence, the $\mathcal{L}_p(\mathbb{R})$ norms differ significantly from each other for different waveforms [WKM13]. They are of utmost interest for determining the impact of synchronization errors etc.

A.2.3 Tail behavior

The sinc pulse has only theoretical meaning since the sums of the absolute samples of the tails add up to infinity. This means small distortion due imperfect timing has catastrophic effect. On the other hand the pulse in Figure A.2. has different behavior. It can be shown that the pulse has almost optimal behavior in terms of absolute error measured. Defining the error term as (which is independent of B and depends on L only):

$$\Delta(L) \leq \max_{-\frac{n}{2n+2}\leq t\leq\frac{n}{2n+2}} \frac{1}{L}\sum_{l\in\mathcal{I}}\left|\gamma_L\left(t-\frac{t}{L}\right)\right| \tag{A.2.7}$$

We can show [WKM13] that

$$\Delta(L) \leq \max_{-\frac{n}{2n+2}\leq t\leq\frac{n}{2n+2}} \frac{1}{2n+2}\sum_{l=0}^{2n+1}\left|\sum_{k=-n}^{n} e^{jk\left(\frac{\pi t}{n}-\frac{l\pi}{n+1}\right)}\right| \tag{A.2.8}$$

for any kernel which satisfies the Nyquist criterion with excess bandwidth $L=\frac{n+1}{n}\leq 2$ and some integer n. The formula can be easily evaluated which is done in Figure A.2.14.

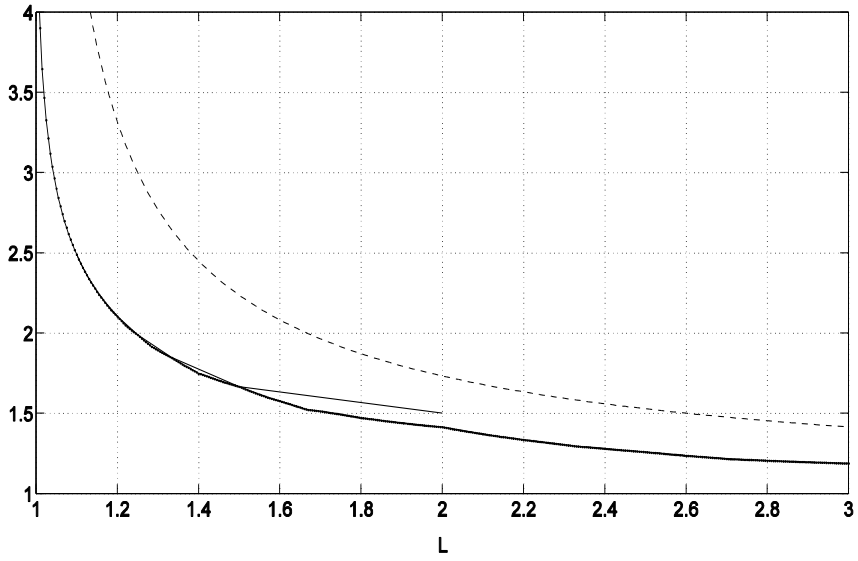

Figure A.2.14: Lower and upper bound for the distortion error $\Delta(L)$. The dashed line is the universal upper bound on the $\|\gamma_L(t)\|_1$ norm.

A.2.4 General pulses

The analysis can be taken to analyze arbitrary pulses by approximating the given pulse response in the frequency domain. The approach is illustrated in Figure A.2.15. Note that the impulse response of the triangle kernel follows from the trapezoidal kernel and is given by:

$$\gamma_L(t) = \frac{2\sin^2\left(\frac{Bt}{2}\right)}{B^2t^2} \quad \text{(A.2.9)}$$

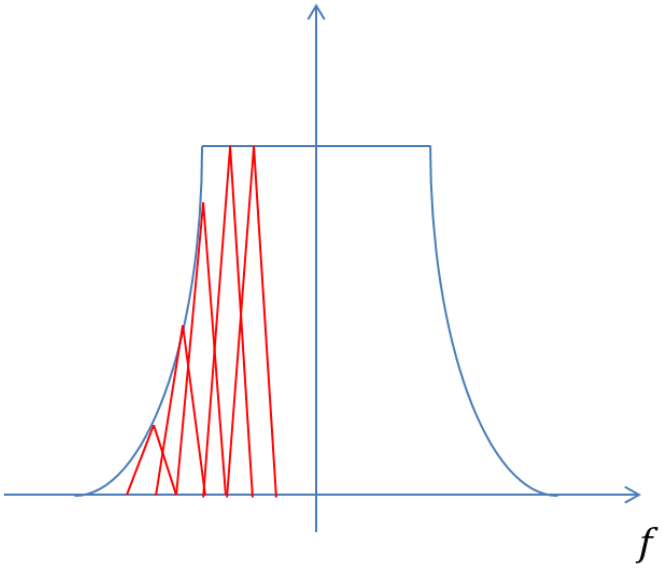

Figure A.2.15: Approximation of arbitrary frequency responses

A.3 Multicarrier theory

The material presented in the following sections is mainly from [JW07].

A.3.1 Gabor signaling

Conventional OFDM and pulse shaped Offset QAM (OQAM) can be jointly formulated within the concept of generalized multicarrier schemes which mean that some kind of time-frequency multiplexing will be performed. To avoid cumbersome notation we will adopt a two-dimensional index notation $n = (n_1, n_2) \in \mathbb{Z}$ for time-frequency slots n. In our framework the baseband transmit signal is

$$s(t) = \sum_{n\in\mathcal{I}} x_n \gamma_n(t) = \sum_{n\in\mathcal{I}} x_n (\boldsymbol{S}_{\Lambda n}\gamma)(t) \quad \text{(A.3.1)}$$

where

$$\left(S_\mu \gamma\right)(t) \stackrel{\text{def}}{=} e^{i2\pi\mu_2 t}\gamma(t-\mu_1) \quad \text{(A.3.2)}$$

and the coefficients x_n are the complex data symbols at time instant n_1 and subcarrier index n_2 with the property $E\{x\, x^*\} = \mathbb{I}$, where $x = (\dots, x_n, \dots)^T$. Here, $\mu = (\mu_1, \mu_2)$ is a time-frequency shifted version of the transmit pulse γ, i.e. $\gamma_n \stackrel{\text{def}}{=} \boldsymbol{S}_{\Lambda n}\gamma$ is shifted according to a lattice $\Lambda\mathbb{Z}^2$ where the matrix Λ denotes its 2 x 2 real generator matrix. The indices $n = (n_1, n_2)$ range over the doubly-countable set $\mathcal{I} \subset \mathbb{Z}^2$, referring to the data burst to be transmitted. This lattice structure in the time-frequency plane (or phase space) is called Gabor signaling. Moreover, because the time-frequency shift operators (or phase space displacement operators) S_μ are unitary representations of the Weyl-Heisenberg group (see for example [Fol89], [Mil91]) on$\mathcal{L}_2(\mathbb{R})$ this also known as Weyl-Heisenberg signaling.

In practice Λ is often restricted to be diagonal, i.e. $\Lambda = diag(T, F)$. However Gabor based multicarrier transmission can be generalized to other lattices as well [SB03]. The time-frequency sampling density is related to the bandwidth efficiency (in complex symbols) of the signaling, i.e. $\epsilon \stackrel{\text{def}}{=} |\det \Lambda^{-1}|$, which gives

$$\epsilon = (TF)^{-1} \tag{A.3.3}$$

for $\Lambda = diag(T, F)$.

Example:

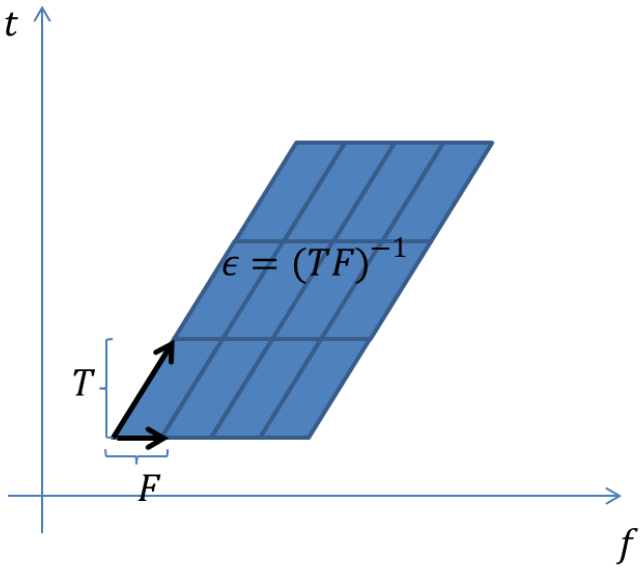

A.3.2 Spreading function

We will denote the linear time-variant channel by $\boldsymbol{\mathcal{H}}$ and the additive white Gaussian noise process (AWGN) by $n(t)$. The received signal is then

$$r(t) = (\boldsymbol{\mathcal{H}}s)(t) + n(t) = \int_{\mathbb{R}^2} \sum(\mu)\big(S_\mu s\big)(t)d\mu + n(t) \tag{A.3.4}$$

with $\sum: \mathbb{R}^2 \rightarrow \mathbb{C}$ being a realization of the (causal) channels spreading function with finite support. We used here the notion of the *wide-sense stationary uncorrelated scattering* (WSSUS) channel [Bel63] and its decomposition into time-frequency shifts.

A.3.3 Scattering function

In the WSSUS assumption the channel is characterized by the second order statistics of $\sum(.)$, i.e. the scattering function $C : \mathbb{R}^2 \rightarrow \mathbb{R}_+$

$$E\big\{\sum(\mu)\overline{\sum(\mu')}\big\} = C(\mu)\delta(\mu - \mu') \tag{A.3.5}$$

Moreover we assume that

$$E\{\sum(\mu)\} = 0. \tag{A.3.6}$$

Without loss of generality we use $\|C\|_1 = 1$, which means that the channel has no overall path loss.

A.3.4 Ambiguity function

To obtain the data symbol $\tilde{x}_m$ the receiver projects on $g_m \stackrel{\text{def}}{=} S_{\Lambda m} g$ with $m \in \mathcal{I}$, i.e.

$$\tilde{x}_m = \langle g_m, r \rangle = \langle S_{\Lambda m} g, r \rangle = \int e^{-i2\pi(\Lambda m)2t} \overline{g(t-(\Lambda m)_1)} r(t) dt \qquad \text{(A.3.7)}$$

By introducing the elements

$$H_{m,n} \stackrel{\text{def}}{=} \langle g_m, \boldsymbol{\mathcal{H}} \gamma_n \rangle = \int_{\mathbb{R}^2} \sum(\mu) \langle g_m, \boldsymbol{S_\mu} \gamma_n \rangle d\mu \qquad \text{(A.3.8)}$$

of the channel matrix $H \in \mathbb{C}^{\mathcal{I}X\mathcal{I}}$, the multicarrier transmission can be formulated as the linear equation $\tilde{x} = Hx + \tilde{n}$, where $\tilde{n} = (\ldots, \langle g_m, n \rangle, \ldots)^T$ is the vector of the projected noise having variance $\sigma^2 := E_n\{|\langle g_m, n \rangle|^2\}$ per component. If we assume that the receiver has perfect channel knowledge (given by $\sum$) "one—tap" (zero forcing) equalization would be of the form $\tilde{x}_m^{eq} = H_{m,m}^{-1} \tilde{x}_m$ (or alternatively MMSE equalization if σ^2 is known), where

$$H_{m,m} = \int_{\mathbb{R}^2} \sum(\mu) e^{-i2\pi(\mu_1(\Lambda m)_2 - \mu_2(\Lambda m)_1)} \langle g, S_\mu \gamma \rangle d\mu \qquad \text{(A.3.9)}$$

$$= \int_{\mathbb{R}^2} \sum(\mu) e^{-i2\pi(\mu_1(\lambda m)_2 - \mu_2(\lambda m)_1)} \mathbf{A}_{g\gamma}(\mu) d\mu \qquad \text{(A.3.10)}$$

Here $\mathbf{A}_{g\gamma}(\mu) \stackrel{\text{def}}{=} \langle g, S_\mu \gamma \rangle$ is the well known cross ambiguity function of g and γ.

A.3.5 Biorthogonality (or generalized Nyquist condition)

We adopt the following ℓ_2-normalization of the pulses. The normalization of g will have no effect on the later used system performance measures. The normalization of γ is typically determined by some transmit power constraint and will scale later only the noise variance $\sigma^2 \to \sigma^2 / \|\gamma\|_2^2$. Thus we assume g and γ to be normalized to one, i.e. $\|g\|_2^2 = \|\gamma\|_2^2 = 1$. Furthermore we might (or not) enforce orthogonal transmit/receive signaling

$$\langle \gamma_m, \gamma_n \rangle = \delta_{mn}), (\langle g_m, g_n \rangle = \delta_{mn} \qquad \text{(A.3.11)}$$

or biorthogonality between transmitter and receiver, i.e.

$$\langle g_m, \gamma_n \rangle \sim \delta_{mn}. \qquad \text{(A.3.12)}$$

But note that, advanced equalization techniques like interference cancellation will suffer from noise--enhancement and noise correlation introduced by non-orthogonal receivers.

A.3.6 Complex Schemes

In this approach full complex data symbols are transmitted according to (1). Depending on the lattice density ($\epsilon < 1$) this includes redundancy. In the sense of biorthogonality it is then desirable to achieve $\langle g_m, \boldsymbol{\mathcal{H}} \gamma_n \rangle \sim \delta_{mn}$ for a particular class of channels $\boldsymbol{\mathcal{H}}$. For example the classical OFDM system exploiting a cyclic prefix (cp-OFDM) is obtained by assuming a lattice generated by $\Lambda = diag(T, F)$ and setting γ to the rectangular pulse

$$\gamma(t) = \frac{1}{\sqrt{T_u+T_{cp}}}\,\chi[-T_{cp}\,,T_u](t) \qquad \text{(A.3.13)}$$

The function $\chi\left[-T_{cp}\,,T_u\right]$ is the characteristic function of the interval $\left[-T_{cp}\,,T_u\right]$, where T_u denotes the length of the useful part of the signal and $-T_{cp}$ the length of the cyclic prefix ($\approx 10\%\ T_u$), hence the OFDM overall symbol period is $T = T_u+T_{cp}$. The OFDM subcarrier spacing is $F = 1/T_u$. At the OFDM receiver the rectangular pulse $g(t) = \frac{1}{\sqrt{T_u}}\,\chi[0\,,T_u](t)$ is used which removes the cyclic prefix. The bandwidth efficiency of this signaling is given as

$$\epsilon = \left(TF\right)^{-1} = T_u/\left(T_u+T_{cp}\right) < 1\,. \qquad \text{(A.3.14)}$$

It can be easily verified that $\mathbf{A}_{g\gamma}\left((\tau+\ m_1T, m_2F)\right) = \sqrt{\epsilon}\delta_{m,0}$ if $0 \le \tau \le T_{cp}$ (or see [JW05] for the full formula). i.e.

$$H_{m,m} = \langle g_m, \boldsymbol{\mathcal{H}}\gamma_n\rangle = \sqrt{\epsilon}\hat{h}(m_2F)\delta_{m,n} \qquad \text{(A.3.15)}$$

holds for all channel realization as long as the causal scattering function fulfills $B_D = 0$ and $\tau_d \le T_{cp}$, where $\tau_d(B_D)$ is its maximal delay (one-sided Doppler) support. $\hat{h}(f)$ denotes the Fourier transform of the impulse response $h(\tau) = \sum\left((\tau,0)\right)$ that corresponds to the time-invariant channel. Therefore cp-OFDM is a powerful signaling, which diagonalizes time-invariant channels, but at the cost of signal power (the redundancy is not used) and bandwidth efficiency.

The latter equation does not hold anymore if the channels are doubly-dispersive, as for example modeled by the WSSUS assumptions. If considering other pulse shapes independent of a particular realization $\boldsymbol{\mathcal{H}}$ it is also not possible achieve a relation similar to (8), which will be explained later on.

So it remains to achieve at least $\langle g_m, \gamma_n\rangle \sim \delta_{mn}$ at nearly optimal bandwidth efficiency $\epsilon \approx 1$. But one of the deeper results in Gabor theory, namely the Balian-Low Theorem (see for example [Dau92]), states that (bi-)orthogonal pulses at efficiency $\epsilon \approx 1$ must have bad time-frequency localization properties (efficiency $\epsilon = 1$ localization). Indeed, in discrete implementation the localization of orthogonalized Gaussians for efficiency $\epsilon \ge 1$ and ''tighten'' Gaussians for efficiency $\epsilon < 1$ peaks at the critical density efficiency $\epsilon = 1$ so that pulse shaping is mainly prohibited for band efficient complex schemes if still (bi-) orthogonality is desired. Nevertheless in contrast to cp-OFDM it is via pulse shaping (for efficiency $\epsilon < 1$) still possible to make use of the redundancy.

A.3.7 Real Schemes

For those schemes an inner product $\mathrm{Re}\{\langle .,. \rangle\}$ is considered, which is realized by OQAM based modulation for OFDM (also known as OQAM/OFDM) [Cha66]. It is obtained in (1) and (4) with a lattice generated by $\Lambda = diag(T,F)$ having $|\det\Lambda| = 1/2$. Before modulation the mapping $x_n = i^n x_n^R$ has to be applied, where $x_n^R \in \mathbb{R}$ is the real-valued information to transmit. We use here the notation $i^n = i^{n_1} + i^{n_2}$. Furthermore other phase mappings are possible, like $i^{n_1+n_2+2n_1n_2}$. After demodulation $\tilde{x}_m^R = \mathrm{Re}\{i^{-m}\tilde{x}_m\}$ is performed. Moreover, the pulses (g,γ) have to be real. Thus, formally the transmission of the real information vector $x^R = (\dots, x_n^R, \dots)^T$ can be written as $\tilde{x}^R = H^R x^R + \tilde{n}^R$, where the real channel matrix elements are:

$$H_{m,n}^R = \mathrm{Re}\{i^{-m}H_{m,n}\} = \mathrm{Re}\{i^{n-m}\langle g_m, \boldsymbol{\mathcal{H}}\gamma_n\rangle\} \qquad \text{(A.3.16)}$$

and ''real-part'' noise components are $\tilde{n}_m^R = \mathrm{Re}\{i^{-m}\langle g_m, n\rangle\}$. Note that there exists no such relation for OQAM based multicarrier transmission equivalent to (8) for cp-OFDM. Hence, also in time-invariant channels there will be ICI. But in the absence of a channel, biorthogonality of the form $\Re = \{\langle g_m, \gamma_n\rangle\} = \delta_{m,n}$ can be achieved. Furthermore it is known that the design of orthogonal OQAM based multicarrier transmission is equivalent to the design of orthogonal Wilson bases [Böl02]. Because the system operates with real information $\epsilon = 2$ the effective efficiency is one, but in the view of pulse shaping it is not affected by the Balian-Low theorem.
It is known that the construction of orthogonal Wilson bases is equivalent to the design of tight frames having redundancy two (which will be explained later on in the paper)[DJJ91] . It will turn out that this equivalence holds also for the WSSUS pulse shaping problem considered in this paper if assuming some additional symmetry for the noise and the spreading function of the channel. Finally, extensions of classical Wilson bases to non-separable lattices are studied in [KS05].

A.3.8 Multicarrier pulse shaping

1) Step one (Gain optimization)

In the first step the maximization of the averaged *channel gain* $E_{\mathcal{H}}\{a\}$ is considered, which is

$$E_{\mathcal{H}}\{a\} = \int_{\mathbb{R}^2} \left|\mathbf{A}_{g\gamma}(\mu)\right|^2 C(\mu)d\mu \leq \|C\|_1 \|g\|_2^2 \|\gamma\|_2^2 = 1. \qquad \text{(A.3.17)}$$

In this context (13) was first introduced in [KM98], respectively [Koz96], but similar optimization problems already occurred in radar literature much earlier. In particular for the elliptical symmetry of $C(.)$, Hermite functions establish local extremal points as found in [Koz96]. If $C(.)$ is a two-dimensional Gaussian, the optimum is achieved *only* using Gaussian pulses for g and γ matched in spread and offset to $C(.)$ (see [Jun06]).
In IV-B we will establish the maximization of (13) as global-type optimization problem closely related to bilinear programming. However, already [JW04] has proposed the following lower bound

$$E_{\mathcal{H}}\{a\} \geq \left|\langle g, \left(\int_{\mathbb{R}^2} \mathrm{S}_\mu \, C(\mu)d\mu\right)\gamma\rangle\right|^2 \stackrel{\text{def}}{=} \left|\langle g, \mathcal{L}_\gamma \rangle\right|^2 \qquad \text{(A.3.18)}$$

which admits a simple direct solution given as the maximizing eigenfunctions of $\mathcal{L}^*\mathcal{L}$, respectively $\mathcal{L}\mathcal{L}^*$. Furthermore the lower bound is analytically studied in [JW05b].

Pulse Scaling: The maximization of (13) is still a difficult task, numerically and analytically. However, it is possible to obtain a simple scaling rule by second order approximation of the cross ambiguity function. For g and γ being even and real, the squared cross ambiguity can be approximated for small $|\mu|$ as follows [JW07]

$$\left|\mathbf{A}_{g\gamma}(\mu)\right|^2 \approx \langle g, \gamma\rangle^2 \, [1 - 4\pi^2(\mu_2^2\sigma_t^2 + \mu_1^2\sigma_f^2)] \qquad \text{(A.3.19)}$$

with $\sigma_t^2 = \langle t^2 g, \gamma\rangle / \langle g, \gamma\rangle$ and $\sigma_f^2 = \langle f^2 \hat{g}, \hat{\gamma}\rangle / \langle g, \gamma\rangle$. The latter is a slight extension of the often used approximation for the auto-ambiguity function ($g = \gamma$), which gives ellipses as contour lines of (15) in the time-frequency plane [Wil91]. The optimization problem for the averaged channel gain turns under the constraint $\langle g, \gamma\rangle = const.$ now into the following scaling problem:

$$\min_{(\sigma_t, \sigma_f)} \int_{\mathbb{R}^2} [\mu_2^2\sigma_t^2 + \mu_1^2\sigma_f^2] C(\mu)d\mu \qquad \text{(A.3.20)}$$

which is an optimization of σ_t and σ_f only. For a separable scattering function $(\mu) = C_t(\mu_1)C_f(\mu_2)$, this further simplifies to

$$\min_{(\sigma_t,\sigma_f)} C^{(f)}(\sigma_t^2) + C^{(t)}\left(\sigma_f^2\right) \tag{A.3.21}$$

where $C^{(f)} = \|C_t\|_1 \int C_f(v)\, v^2\, dv$ and $C^{(t)} = \left\|C_f\right\|_1 \int C_t(\tau)\, \tau^2\, d\tau$ are the corresponding scaled second moments of the scattering function. Optimal points have to fulfill the relation

$$\frac{\partial}{\partial(\sigma_t/\sigma_f)}\left[C^{(f)}(\sigma_t^2) + C^{(t)}\left(\sigma_f^2\right)\right] = 0 \iff \frac{\sigma_t}{\sigma_f} = \sqrt{\frac{C^{(t)}}{C^{(f)}}}. \tag{A.3.22}$$

Already in [Koz96] this matching rule was found for $C(\mu) = \frac{1}{2B_D\,\tau_D}\,\chi_{\left[-\frac{\tau_D}{2},\ \frac{\tau_D}{2}\right]}(\mu_1)\,\chi_{[-B_D,\,B_D]}(\mu_2)$ (non-causal) and for centered flat elliptic shapes.
For this special case the rule was also studied in [LKM04] whereas the latter derivation of the scaling law in terms of moments needs no further assumptions. The pulses itself which have to be scaled accordingly were not provided by this second order approximation. But in [JW05b] we have shown that an operator-algebraic formulation leads to eigenvalue problem for Hermite-kind differential operator, having for small $C^{(t)}C^{(f)}$ Gaussians as optimal eigenfunctions. Moreover this approach gives some hint on the optimal phase space displacement between g and γ, which is also not provided by (15). Hence, Gaussians are a good choice for underspread channels $C^{(t)}C^{(f)} \ll 1$ if only pulse scaling is considered.

2) Step two (Interference minimization)

The main objective in this step is the minimization of the upper bound on the sum of interferences from other lattice points, i.e. $E_{\mathcal{H}}\{b\} \leq B_\gamma - E_{\mathcal{H}}\{a\}$ .Let us consider a pulse pair $\{g,\gamma\}$ that is returned by step one. Hence they represent some kind of ''single-pulse channel optimality'' achieved by scaling or direct solution of the gain optimization problem, i.e. let us say they achieve the value $F(g,\gamma) \stackrel{\text{def}}{=} E_{\mathcal{H}}\{a\}$. As we will show later on in more detail the optimal values of $F(g,\gamma)$ and $\mathrm{SINR}(g,\gamma,\Lambda)$ depend only γ, where g is given by the ''optimum'' (or vice versa), i.e.

$$F(\gamma) \stackrel{\text{def}}{=} \max_{\|g\|_2=1} F(g,\gamma) \tag{A.3.23}$$
$$\mathrm{SINR}(\gamma,\Lambda) \stackrel{\text{def}}{=} \max_{\|g\|_2=1} \mathrm{SINR}(g,\gamma,\Lambda) \tag{A.3.24}$$

Recalling now the Bessel bound $B_\gamma = \rho\left(\mathrm{S}_{\gamma,\Lambda}\right)$ related to this ''optimal'' γ, we have

$$\mathrm{SINR}(\gamma,\Lambda)^{-1} \leq \frac{\sigma^2+\rho(\mathrm{S}_{\gamma,\Lambda})}{F(\gamma)} - 1. \tag{A.3.25}$$

To arrive at what is commonly known as pulse orthogonalization we consider a linear transformation O, which minimizes the Bessel bound, fulfills $\|O\gamma\|_2 = \|\gamma\|_2$, and ensures that $F(O\gamma) \approx F(\gamma)$. For non-dispersive channels, the latter, this of course unproblematic since $F(O\gamma) = F(\gamma) = 1$. However, for the doubly dispersive case this is difficult to fulfill and it is exactly the gap which can be filled by non-orthogonal pulses. Nevertheless, under this assumption, the problem decouples and we would have for any g with $F(g,\gamma) = F(\gamma)$

$$\inf_{\tilde{\gamma}} \mathrm{SINR}(\tilde{\gamma}, \Lambda)^{-1} \leq \frac{\sigma^2 + \min_O(\rho(\mathrm{S}_{O\gamma,\Lambda}))}{F(\gamma)} - 1. \quad \text{(A.3.26)}$$

The remaining minimization in this approach can be performed for the given ''optimal'' γ as follows. To this end, let $O = \beta \mathrm{S}_{\gamma,\Lambda}^{\alpha}$ and assume $\mathcal{G}(\gamma, \Lambda, \mathbb{Z}^2)$ establishes a frame, we have

$$\mathrm{S}_{O\gamma,\Lambda} = O\mathrm{S}_{\gamma,\Lambda}\, O^* = \beta^2 \mathrm{S}_{\gamma,\Lambda}^{1+2\alpha} \overset{\alpha=-1/2}{=} \beta^2 \mathbb{I} \quad \text{(A.3.27)}$$

because $\mathrm{S}_{\gamma,\Lambda}$ commute with each S_{λ} for $\lambda \in \Lambda\mathbb{Z}^2$; hence, its powers. Thus, with $\alpha \to -\frac{1}{2}$, we obtain a tight frame which has minimal Bessel bound $\beta^2 = |\det \Lambda|$, i.e. we achieved the minimum in the right-hand side of (17). This well known procedure [Dau92] was already applied for the pulse shaping problem in [SB03] and has its origins in frame theory. Independently a different method γ being a Gaussian was proposed in the context of OQAM [FAB95], which yields the so called *IOTA pulse* (IOTA= Isotropic Orthogonal Transform Algorithm). It is known that IOTA is an equivalent method to obtain a tight frame [JB00]. But note that this method does not work in the general case. Furthermore, because of the integer oversampling (two is needed for OQAM) the calculation of $\mathrm{S}_{\gamma,\Lambda}$ simplifies much in the Zak-domain and can be done using efficient FFT-based methods [Böl03]. The extension to the case where $\mathcal{G}(\gamma, \Lambda, \mathbb{Z}^2)$ is an incomplete Riesz basis is done by Ron-Shen duality. In this case, the minimal Bessel bound is achieved by an ONB, which is given by $\mathcal{G}\left(\mathrm{S}_{\gamma,\Lambda^\circ}^{-1/2}\gamma, \Lambda, \mathbb{Z}^2\right)$, i.e.given by the computation of a tight frame on the adjoint lattice. Interestingly the resulting orthogonalization procedure based on duality is equivalent to the known Schweinler-Wigner [SW70] or Löwdin [Löw50] orthogonalization. Hence, we arrive at the following operator

$$O_{\gamma,\Lambda} = \beta \begin{cases} \mathrm{S}_{\gamma,\Lambda}^{-1/2} & |\det \Lambda| \leq 1 \\ \mathrm{S}_{\gamma,\Lambda^\circ}^{-1/2} & \text{else} \end{cases} \quad \text{(A.3.28)}$$

to be applied on γ to minimize the Bessel bound (β ensures the normalization). To perform this operation a lattice with $\Lambda^{-1} = \epsilon$ has to be fixed. In the previous derivations the crucial assumption $F(O\gamma) = F(\gamma)$ was made and it would be therefore desirable to choose the Λ minimizing $\delta_1(\Lambda) = F(\gamma) - F\left(O_{\gamma,\Lambda}\gamma\right) \geq 0$, which is a rather complicated optimization. However, it is known that $O_{\gamma,\Lambda}\gamma$ is (under all B_γ minimizer) closest γ in the $\mathcal{L}_2$-sense [JS02], i.e. $\min_{B_d^2=|\det\Lambda|} \|d - \gamma\|_2 = \left\|O_{\gamma,\Lambda}\gamma - \gamma\right\|_2 = \delta_2(\Lambda)$. The relation between $\delta_1(\Lambda)$ and $\delta_2(\Lambda)$ is out of the scope of this paper, but it is $\delta_1(\Lambda) \to 0$ whenever $\delta_2(\Lambda) \to 0$. In summary one has to expect from these arguments that non-orthogonal pulse shapes obtained from direct SINR optimization algorithms [JW07] should yield in general higher SINR values for (full) doubly-dispersive channels.

Lattice scaling: For $\Lambda = \mathrm{diag}(T, F)$, γ being a Gaussian and C being Gaussian too, it is to expect, that $T/F = \sigma_t/\sigma_f$ ensures the $\min_\Lambda \delta_1(\Lambda)$. Moreover, in terms of the channel coherence one can follow the argumentation given in [LKM04], i.e.

$$\sqrt{C^{(t)}} \leq T \leq \frac{1}{\sqrt{C^{(f)}}} \text{ and } \sqrt{C^{(f)}} \leq F \leq \frac{1}{\sqrt{C^{(t)}}}. \quad \text{(A.3.29)}$$

In summary, the overall scaling rule for the lattice and the pulse according to the channel statistics is:

$$\frac{T}{F} = \frac{\sigma_t}{\sigma_f} = \sqrt{\frac{C^{(t)}}{C^{(f)}}} \qquad \text{(A.3.30)}$$

Appendix B: Further Result Details on Multiple Access

This appendix includes extra details (theorems) regarding the layering concept from chapter 3.

B.1 Layering

- **Soft-Output of ESE**

We consider BPSK modulation. From the view point of user k , the system equation is

$$r(j) = h_k x_k(j) + \underbrace{\sum_{l \neq k} h_l x_l(j) + n(j)}_{\zeta_k(j)} . \qquad \text{(B.1.1)}$$

With respect to central limit theorem, $\zeta_k(j)$ is Gaussian random variable with mean and variance as,

$$\mu_{\zeta,k} = \sum_{l \neq k} h_l E[x_l(j)] \qquad \text{(B.1.2a)}$$

$$\sigma^2_{\zeta,k} = \sum_{l \neq k} h_l^2 \{E[x_l^2(j)] - E[x_l(j)]^2\} + \sigma^2 \qquad \text{(B.1.2b)}$$

The *a posteriori* Log-Likelihood-Ratio (LLR) can be computed as

$$e_{ESE}(x_k(j)) = \log\left\{\frac{p[r(j) \mid x_k(j) = +1, \mathbf{h}]}{p[r(j) \mid x_k(j) = -1, \mathbf{h}]}\right\} = \log\left(\frac{\frac{1}{\sqrt{2\pi\sigma^2_{\zeta,k}}}\exp\left\{-\frac{[r(j) - \mu_{\zeta,k} - h_k]^2}{2\sigma^2_{\zeta,k}}\right\}}{\frac{1}{\sqrt{2\pi\sigma^2_{\zeta,k}}}\exp\left\{-\frac{[r(j) - \mu_{\zeta,k} + h_k]^2}{2\sigma^2_{\zeta,k}}\right\}}\right) \qquad \text{(B.1.3)}$$

$$= \frac{[r(j) - \mu_{\zeta,k} + h_k]^2}{2\sigma^2_{\zeta,k}} - \frac{[r(j) - \mu_{\zeta,k} - h_k]^2}{2\sigma^2_{\zeta,k}} = 2h_k \cdot \frac{r(j) - \mu_{\zeta,k}}{\sigma^2_{\zeta,k}}$$

$$= 2h_k \cdot \frac{r(j) - \{E[r(j)] - h_k E[x_k(j)]\}}{\{E[r^2(j)] - E[r(j)]^2\} - h_k^2\{E[x_k^2(j)] - E[x_k(j)]^2\}}$$

Soft-Input from Decoder (discussed below)

- **Soft-Input of ESE**

The *a priori* Information for user k is

$$\tilde{l}_{ESE}(x_k(j)) = \log\left\{\frac{\Pr[x_k(j)=+1 \mid e_{DEC}(x_k(j))]}{\Pr[x_k(j)=-1 \mid e_{DEC}(x_k(j))]}\right\}. \quad \text{(B.1.4)}$$

Thus, it holds

$$\exp\left\lceil\frac{\tilde{l}_{ESE}(x_k(j))}{2}\right\rceil = \sqrt{\frac{\Pr[x_k(j)=+1 \mid e_{DEC}(x_k(j))]}{\Pr[x_k(j)=-1 \mid e_{DEC}(x_k(j))]}} \quad \text{(B.1.5a)}$$

and

$$\exp\left\lceil-\frac{\tilde{l}_{ESE}(x_k(j))}{2}\right\rceil = \sqrt{\frac{\Pr[x_k(j)=-1 \mid e_{DEC}(x_k(j))]}{\Pr[x_k(j)=+1 \mid e_{DEC}(x_k(j))]}}. \quad \text{(B.1.5b)}$$

Furthermore, it yields,

$$\sinh\left\lceil\frac{\tilde{l}_{ESE}(x_k(j))}{2}\right\rceil = \frac{\exp\left\lceil\frac{\tilde{l}_{ESE}(x_k(j))}{2}\right\rceil - \exp\left\lceil-\frac{\tilde{l}_{ESE}(x_k(j))}{2}\right\rceil}{2} \quad \text{(B.1.6a)}$$

$$= \frac{\Pr[x_k(j)=+1 \mid e_{DEC}(x_k(j))] - \Pr[x_k(j)=-1 \mid e_{DEC}(x_k(j))]}{2\sqrt{\Pr[x_k(j)=+1 \mid e_{DEC}(x_k(j))] \cdot \Pr[x_k(j)=-1 \mid e_{DEC}(x_k(j))]}}$$

and

$$\cosh\left\lceil\frac{\tilde{l}_{ESE}(x_k(j))}{2}\right\rceil = \frac{\exp\left\lceil\frac{\tilde{l}_{ESE}(x_k(j))}{2}\right\rceil + \exp\left\lceil-\frac{\tilde{l}_{ESE}(x_k(j))}{2}\right\rceil}{2} \quad \text{(B.1.6b)}$$

$$= \frac{1}{2\sqrt{\Pr[x_k(j)=+1 \mid e_{DEC}(x_k(j))] \cdot \Pr[x_k(j)=-1 \mid e_{DEC}(x_k(j))]}}.$$

Hence, we obtain

$$E[x_k(j)] = \tanh\left\lceil\frac{\tilde{l}_{ESE}(x_k(j))}{2}\right\rceil = \frac{\sinh\left\lceil\frac{\tilde{l}_{ESE}(x_k(j))}{2}\right\rceil}{\cosh\left\lceil\frac{\tilde{l}_{ESE}(x_k(j))}{2}\right\rceil} \quad \text{(B.1.7)}$$

$$= \Pr[x_k(j)=+1 \mid e_{DEC}(x_k(j))] - \Pr[x_k(j)=-1 \mid e_{DEC}(x_k(j))]$$

$$= \sum_{a=\pm 1} a \Pr[\, x_k(j) = a \mid e_{DEC}\,(x_k(j))] \ .$$

Appendix C: Further Result Details on Reference Scenarios

Appendix C contains additional results and details for the reference scenario chapter 4.

C.1 CoMP and HetNet

C.1.1 Uplink

The time domain UFMC receive signal for *K* users and *M* base station antennas, at the *m*-th antenna for a particular multi-carrier symbol (where we drop the index for the sake of readability) can be written as

$$\mathbf{y}_m = \sum_{k=1}^{K} \mathbf{H}_{mk} \mathbf{\Gamma}_{mk} \mathbf{x}_k + \mathbf{n}_m = \sum_{k=1}^{K} \mathbf{H}_{mk} \mathbf{\Gamma}_{mk} \overline{\mathbf{F}}\,\overline{\mathbf{V}}\,\overline{\mathbf{s}}_k + \mathbf{n}_m \,, \qquad \text{(C.1.1)}$$

where the signal of each user is according to the definitions of equation (2.2.2) in chapter 2.2 for the filters, IDFT and the respective matrix/vector dimensions:

$$\overline{\mathbf{F}} = [\mathbf{F}_1, \mathbf{F}_2, \ldots, \mathbf{F}_B]$$
$$\overline{\mathbf{V}} = diag\,(\mathbf{V}_1, \mathbf{V}_2, \ldots, \mathbf{V}_B)$$
$$\overline{\mathbf{s}} = [\mathbf{s}_1^T, \mathbf{s}_2^T, \ldots, \mathbf{s}_B^T]^T$$

Here $\mathbf{F}_i$ is a Toeplitz matrix with dimension $(N+N_{filter}-1)xN$, composed of the filter impulse response and $\mathbf{V}_i$, being of dimension N x n_i, includes the relevant columns of the inverse Fourier matrix, where the element in *u*-th column and *v*-th row can be expressed as $\mathbf{V}_i(u,v) = \exp(\ j2\pi(u + u_{offset})v \,/\, N)$, in case of adressing the subcarrier indexed $u + u_{offset}$.

The modelling of carrier frequency offset (CFO) is handled in the diagonal matrix $\mathbf{\Gamma}_{mk}$.

The UFMC FIR filter coefficients used in this investigation are length 16 Dolph-Chebyshev-window coefficients. For constructing the filterbank $\overline{\mathbf{F}}$, they are shifted to the center frequency of each PRB. The OFDM signal for comparison uses the same multi-carrier parameters. As OFDM is not using filtering, the filterbank is formed out of identity matrices. A cyclic prefix (CP) is prepended which is discarded in the receiver. The total symbol duration including CP (for OFDM) or filtering (for UFMC), respectively, is the same in both compared signal formats.

In order to write the multiuser signal in pure matrix vector form, with $\mathbf{T}_{mk} = \mathbf{H}_{mk} \mathbf{\Gamma}_{mk} \overline{\mathbf{F}}\,\overline{\mathbf{V}}$, we define:

$$\tilde{\mathbf{T}}_m = [\mathbf{T}_{m1}, \mathbf{T}_{m2}, \ldots, \mathbf{T}_{mK}]$$
$$\tilde{\mathbf{s}} = [\overline{\mathbf{s}}_1^T, \overline{\mathbf{s}}_2^T, \ldots, \overline{\mathbf{s}}_B^T]^T \qquad \text{(C.1.2)}$$

The signal from (C.1.1) thus can be rewritten, using the stacked variables (C1.1.2), as

$$\mathbf{y}_m = \tilde{\mathbf{T}}_m \tilde{\mathbf{s}} + \mathbf{n}_m \ . \qquad \text{(C.1.3)}$$

In order to write one receive vector for all the distributed receive antennas, we further define:

$$\breve{\mathbf{y}} = [\mathbf{y}_1^T, \mathbf{y}_2^T, \ldots, \mathbf{y}_m^T]^T$$
$$\breve{\mathbf{T}} = [\tilde{\mathbf{T}}_1^T, \tilde{\mathbf{T}}_2^T, \ldots, \tilde{\mathbf{T}}_M^T]^T \quad \text{(C.1.4)}$$
$$\breve{\mathbf{n}} = [\breve{\mathbf{n}}_1^T, \breve{\mathbf{n}}_2^T, \ldots, \breve{\mathbf{n}}_B^T]^T$$

This leads to the composite multiuser multi-cell signal vector

$$\breve{\mathbf{y}} = \breve{\mathbf{T}}\breve{\mathbf{s}} + \breve{\mathbf{n}}. \quad \text{(C.1.5)}$$

In order to obtain the multiuser symbol estimate vector $\hat{\breve{\mathbf{s}}}$, we apply a linear receiver $\hat{\breve{\mathbf{s}}} = \mathbf{W}_{\text{CoMP}}\breve{\mathbf{y}}$, which deals with all multiuser and inter-carrier interference across all the distributed antennas of the coordinated cell set.

In our considered investigation scenario, a zero forcer was used with

$$\mathbf{W}_{\text{CoMP}} = \breve{\mathbf{T}}^{+}, \quad \text{(C.1.6)}$$

applying the Moore-Penrose-pseudo-inverse. In the simulations of chapter 4.1, the channel knowledge $\mathbf{H}_{mk}$ was assumed to be perfect, while the carrier-frequency offset contained in $\mathbf{\Gamma}_{mk}$ was either perfectly known, unknown or known with a relative frequency offset mismatch of 10%.

C.1.2 Downlink

The system model for Multi-User transmission with FBMC is presented in this section. It is here supposed that the BSs and the UEs are synchronized in time and in frequency (see section 4.1).

C.1.2.1 System model for Multi-User transmission

Figure C.1.1 details the system model for Multi-User transmission based on Figure 4.1.1 (left hand side). Cooperation between two sectors of two adjacent tri-sectored cells is considered. The BSs are equipped with N_T transmit antennas while the UEs have a single receive antenna. The dotted arrows represent the BSs array broadsides. Grey, red and blue circles represent UEs at cell edge that are likely to be scheduled for MU CoMP transmission.

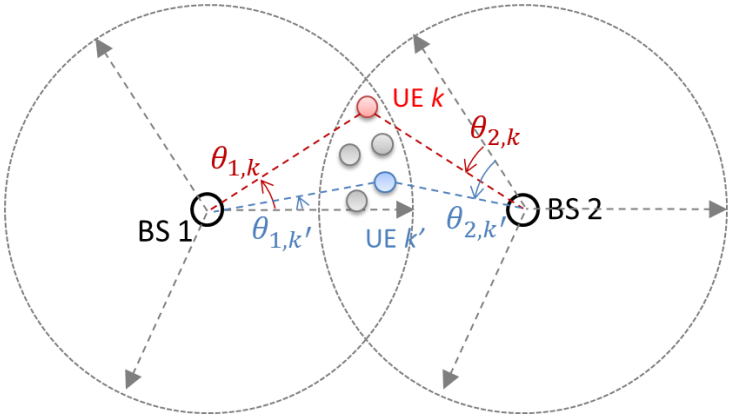

Figure C.1.1. System model for Multi-User transmission

$\mathbf{H}_{r,k} \in \mathbb{C}^{N_T \times L}$ is the channel response for UE k on RB r, with L the number of carriers in a RB, $\mathbf{h}_{r,k}(f) \in \mathbb{C}^{N_T \times 1}$ is the channel response for UE k on carrier f of RB r. The channel considered here is the equivalent channel described in section 4.1 by:

$$h_{eq,j}(t) = h_{1j}(t) + h_{2j}(t - \tau) \quad \text{(C1.1.1)}$$

The proposed algorithms operate independently on each RB, in the following the subscript r is then dropped.

To get to a MU transmission between both BSs and two UEs, weight vectors are applied at the transmitters. In this study the weights are to be chosen in a finite set of 2^{N_T} vectors (the codewords) named the codebook. Codebooks for $N_T = 2$ and $N_T = 4$ can be found in section C1.3. Codebooks are further divided into N_T Unitary Codebooks (UCs) composed of $2^{N_T}/N_T$ codewords each. Figures C.1.2 and C.1.3 show the beams of UCs 1 and 2 for $N_T = 4$ and $N_T = 2$ respectively; the BS array broadside is the horizontal line passing through the point '0'.

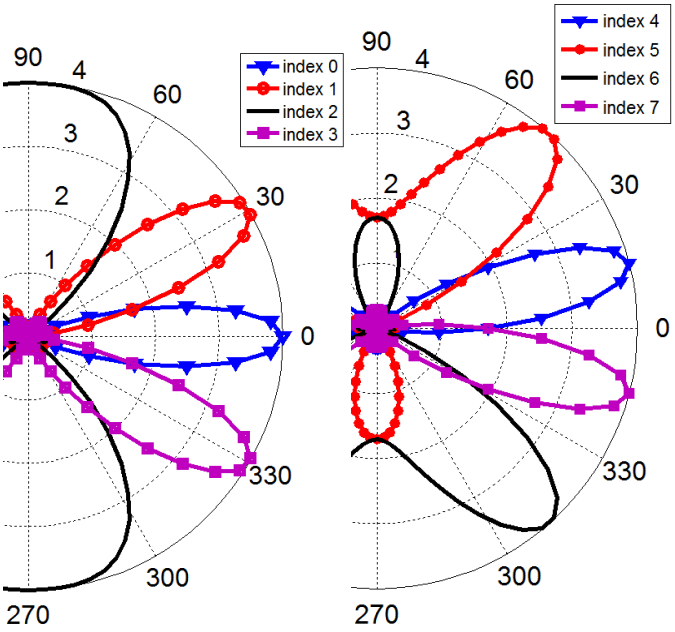

Figure C.1.2. Beams of unitary codebooks 1 and 2 for $N_T = 4$.

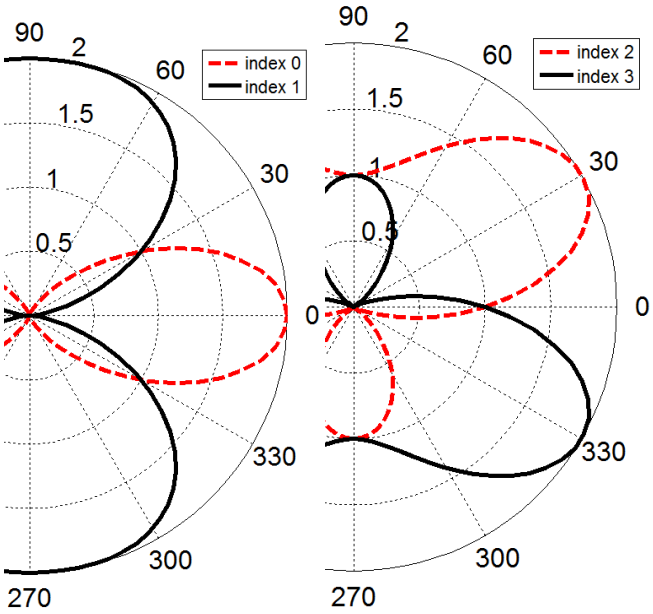

Figure C.1.3. Beams of unitary codebooks 1 and 2 for $N_T = 2$.

$\mathbf{w}_{u,i} \in \mathbb{C}^{N_T \times 1}, u \in S_{UC}, i \in \{1,2,\dots,2^{N_T}/N_T\}$, is the weight vector of index i chosen in the UC u. S_{UC} is the set of UCs that are allowed for feedback and transmission. Note that the same weights are applied on all the carriers of the RB.

C.1.2.2 Channel model

The channel used for this study is the Spatial Channel Model Extended (SCME) [SGS+05]. SCME allows defining multiple links, between multiple BSs and a UE: the channel between the two BSs and one UE is described by Figure C.1.4. The detailed channel model between one BS and one UE is described by Figure C.1.5.

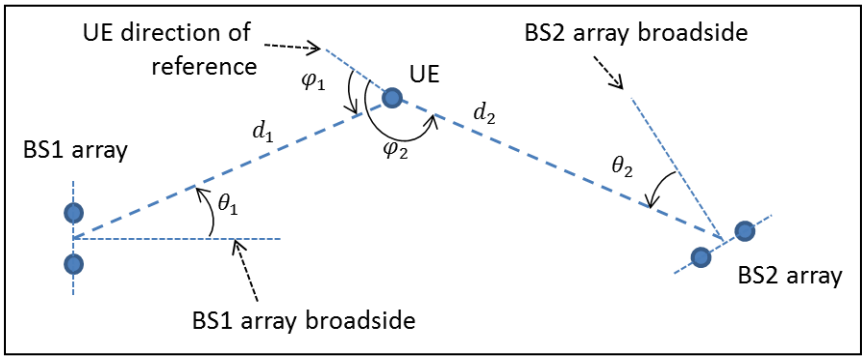

Figure C.1.4. Multiple link SCME channel model

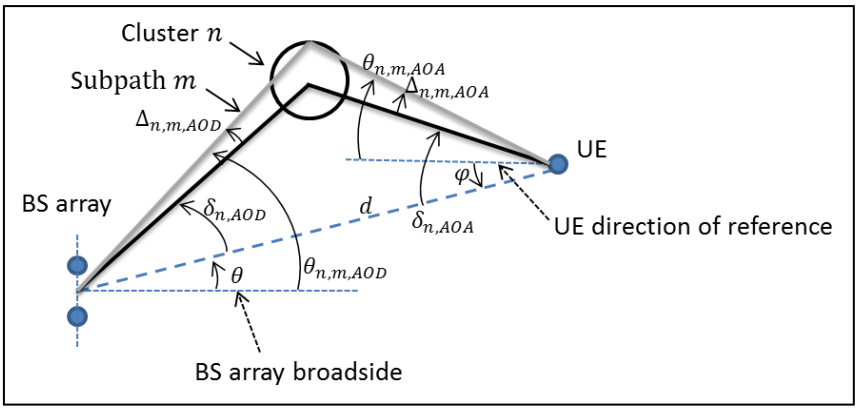

Figure C.1.5. SCME channel model for one link

UEs likely to be scheduled for MU-CoMP transmission from BS1 and BS2 are uniformly distributed at the edge of cells BS1 and BS2: the black area on Figure C.1.6 shows the possible positions of UEs. It is assumed in the following that each UE k has perfect knowledge of the channel $\mathbf{H}_{r,k}$ on all the RBs r.

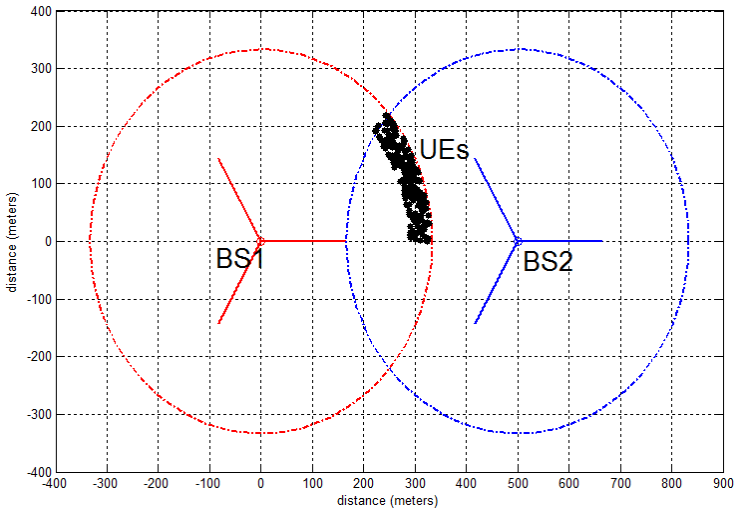

Figure C.1.6. Distribution of UEs likely to be scheduled for MU-CoMP transmission

C.1.2.3 Performance evaluation

In the next deliverables, the performance of the system will be assessed in terms of achievable rate of the UEs scheduled in MU-CoMP. The amount of bits necessary for the feedback will be measured so as the influence on the performance of the feedback delay. Several speeds for the UEs will be considered.

C.1.2.4 Codebooks

Table C.1.2.1 codebook for two transmit antennas

Index	0	1	2	3
Codeword	$\frac{1}{\sqrt{2}}\begin{bmatrix}1\\1\end{bmatrix}$	$\frac{1}{\sqrt{2}}\begin{bmatrix}1\\-1\end{bmatrix}$	$\frac{1}{\sqrt{2}}\begin{bmatrix}1\\j\end{bmatrix}$	$\frac{1}{\sqrt{2}}\begin{bmatrix}1\\-j\end{bmatrix}$

Table C.1.3. codebook for four transmit antennas

Index	0	1	2	3
Codeword	$\frac{1}{2}\begin{bmatrix}1\\1\\1\\1\end{bmatrix}$	$\frac{1}{2}\begin{bmatrix}1\\j\\-1\\-j\end{bmatrix}$	$\frac{1}{2}\begin{bmatrix}1\\-1\\1\\-1\end{bmatrix}$	$\frac{1}{2}\begin{bmatrix}1\\-j\\-1\\j\end{bmatrix}$
Index	4	5	6	7
Codeword	$\frac{1}{2}\begin{bmatrix}1\\(1+j)/\sqrt{2}\\j\\(-1+j)/\sqrt{2}\end{bmatrix}$	$\frac{1}{2}\begin{bmatrix}1\\(-1+j)/\sqrt{2}\\-j\\(1+j)/\sqrt{2}\end{bmatrix}$	$\frac{1}{2}\begin{bmatrix}1\\(-1-j)/\sqrt{2}\\j\\(1-j)/\sqrt{2}\end{bmatrix}$	$\frac{1}{2}\begin{bmatrix}1\\(1-j)/\sqrt{2}\\-j\\(-1-j)/\sqrt{2}\end{bmatrix}$
Index	8	9	10	11

Codeword	$\frac{1}{2}\begin{bmatrix}1\\1\\-1\\-1\end{bmatrix}$	$\frac{1}{2}\begin{bmatrix}1\\j\\1\\j\end{bmatrix}$	$\frac{1}{2}\begin{bmatrix}1\\-1\\-1\\1\end{bmatrix}$	$\frac{1}{2}\begin{bmatrix}1\\-j\\1\\-j\end{bmatrix}$
Index	12	13	14	15
Codeword	$\frac{1}{2}\begin{bmatrix}1\\1\\1\\-1\end{bmatrix}$	$\frac{1}{2}\begin{bmatrix}1\\1\\-1\\1\end{bmatrix}$	$\frac{1}{2}\begin{bmatrix}1\\-1\\1\\1\end{bmatrix}$	$\frac{1}{2}\begin{bmatrix}1\\-1\\-1\\-1\end{bmatrix}$

C.2 MTC and Tactile Internet

C.2.1 BER performance and Out of band radiation

To generate the GFDM transmit signal, complex-valued data symbols are distributed on a grid that spans across several time slots a subcarriers, thus yielding a two dimensional block structure. Each subcarrier is pulse shaped with an adjustable filter. So far, the root raised cosine filter with small roll-off factors has proven to provide good performance. Further, the pulse shaping filter is circular, thus the tail biting technique is applied when digitally convolving the data symbol with filter samples. The circularity allows avoiding filtered tails that ultimately reduce the spectral efficiency of the system. The individual subcarriers are first modulated with a respective subcarrier frequency and then super positioned. One cyclic prefix is used per block to enable simple frequency domain channel equalization at the receiver. Note that when one block spans over several time slots, only one CP is used.

An overall model for the signal generation is given by $\mathbf{x}=\mathbf{Ad}$, where $\mathbf{d}$ denotes a vector containing the complex valued data symbols, $\mathbf{A}$ is a modulation matrix that is constructed from the samples of the pulse shaping filter and the parameters of the block size and $\mathbf{x}$ is a vector containing the transmit signal time samples.

From this basic model, three standard ways of receiving the signal follow:

- Matched filter (MF) $\mathbf{d}_{MF}=\mathbf{A}^H\mathbf{y}$
- Zero forcing (ZF) $\mathbf{d}_{ZF}=\mathbf{A}^+\mathbf{y}$
- Minimum mean square error (MMSE) $\mathbf{d}_{MMSE}=\mathbf{A}^+\mathbf{y}$ with $\mathbf{A}^+=((\sigma_n^2/\sigma_d^2)\mathbf{I}+\mathbf{A}^H\mathbf{A})^{-1}\mathbf{A}^H$ and variance of the noise samples σ_n^2, variance of the data symbols σ_d^2 and identity matrix $\mathbf{I}$

Due to the previous introduced flexible pulse shaping which can reduce out of band radiation, in GFDM the subcarriers are not necessarily orthogonal. This leads to cross-talk between time slots and subcarriers and produces self-created interference, even in the absence of a multipath channel. The performance of the different methods to receive the signal is compared in Figure C.2.1 where uncoded BER for AWGN channels is depicted (note that *K* is the number of subcarriers, *M* the number of symbols per subcarrier and *a* the roll-off factor)

The conventional matched filter approach yield strong deviation from the OFDM BER curve, particularly for high SNR where the impact of the noise shrinks while the self-interference remains.

The zero forcer performs better than the matched filter, especially for high SNRs. However there is still a gap between the ZF the OFDM curve which is due to the inherent noise enhancement of that receiver scheme. Finally, the MMSE provides a balance between variance of the data symbols and the variance of the noise, yielding the performance, at the cost of highest computational complexity. Note that the MF and ZF receiver are computed once and do not have to be adjusted according to the current SNR.

Finally, a fourth way of receiving the signal is constituted by an enhancement of the matched filter receiver: By adding an iterative interference cancellation scheme at the receiver, the mutual cross-talk within a GFDM block can be mitigated such that the MF performance matches with the OFDM curve.

Note that, as can be seen in Figure C.2.2 the performance degradation of GFDM is highly dependent on the pulse shaping filter that is used.

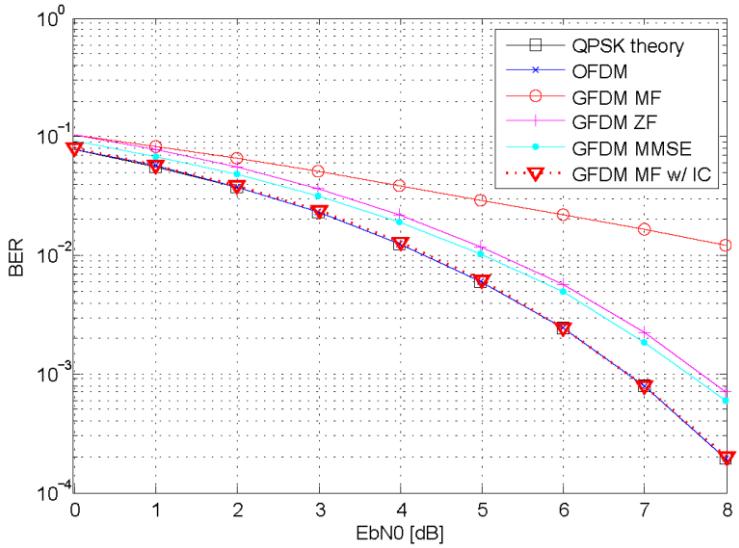

Figure C.2.1: AWGN, uncoded, K=128, M=5, a=0.5

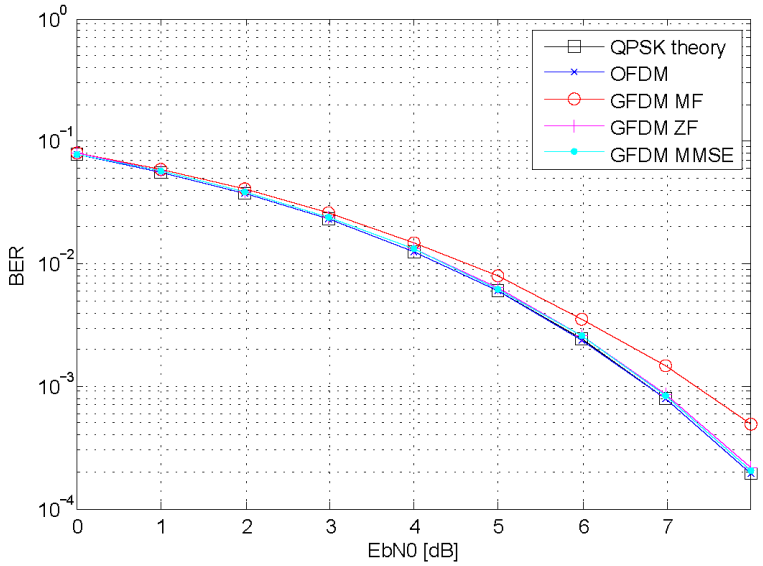

Figure C.2.2: AWGN, uncoded, K=128, M=5, a=0.1

In case of Rayleigh multipath fading the behavior of the three receivers is similar, as can be seen in Figure C.2.3 and Figure C.2.4. Note that one significant advantage of GFDM over OFDM is the reduced amount of cyclic prefix. By prefixing one block instead of each symbol, the amount of redundancy in GFDM scales with the block size. This directly influences the energy required to transmit one bit and is particularly evident in the curves in Figure C.2.3. Thus, when the pulse shaping filter is such that it keeps self-interference low, GFDM can outperform OFDM. Assuming the CP is as long as 25% of a symbol, the gain is roughly 1dB.

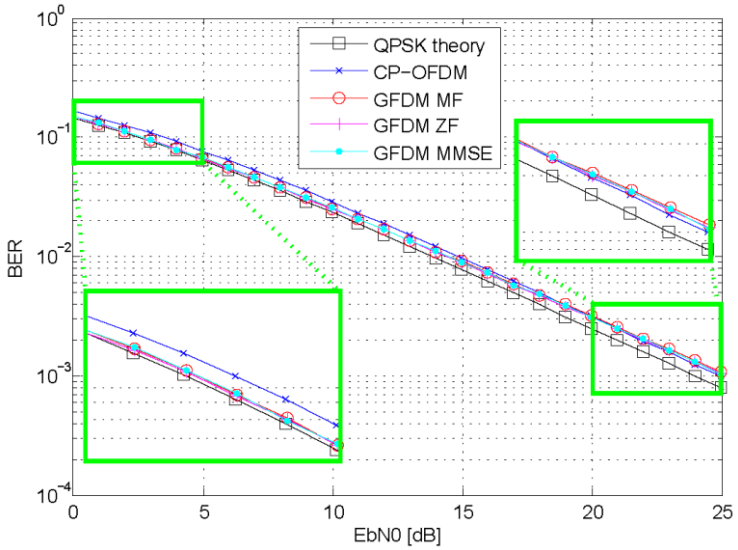

Figure C.2.3: Rayleigh channel, uncoded, K=128, M=5, a=0.1

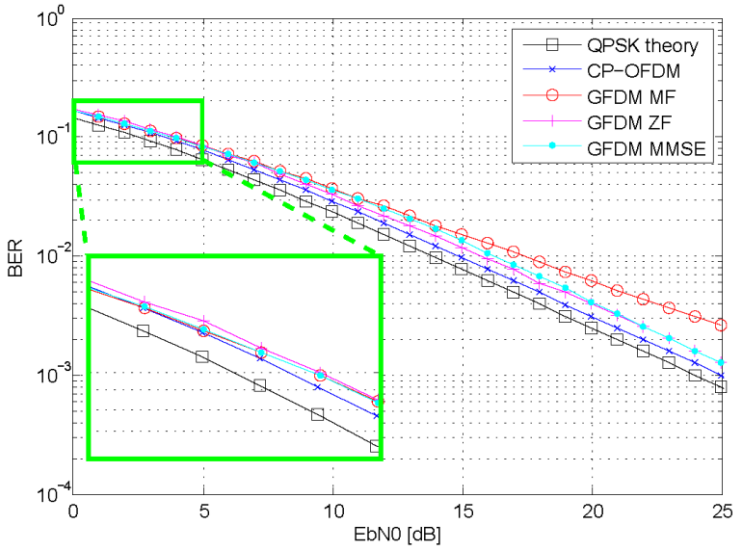

Figure C.2.4: Rayleigh channel, uncoded, K=128, M=5, a=0.5

While the self-induced interference in GFDM is certainly not an attractive feature, it is an issue that does not impact the LTE primary system. In fact, by accepting the self-interference, flexible pulse shaping is enabled at the same time, which is highly desirable. Also, as discussed above, by choosing appropriate filter parameters and/or employing an interference cancellation scheme, the BER degradation can be eliminated without losing the pulse shaping.

The power spectral density of a GFDM and an OFDM signal are compared in Figure C.2.5, assuming the same sampling time for both signal. For GFDM, a RRC filter with roll-off factor 0.1 is used. It becomes clearly evident, that due to the better spectral localization of GFDM, it provides less interference to the primary system than an asynchronous OFDM secondary system. Figure C.2.6 depicts the same signal as it is measured with a spectrum analyzer after transmission through a real AWGN channel.

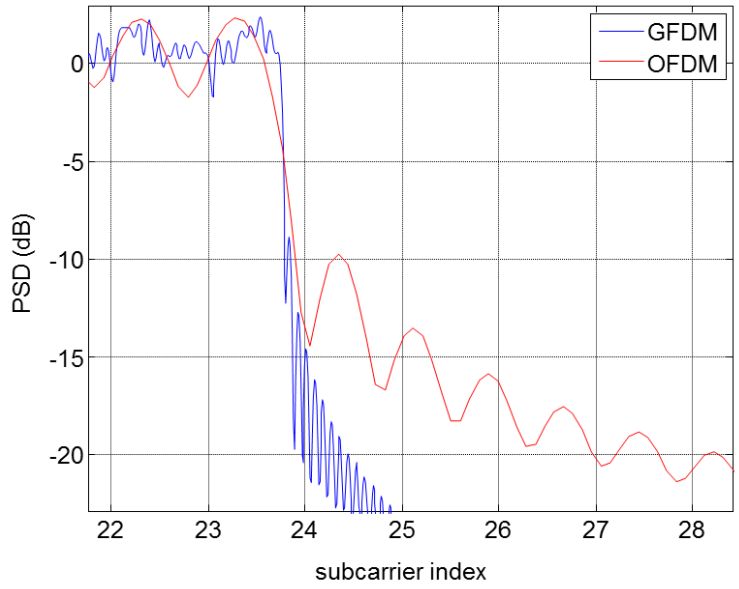

Figure C.2.5: Simulated PSD of OFDM and GFDM with block size of 32 subcarriers and 5 time slots and a RRC filter with roll-off 0.1

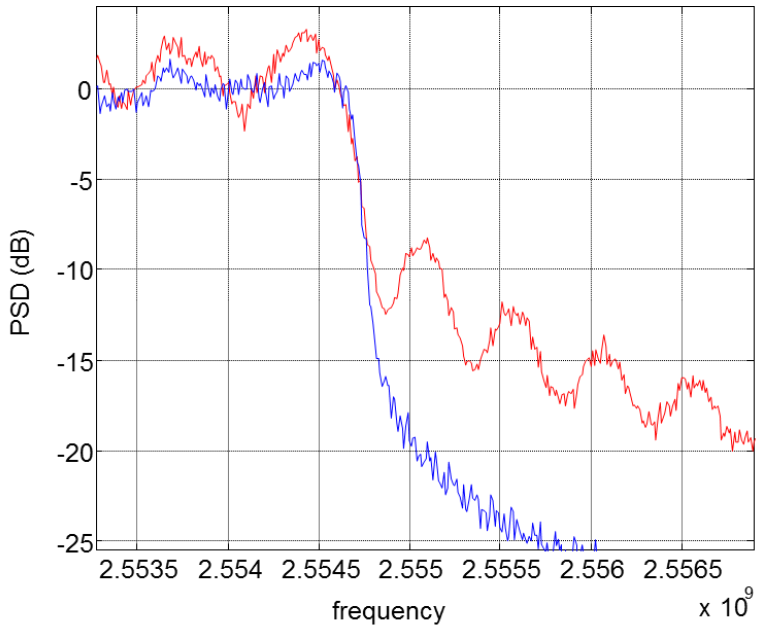

Figure C.2.6: Measured PSD of OFDM and GFDM with block size of 32 subcarriers and 5 time slots and a RRC filter with roll-off 0.1

C.2.2 Opportunistic use of spectrum

In order to investigate out-of-band leakage of OFDM and GFDM, an OFDM primary system is considered. First, a white space is artificially created in within the bandwidth of the primary system by silencing a given number of subcarriers. Then, an asynchronous secondary system is inserted into

the whitespace according to Figure C.2.7. Two setups are investigated: In Setup 1, OFDM was used as a secondary system, while in Setup 2 a GFDM secondary system was employed.

The results shown in Figure C.2.8 have been obtained through simulation of uncoded bit error rate performance under AWGN conditions and with QPSK modulation. A total bandwidth of 64 subcarriers was considered, where 2/3 were assigned to the primary system and 1/3 was assigned to the secondary system. One subcarrier was left silent as a guard band on each side. The GFDM system employed an RRC pulse shaping filter with roll-off factor 0.25 and filter length of 11 symbols.

The conclusion that can be drawn is that while the secondary GFDM system performs worse in Setup 2 than the secondary OFDM system in Setup 1, GFDM offers a better protection to the primary system.

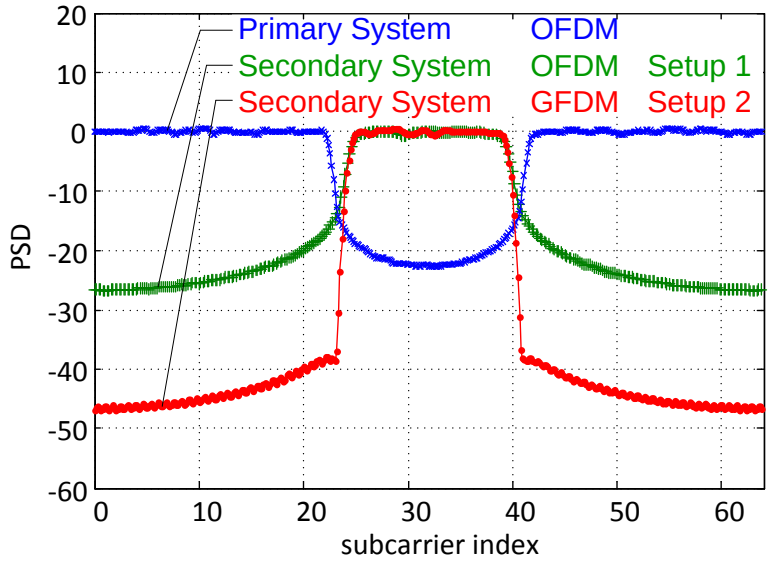

Figure C.2.7: Power spectral density of primary and secondary system from Setup 1 and Setup 2.

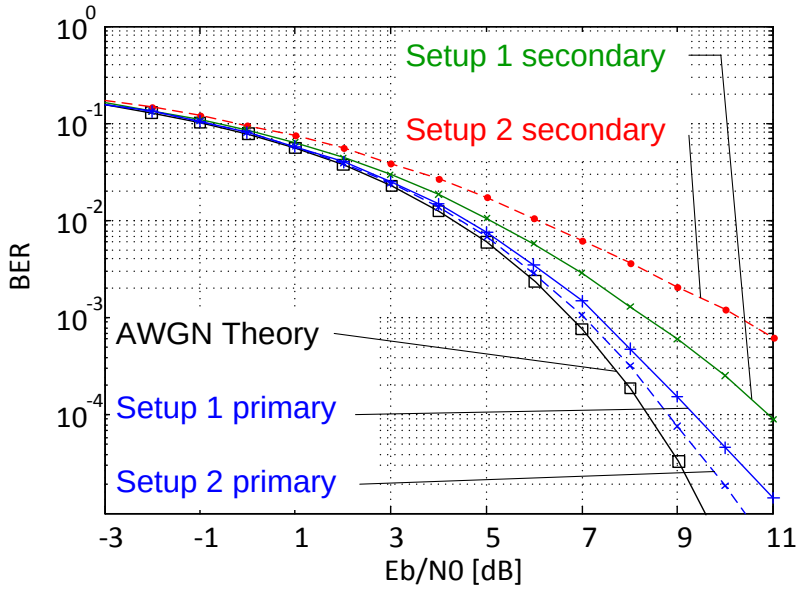

Figure C.2.8: Bit Error Rate performance of primary and secondary system from Setup 1 and Setup 2

C.2.3 Low Complex implementation of the transmitter

The method described in this section is based on [MGKLF12]. Considering a GFDM system, the transmitted data symbols on every subcarrier undergo three processing steps:

- upsampling
- pulse shaping
- upconversion.

These operations are inherently accounted for in the modulation matrix A. As can be seen in Figure C.2.9, **A** contains the pulse shape in all possible phase offsets and frequencies. This however is a very redundant approach and thus subject to further optimization. By carrying over the subcarrier processing from time domain to frequency domain, significant savings can be achieved.
Upsampling a signal in time domain by factor N basically denotes the operation of inserting N-1 zeros for every original sample. The downside of doing this is that the size of the original vector is increased, thus all subsequent operations need to be performed on a factor N times larger vector. But inserting zeros in time domain can be represented in frequency domain by a simple N times repetition of the Fourier transform of the original signal. Thus in the discrete case a small FFT is enough to contain all information.

Further, filtering the individual subcarriers in a GFDM system corresponds to a convolution of a vector containing upsampled data symbols and a vector containing the time samples of the pulse's shape. Convolution is a computationally heavy operation and carrying this over to frequency domain, it can be substituted by a simple elementwise multiplication of the FFT of the data symbols and the FFT of the filter pulse. Note that for this to hold, the pulse needs to be applied in a circular, tail biting manner [FKB09].

The third operation, the upconversion, is performed in time domain by multiplying the samples of the pulse-shaped subcarrier signals with complex valued oscillations of different frequencies. In frequency domain, this multiplication is replaced by a convolution of the FFT of the pulse shaped subcarrier samples and a Dirac function. This convolution results in a simple, circular shift which can be easily implemented as a pointer operation on a register. Note that the operations described in this paragraph are illustrated in Figure C.2.10.

As a result, the GFDM transmitter shown in Figure C.2.12 can be derived, wherein the red blocks denote upsampling, filtering and upconversion in frequency domain. Comparing this with OFDM, the relation between both becomes evident: setting the parameter M=1 and omitting the processing steps denoted by the red blocks leads turns GFDM into OFDM. Comparing GFDM to the scheme that is used in the LTE uplink standard from Figure C.2.11, namely DFT spreading, the number of common processing blocks is even larger. As a conclusion, GFDM can be therefore seen as a generalization of the two other multicarrier transmission methods.

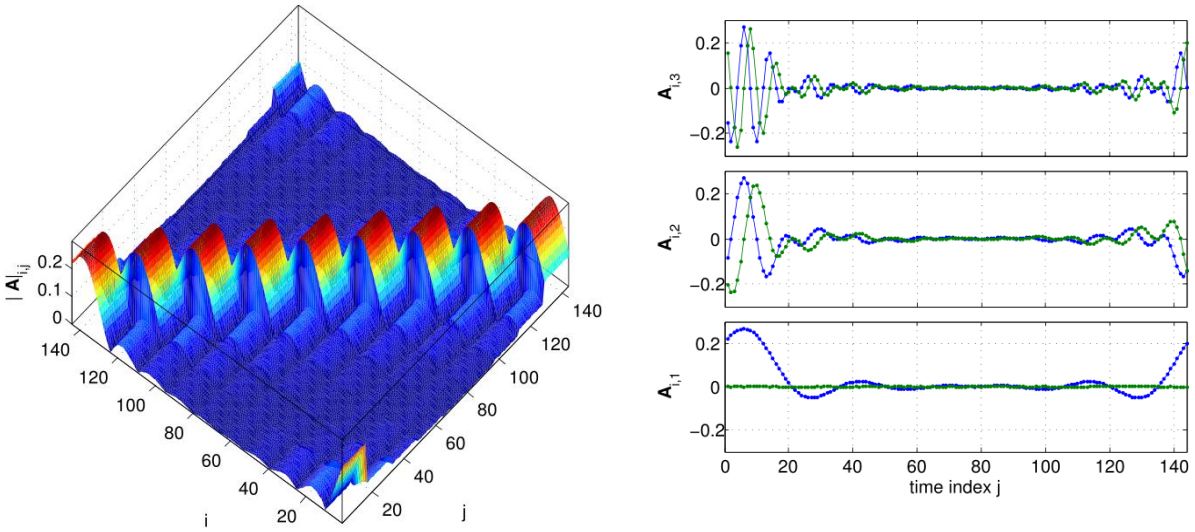

Figure C.2.9: Absolute value of the entries of an example modulation matrix A (left) and real and imaginary part of the first three rows of A (right).

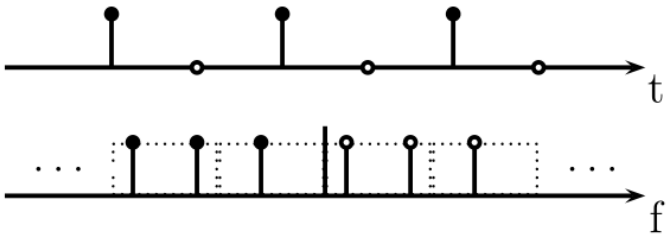

(a) Upsampling in time and frequency domain

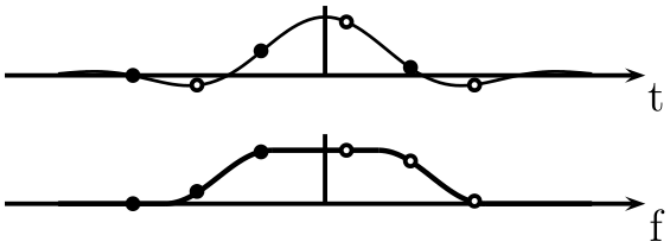

(b) Pulse shaping filter in time and frequency domain

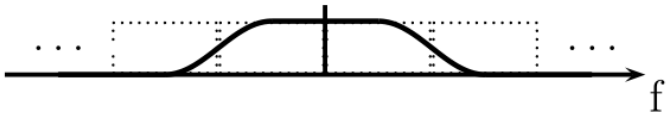

(c) Filtering in frequency domain

Figure C.2.10: Illustration of the operations involved in the modulation of GFDM signal for both time and frequency domain

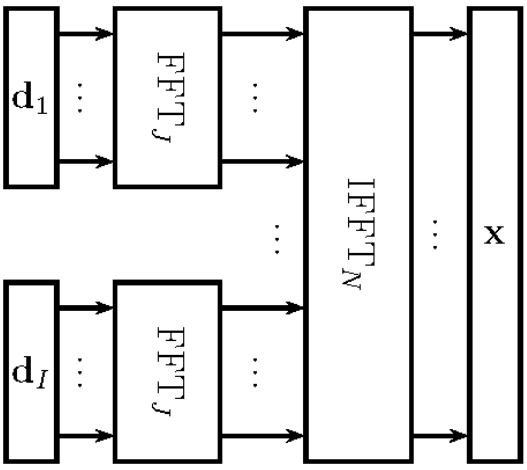

Figure C.2.11: DFT-spreading transmitter model

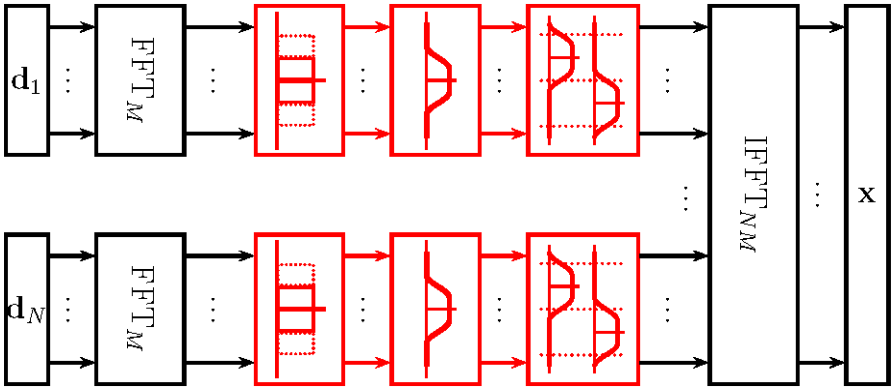

Figure C.2.12: GFDM transmitter model

Carrying out certain processing steps in frequency domain enables savings computational complexity. Particularly, the upsampling and the upconversion can be carried out through pointer/memory operations as previously described. This leaves three steps that contribute to the total number of multiplications that are necessary to generate the transmit signal. Assuming that an FFT/IFFT operation of N points can be performed at the cost of N log2 N multiplications, the GFDM frequency domain approach requires:

- K times M log2 M multiplications for the M point FFTs of K subcarriers,
- K times LM multiplications for the filtering of K subcarriers,
- NM log2 NM multiplications for the NM point IFFT.

Thus the total complexity is $C_{GFDM,FFT}$ = KM log2 M + KLM + NM log2 NM. Therein, N gives the total number of subcarriers in the system, K gives the number of active subcarriers in the system and L gives how many neighboring subcarriers are overlapping (thus L=2 for the RC/RRC case).

As a comparison, taking the approach of the modulation matrix described in [MGKLF12] leads to $C_{GFDM,A}$ = NKM^2 and since K is typically a number in the same order of magnitude as N, that means nearly quadratic growth. Lastly, OFDM complexity is C_{OFDM} = M N log2 N and $C_{DFT\text{-}spread}$ = M I J log2 J + M N log2 N. Note that in relation to the LTE standard, J = 12 and I = 100.

The resulting complexity can be observed in Figure C.2.13. While the LTE UL and DL are denoted by the two blue curves respectively, the analysis shows that GFDM (red curves) can achieve a

complexity in the same order of magnitude by shifting the transmitter processing to the frequency domain. However, there is a big margin and the computational effort is highly depending on the parameter L, which denotes how many neighboring subcarriers overlap. A small L is desirable because it keeps the interference between neighboring subcarriers limited to one neighbor. An L>1 is necessary, because in order to achieve narrowband subcarriers, the filtering pulse needs to be allowed to spread over a certain amount of time. Finally, the GFDM approach with the modulation matrix yields the highest computational effort (black curve).

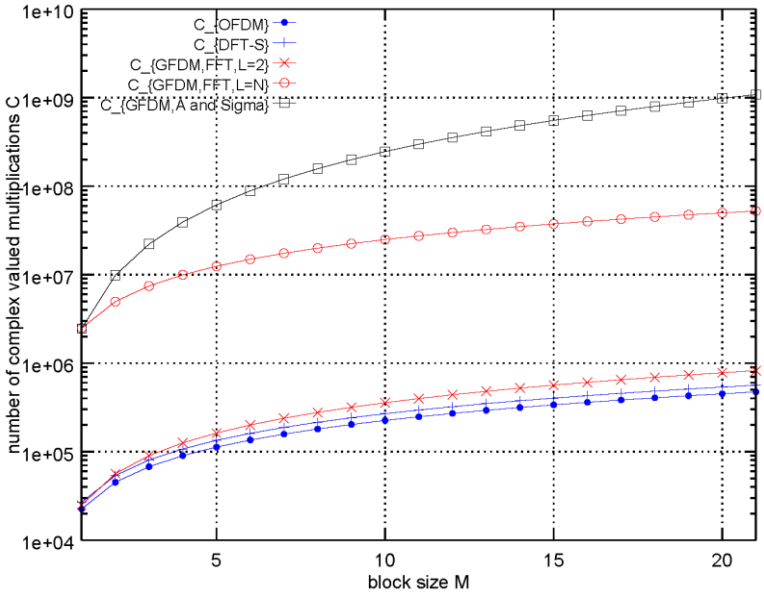

Figure C.2.13: Computational complexity of the transmitter of different modulation schemes and implementation approaches as a function of the block size denoted by M

C.2.3 PAPR aspects

Peak-to-average power ratio (PAPR) is a key parameter that influences the energy efficiency and is particularly relevant for cheap mass market terminals. For instance the most recent cellular standard, Long Term Evolution, uses different waveforms in downlink and uplink transmission, to address the issue of nonlinear distortions as a consequence of high PAPR. High PAPR means that linear amplifiers with large input back off need to be used, in order to avoid distortions in the transmitted signal, otherwise bit error rates of the transmission can increase and strong out-of-band radiation may be introduced. The input back off is especially relevant for the battery lifetime of mobile terminals, as it impacts the energy consumption of a device, while another issue is heat dissipation of the circuitry. So a good PAPR can easy the deployment of cheap terminals that require little maintenance and a battery lifetime of several years for mass market of MTC.

The PAPR of GFDM with multiple subcarriers predictably follows the theorem of the central limit, exhibiting a Gaussian CCDF (Complimentary Cumulative Density Function) plot as seen in Figure C.2.14.

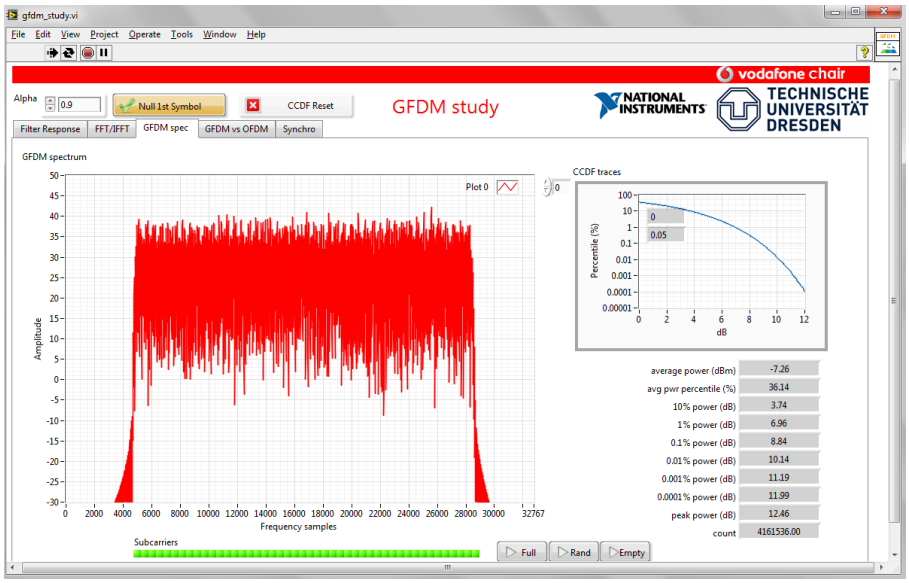

Figure C.2.14: GFDM with multiple subcarriers study using LabView platform

But individually each subcarrier follows a single carrier CCDF curve, keeping the exploration of multiple accesses attractive for power limited devices in the uplink side, Figure C.2.15. The PAPR per subcarrier can easily be controlled using the roll off parameter of the pulse shaping.

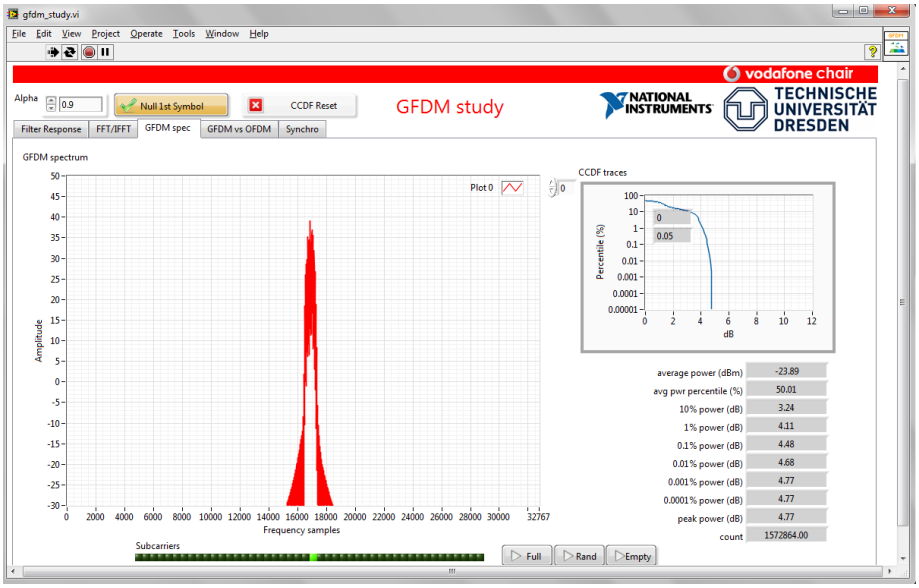

Figure C.2.15: GFDM with single subcarriers study using LabView platform

C.2.4 Packet transmission with FBMC

In packet transmission, the impulse response of the prototype filter imposes signal transition at the beginning and at the end of the packet, which increases the overall duration of the emitted signal (Figure C.2.16). If the prototype filter is of length duration L and the ratio $K=L/M$, K is called the overlapping factor as it is the number of multicarrier FBMC symbols which overlap in the time domain. The authors of [PHY08a] proposed extensive study on the design of the prototype filter. A proposed set of filter coefficient as a function of K is given in Table C.2.1.

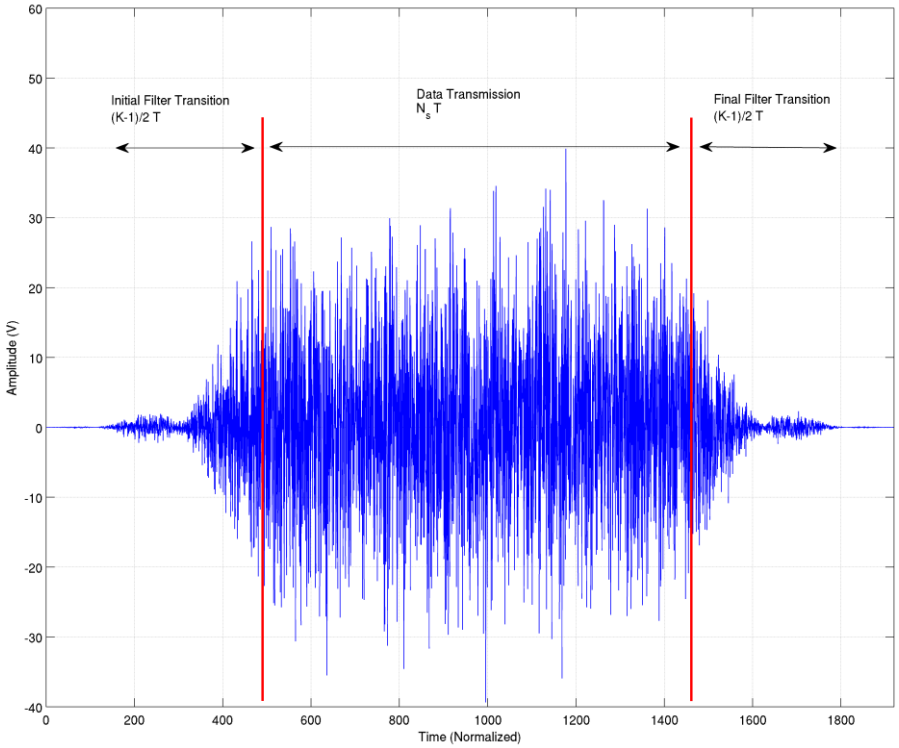

Figure C.2.16: FBMC OQAM filter transitions (packet transmission mode)

Table C.2.1. Frequency Domain Prototype filter Coefficients

Overlapping Factor K	H_0	H_1	H_2	H_3
2	1	$\sqrt{2}/2$	-	-
3	1	0.911438	0.411438	-
4	1	0.971960	$\sqrt{2}/2$	0.235147

The impulse response, $h(t)$, of the filter is given by the inverse Fourier transform of the frequency domain filter coefficients.

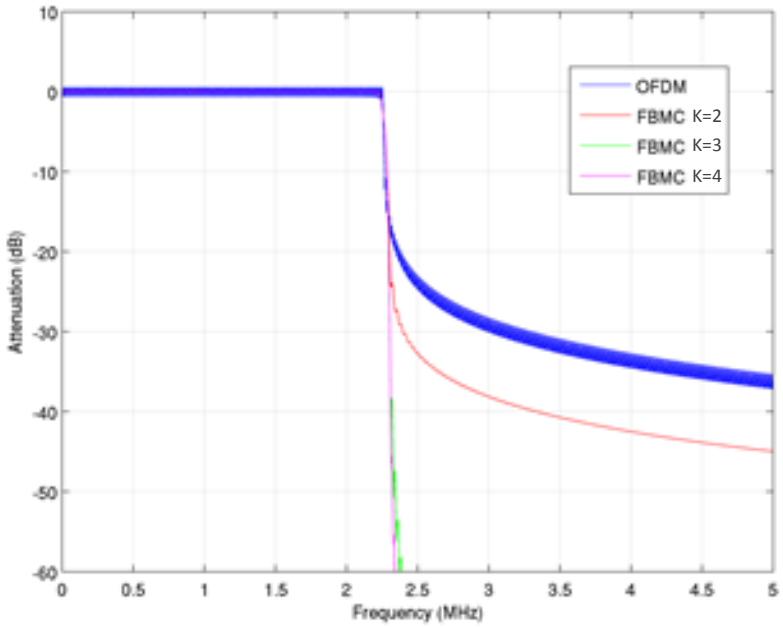

Figure C.2.17: Frequency response comparison, OFDM vs FBMC for various prototype filters (*K=2* to *4*)

A comparison of the theoretical power spectrum density of OFDM and FBMC/OQAM for various values of overlapping factor K is given in Figure C.2.17. The parameters of the 5MHz bandwidth LTE configuration have been used.

If N_s multicarrier symbols have to be transmitted, the multicarrier symbol duration is equal to T, K is the overlapping factor, and CP the OFDM cyclic prefix relative duration, then the burst durations for OQAM/FBMC and for OFDM are given by:

$$D_{FBMC} = \left(N_S + K - \frac{1}{2}\right)T$$
$$D_{OFDM} = \left(N_S(1 + CP)\right)T \qquad \text{(C.2.1)}$$

Therefore, the penalty of using FBMC is equal to $(K\text{-}1/2\text{-}Ns.CP)T$. Depending on the number of transmitted multicarrier symbols, when using FBMC/OQAM, burst duration is longer or shorter than when using OFDM. Table C.2.2 gives the number of multicarrier (OFDM or FBMC) symbols using LTE parameters [LTE10] for which FBMC/OQAM pulse duration starts to be shorter than OFDM pulse duration. When choosing $K=4$ and transmitting $N_s=16$ multicarrier symbols, the pulse duration is 13.9% longer for FBMC/OQAM than for OFDM. With this specific configuration, this makes the waveform less adapted to short pulse duration.

Table C.2.2. Burst duration, FBMC vs. OFDM, LTE parameters

Channel Bandwidth (MHz)	1.4	3	5	10	15	20
FFT Size	128	256	512	1024	1536	2048
Guard Interval	9	18	36	72	108	144

N_s, $D_{FBMC}<D_{OFDM}$ $(K=4)$	50
N_s, $D_{FBMC}<D_{OFDM}$ $(K=3)$	36
N_s, $D_{FBMC}<D_{OFDM}$ $(K=2)$	22
Percentage burst duration for short burst ($Ns = 16$, $K=4$)	13.9 %

However, in order to reduce pulse duration for FBMC/OQAM, [BEL10] analyzed the impact of shortening the pulse duration and concluded that the transmitted burst with Ns symbols may be shortened by up to $(Ns+1/2)T$ with a minor impact on the performance. The order of pulse duration between OFDM and FBMC for short pulses of 16 multicarrier symbols becomes then more favorable to FBMC. Nevertheless a temporal spectrum leakage is introduced as a result of the burst cutting. [PHY08b] investigated a mechanism based on pulse windowing using a Raised Cosine window in order to reduce burst duration while controlling spectrum regrowth. By allowing 1.125 extra OQAM/FBMC symbols (288 out of 512 for the start of the burst and the same for the end of the burst) instead of 3.5 symbols when $K = 4$, out of band leakage may be contained below $50\ dBc$ at any time from the first out-of-band carrier. With these hypothesis, symbol durations are almost the same between OFDM and FBMC/OQAM for $N_s=16$ (17.125 symbols for FBMC/OQAM versus 17.152 for OFDM).

C.3 Fragmented Spectrum

The use of fragmented spectrum is not without any impact on the physical layer algorithms and particularly on the channel estimation process. As an example, the channel state information (CSI) is usually unknown at the receiver side and needs to be efficiently estimated. The most common scheme for multicarrier waveform is the pilot assisted method. A known data sequence is sent through the channel, and at the receiver side, the CSI is estimated based on this data sequence. All the techniques suffer from the "border effect" phenomenon which degrades significantly the overall performance and leads to an error floor. The main cause of border effect comes from the channel estimation at the border of the spectrum which is less reliable. An interesting example is discussed in [DL07]. In case of fragmented spectrum and small resource blocks, the border effect on the channel estimation performance may lead to significant performance degradation. The border effect phenomenon is amplified in case of non-continuous pilots on the resource block.

In order to illustrate the border effect we designed a simple de-noising filter based on the classical FFT interpolation algorithm as suggested in [DL07]. We computed the Relative Mean Square Error (MSE) on the channel estimation. A resource block of 336 carriers is considered (FFT size is equal to 1024). We assumed that a Least Square (LS) estimation of the CSI was performed on contiguous pilots. The de-noising filter has been optimized for channel duration of FFT/8 (128 samples)[1].

[1] The optimized filter is a 336 taps complex filter. This filter is not presented as an example and may not be suitable for a practical implementation.

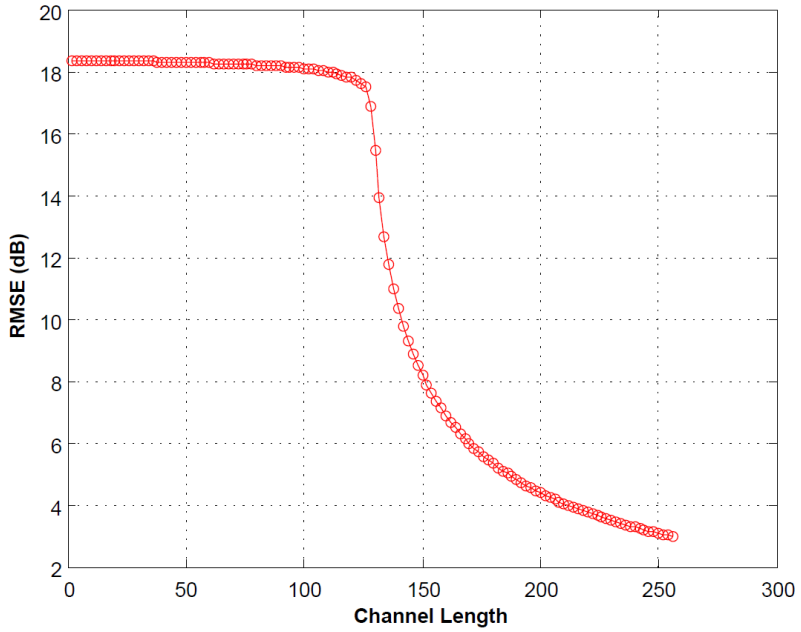

Figure 4.3.2. RMSE of the de noising filter for various channel lengths

We compute the RMSE for a SNR=10dB for different channel lengths. Since the filter is optimized for a channel length of 128, the RMSE is higher than the SNR for the channel length from 0 to 128. If the channel length is higher than 128, the useful signal is cut, resulting in a performance loss. Figure 4.3.2 highlights the gain offered by the de-noising filter. If we have a look at the RMSE for the case of channel duration equal to 56 (see Figure 4.3.3 and Figure 4.3.4), the performance on both borders of the spectrum is poor compared to the performance at the center of spectrum; little or no filter gain may be achieved at the edge of the spectrum.

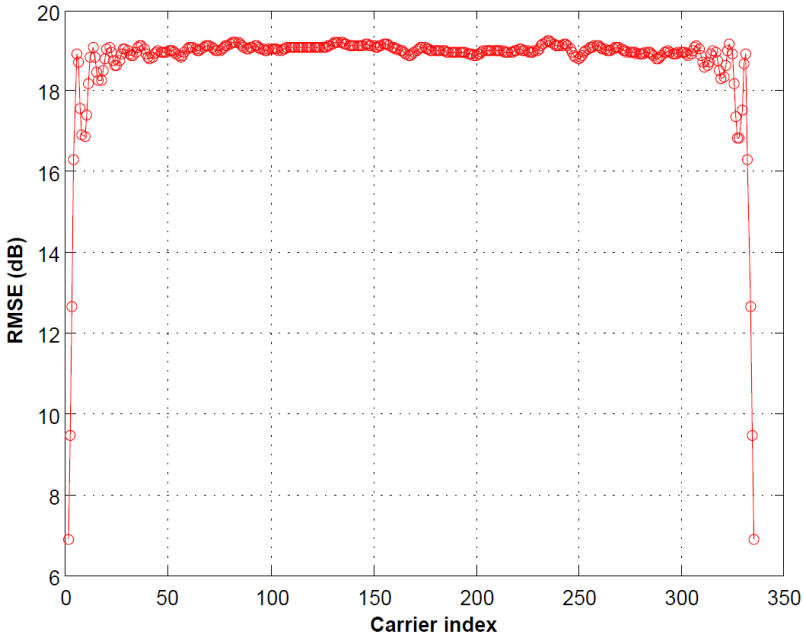

Figure 4.3.2. RMSE of the de-noising filter versus carrier indexes for a channel length of 56.

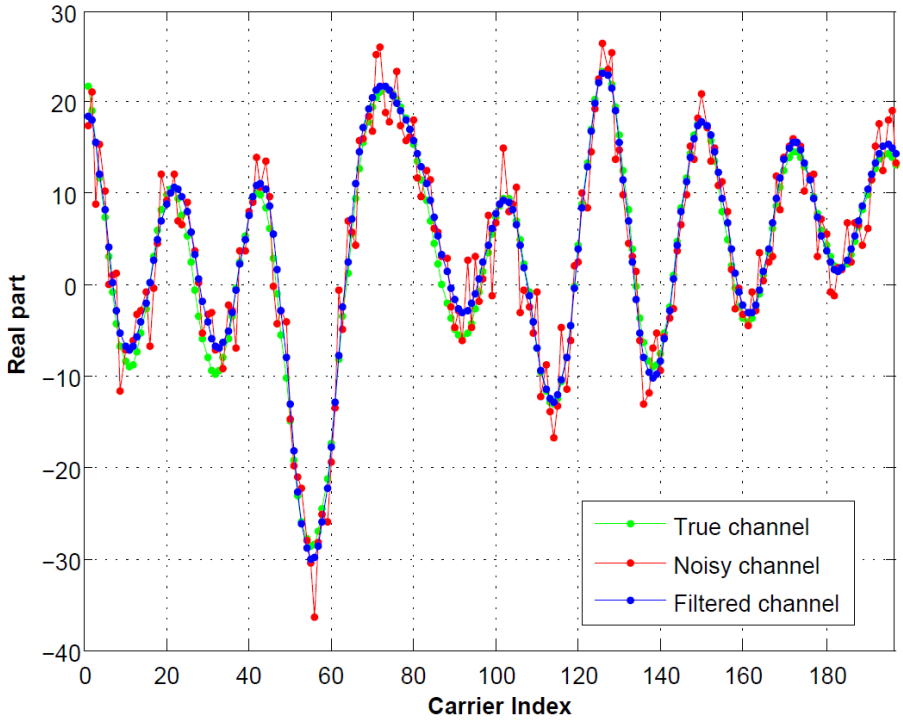

Figure 4.3.4. Illustration of the estimation mismatch at the border of the spectrum.

There is a strong probability that highly fragmented transmission may lead to significant performance degradation in comparison to non-fragmented transmission for the same amount of spectrum usage. In the future of the project we propose to optimize interpolation filters with a particular attention to border effects to improve performance at the edge of the used spectrum and estimate the performance on fragmented channel.